Feasibility study of additive manufacturing techniques applicable to resistojet propulsion systems

Master thesis report
Faculty of Aerospace Engineering
Department of Space Engineering

Justin Bourgois

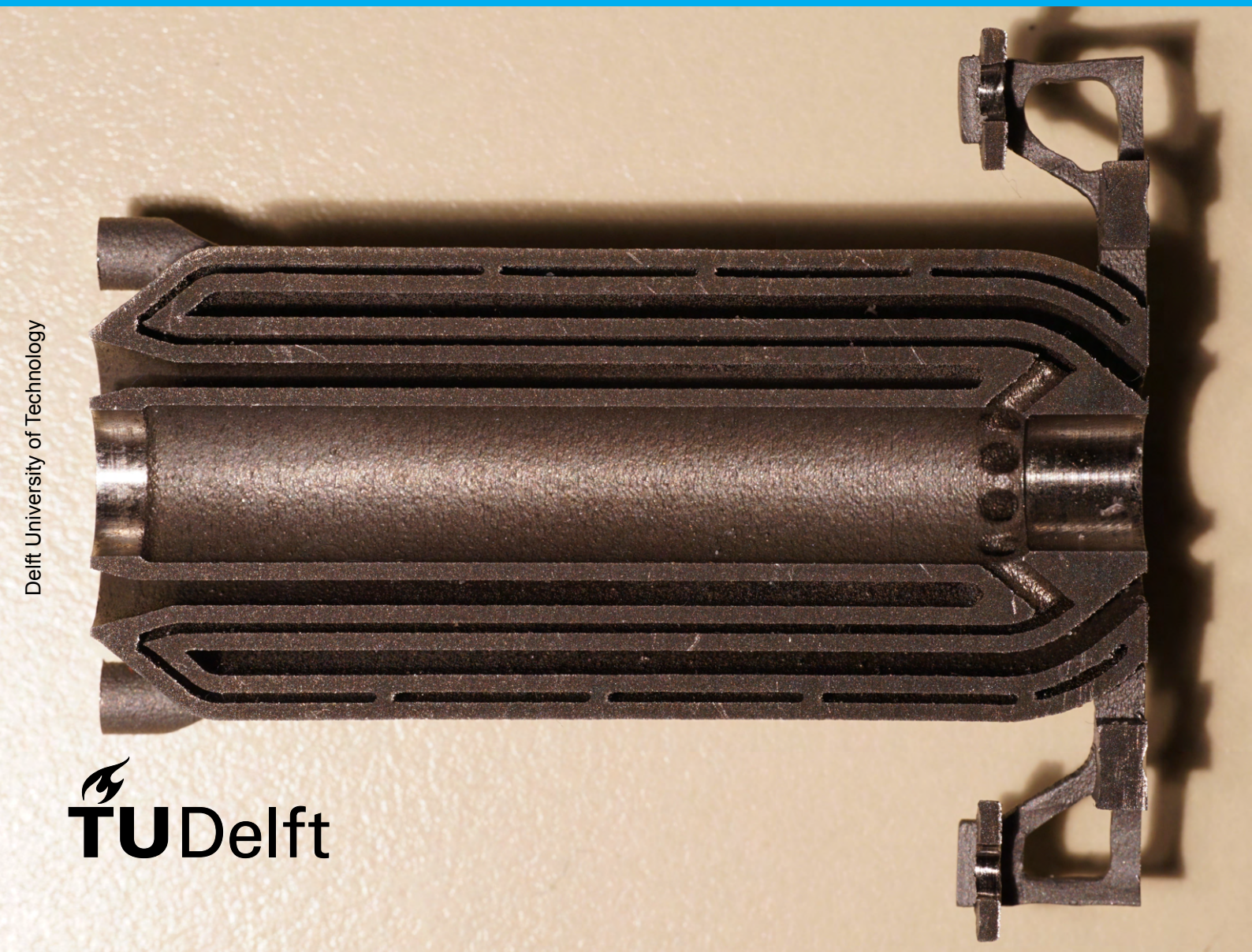

Delft University of Technology

TU Delft

Feasibility study of additive manufacturing techniques applicable to resistojet propulsion systems

by

Justin Bourgois

In partial fulfilment of the requirements for the degree of
Master of Science in Aerospace Engineering
at the Delft University of Technology

Student number:	4667565		
Supervisor:	Dr. B.V.S.Jyoti		
Thesis Committee:	Dr. A. Cervone	TU Delft	Chairperson
	ir. R. Noomen	TU Delft	Examiner
	Dr. B.V.S Jyoti	TU Delft	University supervisor
	Dr. E.R. Santana	Bradford Space	Company supervisor

TU Delft

Preface

This thesis constitutes my graduation assignment for the Space Flight Master's degree at Delft University of Technology. It is the conclusion of five and a half years of studies at the aerospace faculty and marks the end of my studies. I would thus like to thank all of the people who have supported me throughout my studies and this research project.

For this last assignment, I was looking for a topic related to propulsion. I have to thank Dr. Edder Santana from Bradford Space for suggesting the topic of additively manufactured resistojets. Not only was this a propulsion subject, but it also covered one of my other areas of interest, 3D printing. I also have to thank him as well as Dr. Botchu Jyoti for their supervision throughout this project and providing me with valuable feedback.

Many thanks also go to everyone at Bradford Space for welcoming me into their team and being not only great colleagues but also good friends. Special thanks go to the Comet team with which I was working. Thanks to Chris Barta for making sure the 3D printed parts were there on time for testing and to Quentin Mannes for helping with getting the test setup configured and working. I also need to thank Clément Profit and David Mainwaring for their support, expertise, and dedication to ensuring that I could complete my thesis with results that I can be pleased with. Without their help and the late hours they spent with me during the test campaign, this research project would not have been possible.

Finally, I would also like to thank my family for their continued support during my studies and this thesis project.

Justin Bourgois
Delft, January 2023

Summary

Resistojets are one of the simplest types of space micro-propulsion systems. Typically they are found on SmallSats and CubeSats. With the number of missions using these types of satellites going up and becoming ever more complex, the demand for more performant resistojets is also increasing. Resistojets use an electric heater to increase the energy of the propellant before expanding it through a nozzle. Therefore, their performance is dictated by the power that is available to the heater and the temperature it can achieve with this power. Thus making the heating chamber a particularly crucial aspect of their design.

Additive Manufacturing (AM), also known as 3D printing, is a type of manufacturing technology that has gained a lot of interest in recent years in the aerospace domain. In AM, parts are produced straight from CAD (Computer Aided Design) files by progressively depositing material until the part is completed. This type of manufacturing makes very complex geometries possible with next to no additional manufacturing complexity. Furthermore, it also allows for fast design iterations.

Two research projects are already investigating the use of AM for the production of high performance resistojet heating chambers. These projects have shown that it is possible to 3D print heating chambers for resistojets working with gaseous propellant and using the chamber directly as a resistive heater. However, due to the limited amount of research available on the topic of AM resistojets, it was decided that a feasibility study on the use of AM for the heating chamber of a water resistojet with a dedicated heater would be beneficial. Furthermore, this study should also investigate the potential for thermal efficiency improvements that the geometrical design freedom of AM would offer. Bradford Space having already developed a water resistojet were interested in this study and would thus provide the necessary test equipment.

The approach to determine the feasibility of an AM resistojet heating chamber was to design, manufacture and test a prototype chamber. To investigate the potential for efficiency improvements, it was decided that a numerical model capable of predicting the performance of concentric tubular heating chambers should be developed. Following validation with test results, this model could then be used to determine the performance improvements that could be expected from designs optimized to the capabilities of 3D printing.

This model was developed around the assumptions of pseudo-1D inviscid flow and takes into account the basic heat transfer mechanisms to simulate the heat flow from the chamber to the propellant and surrounding environment. It is capable of predicting the fluid temperature at the outlet of the chamber as well as the temperature distribution throughout the chamber for operation at thermal steady state. The goal of the heating chamber prototype was to both demonstrate the feasibility of using AM and to serve as a tool to produce validation data for the numerical model. A 3-layer tubular concentric inconel chamber adapted to AM was thus designed and manufactured.

Testing of the prototype demonstrated that the AM chamber was functional, as throughout six successful tests, the thruster with the AM chamber was able to generate up to 17.3 mN of thrust at a specific impulse of over 140 s. However, the tests were unsuccessful in providing usable validation data at steady state due to deficiencies in the test setup. The numerical model could thus not be validated and used for the investigation of efficiency improvements.

The conclusion of this study is therefore, that it is possible to manufacture a functional water resistojet heating chamber via AM. To determine if this can be beneficial and help with improving the efficiency of resistojets, more work is however needed and new tests with an improved setup need to be carried out to validate the numerical model.

Contents

Nomenclature

Abbreviations

Abbreviation	Definition
3D	Three dimensional
AM	Additive Manufacturing
AQUARIUS	AQUA ResIstojet propUlsion System
BJ	Binder Jetting
CAD	Computer Aided Design
CNC	Computer Numerical Control
DED	Directed Energy Deposition
DfAM	Design for Additive Manufacturing
EBW	Electron Beam Welding
EQUULEUS	EQUilibriUm Lunar-Earth point 6U Spacecraft
FEA	Finite Element Analysis
GSE	Ground Service Equipment
HIP	Hot Isostatic Pressing
ISP	Specific Impulse
PBF	Powder Bed Fusion
SLM	Selective Laser Melting
SSTL	Surrey Satellite Technology Ltd.
STAR	Super-high Temperature Additive-manufactured Resistojet

Symbols

Symbol	Definition	Unit
A	surface area	$[m^2]$
C_p	coefficient of specific heat at constant pressure	$[m/s]$
D	diameter	$[m]$
F	thrust	$[N]$
g	gravitational acceleration	$[m/s^2]$
h	convection coefficient	$[W/(m^2 \cdot K)]$
H	enthalpy	$[J/kg]$
I_{sp}	specific impulse	$[s]$
k	thermal conductivity	$[W/(m \cdot K)]$
L	length	$[m]$
L_h	latent heat of vaporization	$[J/kg]$
M	mass	$[kg]$
M_w	molecular mass	$[kg/mol]$
$\dot{m}$	mass flow rate	$[kg/s]$
Nu	Nusselt number	$[-]$
P	power	$[W]$
p	pressure	$[Pa]$
Pr	Prandtl number	$[-]$
q	heat flux	$[W/m^2]$
r	radius	$[m]$

Symbol	Definition	Unit
R_A	universal gas constant	$[J/(kg \cdot mol)]$
Re	Reynolds number	$[-]$
T	temperature	$[K]$ or $[^\circ C]$
t	thickness	$[m]$
u	flow velocity	$[m/s]$
V_e	exhaust velocity	$[m/s]$
V_{eq}	equivalent exhaust velocity	$[m/s]$
γ	specific heat ratio	$[-]$
ϵ	emissivity	$[-]$
η	efficiency	$[-]$
μ	dynamic viscosity	$[kg/(m \cdot s)]$
ρ	density	$[kg/m^3]$
σ	Stefan-Boltzmann constant	$[W/(m^2 \cdot K^4)]$
σ_{yield}	yield strength	$[Pa]$

List of Figures

List of Tables

1

Introduction

Resistojets offer a simple and affordable propulsion system option for SmallSat and CubeSat missions. With the increasing popularity of these types of satellites, the complexity and duration of missions they get used for also increase. This means that the propulsion system requirements become more and more demanding and that resistojets have to evolve to remain competitive. Meanwhile, additive manufacturing (AM) is starting to be applied more widely in the aerospace domain. While it was initially mostly used for rapid prototyping, AM is now also being used for many flight components. This increased use of AM can be explained by the potential benefits that these technologies offer. Indeed, the geometrical design freedom that AM offers allows for complex and highly optimized shapes to be obtained with little to no increase in manufacturing complexity. Furthermore, the lack of need for part specific tooling makes rapid design iterations possible. Recently a few projects have started looking into the use of AM for resistojet thrusters. Their findings seem promising, as high performance, optimized resistojet prototypes have been shown to work. However, the research in this domain is still limited to only a handful of projects.

The aim of this project is thus to contribute to this research by performing a feasibility study on the use of AM for a water resistojet propulsion system. The components for which AM is applicable need to be identified and the feasibility of using AM for said components needs to be verified by demonstrating the functionality of prototypes of these components adapted to AM. Furthermore, the potential for benefits that AM components offer over conventional ones needs to be investigated to determine if it is not only feasible but also desirable to use AM for resistojet parts. Bradford Space being interested in finding answers to these questions have offered to support this research project by providing the test equipment for the experimental part of this project.

This report starts out with an introduction into the theoretical background and a literature review of the topic in chapter 2. The information presented in the literature review is then used to define the research objective and questions. This is followed, in chapter 3, by the identification of the components for which AM can be used and which should be further analysed as part of this project. Chapter 4 presents the design of an AM heating chamber prototype, from the requirements to the finished part. In chapter 5, the development of a numerical model is presented. The goal of this model is to serve as a design tool for future prototypes and help understand the performance improvements that could be obtained from AM heating chambers. Finally, in chapter 6 the prototype heating chamber is tested, followed by the conclusions and recommendations in chapter 7.

2

Theoretical background and literature review

The purpose of this chapter is to inform the reader about the background, theory and state of the art of the main aspects that will be dealt with during the upcoming chapters. It thus starts off with an introduction on resistojet thrusters, followed by the main equations used to predict and determine their performance and an overview of the three heat transfer mechanisms and their general equations. Then, the concept of additive manufacturing (AM) is introduced along with the main metal AM technologies. Finally, a summary of a previously conducted literature study is presented to provide the reader with an overview of the latest developments in the domain of AM resistojet propulsion systems. This literature study is also used to define the research objective of this study.

2.1. Resistojets

In this section, the concept and working principle of resistojets is introduced. This is followed by the presentation of equations used to predict the performance of resistojets from ideal rocket theory and a brief summary of the main heat transfer equations and how they can be made applicable to a resistojet heater.

2.1.1. Introduction to resistojets

Within space propulsion, resistojets are part of the electro-thermal category. This category itself can be considered as an intermediate between electrical and chemical/thermal propulsion [6]. Resistojets can use propellant initially stored under solid, liquid or gaseous form. In case it is not stored under gaseous form, the propellant is first converted to gas through a combination of expansion and heating. Then, to produce thrust this pressurized, gaseous propellant is subjected to further electrical heating before thermodynamically accelerating it through a convergent divergent nozzle [6]. This basic operating principle also makes resistojets a very simple form of propulsion, only outmatched in simplicity by cold gas thrusters. Indeed, resistojets using gaseous propellant can be considered as enhanced cold gas thrusters or warm gas thrusters [28]. The main components of a resistojet propulsion system are schematically represented in fig. 2.1. They include a tank, a heater or heating chamber, a nozzle and fluidics, i.e. valves, pressure regulators, etc. In some cases, when the propellant is stored under solid or liquid form separate chambers are used to gasify the propellant before heating it further to its final temperature.

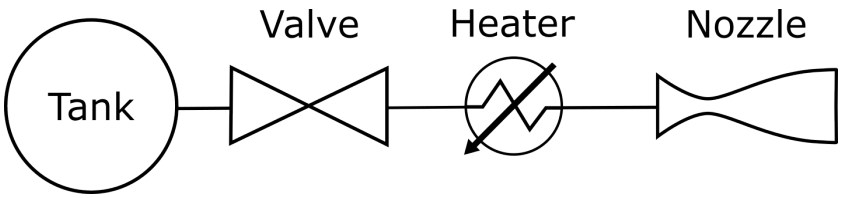

Figure 2.1: Schematic representation of a resistojet propulsion system

Resistojets are mostly used on SmallSats and CubeSats as the main propulsion system or sometimes also as attitude control thrusters on slightly larger satellites [28]. Their main advantage is that they are almost as simple as cold gas thrusters, while offering superior performance. This makes them ideal for smaller missions with more limited resources. However, current designs are still significantly inferior to most forms of electric or chemical propulsion in either specific impulse (I_{sp}) or achievable thrust [10]. As will be highlighted in the following section, these two parameters are limited by the maximum temperature at which the thruster can operate and by the power that is available [28].

2.1.2. Governing equations

Since resistojets use a converging diverging nozzle to accelerate the flow of heated propellant, one can approximate their performance with the classic ideal rocket theory equations as given by Zandbergen [31]. Thrust is given by eq. (2.1), where $\dot{m}$ is the mass flow rate and v_{eq} the equivalent exhaust velocity. v_e is the real exhaust velocity, A_e the outlet area and p_e and p_a are the outlet and ambient pressures respectively. In the case of ideal expansion, these two pressures are equal and $v_{eq} = v_e$. The equivalent exhaust velocity is also used in eq. (2.2) along with the gravitational acceleration at the surface of the Earth g_0 to obtain the specific impulse.

$$F = \dot{m} \cdot v_{eq} = \dot{m} \cdot v_e + (p_e - p_a) \cdot A_e \tag{2.1}$$

$$I_{sp} = \frac{v_{eq}}{g_0} \tag{2.2}$$

Using ideal rocket theory, the exhaust velocity can be obtained from eq. (2.3), where γ is the specific heat ratio, R_A the universal gas constant, M_W the molecular mass of the propellant, T_c the chamber temperature, p_c and p_e the chamber and exhaust pressures. The mass flow rate can be determined with eq. (2.4). In this equation A^* is the throat area of the nozzle. Finally, the relationship between the exhaust to throat area ratio and exhaust to chamber pressure ratio is given by eq. (2.5).

$$v_e = \sqrt{\frac{2\gamma}{\gamma - 1} \cdot \frac{R_A}{M_W} \cdot T_C \cdot \left[1 - \left(\frac{p_e}{p_C}\right)^{\frac{\gamma-1}{\gamma}}\right]} \tag{2.3}$$

$$\dot{m} = \frac{p_C \cdot A^*}{\sqrt{\frac{R_A}{M_W} \cdot T_C}} \cdot \sqrt{\gamma \cdot \left(\frac{1+\gamma}{2}\right)^{\frac{1+\gamma}{1-\gamma}}} \tag{2.4}$$

$$\frac{A_e}{A^*} = \frac{\sqrt{\gamma \cdot \left(\frac{1+\gamma}{2}\right)^{\frac{1+\gamma}{1-\gamma}}}}{\sqrt{\frac{2\gamma}{\gamma-1} \cdot \left(\frac{p_e}{p_C}\right)^{\frac{2}{\gamma}} \cdot \left[1 - \left(\frac{p_e}{p_C}\right)^{\frac{\gamma-1}{\gamma}}\right]}} \tag{2.5}$$

While these general equations are already useful by themselves, they can be made more relevant to resistojets by making a few assumptions. Resistojets are designed to be used as in orbit maneuvering thrusters, thus it is reasonable to assume that they will be operated in vacuum conditions. Furthermore, due to their small size they typically have very small throat diameters (< 1 mm). This means that high expansion ratios can easily be achieved while keeping the outlet diameter reasonably small, hence why one can make the assumption that the exhaust gases are expanded to vacuum conditions. Setting $v_{eq} = v_e$ and $p_e = 0$ one can simplify and combine eq. (2.2) and eq. (2.3) to obtain eq. (2.6), where C_p is the specific heat coefficient at constant pressure of the propellant. This equation is very useful, as it

clearly shows that the I_{sp} that can be achieved is dependent on the propellant choice and its specific heat, C_p, and on the heater design, as it dictates the temperature that the propellant reaches. Applying the same simplifications to the thrust equation, one can obtain eq. (2.7). This equation shows that the thrust is only dependent on the nozzle design (A^*), the operating conditions (p_c) and the choice of propellant (γ).

$$I_{\mathsf{sp}} = \frac{1}{g_0}\sqrt{\left(\frac{2\gamma}{\gamma-1}\right)\frac{R_A T_c}{M_{\mathsf{w}}}} = \frac{\sqrt{2C_p T_c}}{g_0} \tag{2.6}$$

$$F = p_C \cdot A^* \cdot \sqrt{\frac{2\gamma^2}{\gamma-1}\cdot\left(\frac{1+\gamma}{2}\right)^{\frac{1+\gamma}{1-\gamma}}} \tag{2.7}$$

Another equation that is relevant for resistojet thrusters and can easily be derived is the power consumption equation, eq. (2.8) [5]. In this equation, C_{pL} and C_{pG} are the constant pressure heat coefficients of the liquid and gaseous propellant respectively, L_h is the latent heat of vaporization and T_0 and T_{boil} are the initial and boiling temperatures of the propellant. Combining this equation with eq. (2.4) one can obtain eq. (2.9).

$$P_{ideal} = \dot{m} \cdot [C_{pL} \cdot (T_{boil} - T_0) + L_h + C_{pG} \cdot (T_C - T_{boil})] \tag{2.8}$$

$$P_{ideal} = \frac{p_C \cdot A^*}{\sqrt{\frac{R_A}{M_W} \cdot T_C}} \cdot \sqrt{\gamma \cdot \left(\frac{1+\gamma}{2}\right)^{\frac{1+\gamma}{1-\gamma}}} \cdot [C_{pL} \cdot (T_{\mathsf{boil}} - T_0) + L_h + C_{pG} \cdot (T_C - T_{\mathsf{boil}})] \tag{2.9}$$

From these equations, one can clearly understand the disadvantages of resistojets already mentioned in section 2.1.1. Indeed, for a given propellant, a temperature increase is required to improve the I_{sp}, thus also increasing the power consumption and requiring a higher operating temperature for the heater. Higher thrust meanwhile can only be achieved by means of a higher operating pressure or larger throat area, leading once again to an increase in power consumption.

While eq. (2.8) gives the power requirement for a resistojet, this is only the power that gets transferred to the propellant and not the power consumption of the heater. This power consumption is given by eq. (2.10), where the efficiency of the heater is also accounted for. Given the dependence of a resistojet on electrical power to achieve good performance, it is important to maximise the efficiency of the heater.

$$P_{heater} = \eta_{heater} P_{ideal} \tag{2.10}$$

2.1.3. Heat transfer

As it has just been established that the efficiency of the heater and thus also its design is crucial to achieving good performance with a resistojet thruster, one might already deduce that this will be an important aspect of this thesis project. Indeed, chapter 4 will cover the design and optimisation of an AM heating chamber. Thus, it is useful to already introduce the relevant concepts and mechanisms of heat transfer in this theoretical background chapter. Heat can be transferred by conduction, radiation or convection. The equation describing conduction is eq. (2.11)[15], where q_x is the heat flux along the x direction, k is the thermal conductivity, A is the the cross-sectional area of the material conducting heat perpendicular to the path of conduction, ΔT the temperature difference and Δx the distance between the points between which conduction occurs.

$$q_x = kA\frac{\Delta T}{\Delta x} \tag{2.11}$$

For radiation heat transfer, during this project the assumption was made that any radiating bodies behave like grey bodies. This means that for radiation from a body to the environment the emitted flux (q") can be expressed as shown in eq. (2.12) [15]. In this equation ϵ is the emissivity of the body, σ the Boltzmann constant and T the temperature of the body.

$$q" = \epsilon \sigma T^4 \tag{2.12}$$

For surface to surface radiation, the general equation is eq. (2.13) [15], where q_{12} is the rate of radiation transfer from surface 1 to surface 2, T_1 and T_2 are the temperatures of the respective surfaces, A_1 and A_2 their surface areas and ϵ_1 and ϵ_2 their emissivities. Finally F_{12} is the view factor of surface 1 to surface 2. So since during this project the radiation between concentric cylinders will be analysed, one can already simplify eq. (2.13) for this specific case. For long/infinite concentric cylinders one has: $\frac{A_1}{A_2} = \frac{r_1}{r_2}$ and $F_{12} = 1$, thus the surface to surface radiation equation can be rewritten as shown in eq. (2.14) [15].

$$q_{12} = q_1 = -q_2 = \frac{\sigma \left(T_1^4 - T_2^4\right)}{\frac{1-\varepsilon_1}{\varepsilon_1 A_1} + \frac{1}{A_1 F_{12}} + \frac{1-\varepsilon_2}{\varepsilon_2 A_2}} \tag{2.13}$$

$$q_{12} = \frac{\sigma A_1 \left(T_1^4 - T_2^4\right)}{\frac{1}{\varepsilon_1} + \frac{1-\varepsilon_2}{\varepsilon_2}\left(\frac{r_1}{r_2}\right)} \tag{2.14}$$

The general equation for convected heat flux, eq. (2.15) [15] is quite simple and only contains the difference between the wall temperature, T_{wall}, and the mean fluid temperature $T_{fluid,mean}$, as well as the convection coefficient h. The Nusselt number Nu is typically used as shown in eq. (2.16) [27] to describe the relationship between the convective heat transfer and conductive heat transfer in a flow. In this equation, k_{fluid} is the conductivity of the fluid and D_h the hydraulic diameter of the pipe in which the flow and heat transfer occur. The hydraulic diameter is defined as shown in eq. (2.17), where A is the cross-sectional area of the pipe and P its perimeter. Ideally, the Nusselt number should be determined empirically to ensure convection is correctly accounted for. However, in the case of laminar flow, according to R. Shankar Subramian [27], the Nusselt number for pipe flow with a uniform heat flux can be taken as 4.36, while for a uniform wall temperature a value of 3.66 or the use of eq. (2.18) is advised. For more precise results, one can also use eq. (2.18) [27]. In this equation Re is the Reynolds number of the flow, see eq. (2.19), Pr the Prandtl , see eq. (2.20), and L the length of the pipe.

$$q" = h(T_{wall} - T_{fluid,mean}) \tag{2.15}$$

$$h = \frac{k_{fluid}}{\mathsf{Nu} \cdot D_h} \tag{2.16}$$

$$D_h = \frac{4A}{P} \tag{2.17}$$

$$\mathsf{Nu} = 3.66 + \frac{0.065\,\mathsf{Re}\,\mathsf{Pr}\,\frac{D_h}{L}}{1 + 0.04\left(\mathsf{Re}\,\mathsf{Pr}\,\frac{D_h}{L}\right)^{2/3}} \tag{2.18}$$

$$Re = \frac{\rho u L}{\mu} \tag{2.19}$$

$$Pr = \frac{C_p \mu}{k} \tag{2.20}$$

Having given the general heat transfer equations and the main ways in which they can be adapted to resistojet heater applications, this concludes this section on the theoretical background of heat transfer.

2.2. Additive manufacturing

In this section the concept of additive manufacturing is introduced. First the working principle is described, followed by a brief discussion on the major advantages and disadvantages of this type of technology. The most common metal additive manufacturing technologies are then presented along with their suitability for producing resistojet components.

2.2.1. Introduction to additive manufacturing

Additive manufacturing (AM) also referred to as 3D printing or solid freeform fabrication is a type of manufacturing process that is being used for more and more applications in the aerospace industry in recent years. AM is a Computer Numerical Controlled (CNC) manufacturing process in which finished or close to finished parts get produced straight from a Computer Aided Design (CAD) file, without requiring part specific tooling. However, contrary to most other CNC machining processes, 3D printing is an additive, rather than subtractive, process. Indeed, the printing process starts out with an empty build surface or volume on which material is added until the complete part is built up. This is typically accomplished in a layer-by-layer process where material is being deposited over the cross-section of the part being built and fused to the previous layer. These stacked and fused cross-sections of material make up the completed part. The range of materials that can be manufactured via various AM processes is quite wide and includes polymers, ceramics and metals. In the context of resistojets, high operating temperatures and good mechanical properties are needed. Hence only AM metals will be discussed throughout this project. [2, 4]

3D printing covers a range of promising technologies that potentially offer many advantages over more conventional manufacturing methods. These advantages include a reduction in the generated waste, no need for part specific tooling and increased geometrical design freedom. The latter of these advantages in particular is one of the key factors for the increased interest in AM, since it allows for better optimization of part designs without increasing the complexity of the manufacturing process. In fact, manufacturing and assembly can even be simplified by solidifying multiple parts and reducing the part count. Furthermore, designs including intricate internal geometries that could previously not be made are now possible through AM. [2, 4]

The lack of need for part specific tooling, like for most other CNC processes, means that design changes can quickly be implemented. This makes AM ideal for rapid prototyping and design iterations, which allows designers to explore different solutions while keeping development time and cost low. Demonstrating that it is possible to 3D print resistojet components could thus prove useful by allowing engineers to more rapidly optimise these components, allowing them to achieve higher performance. [2, 4, 3]

There are however also still challenges to overcome and potential disadvantages to 3D printing. The main challenge is that AM is still quite a new manufacturing process which means that best practices, testing and certification procedures are not well established yet. This means that defects such as voids, inclusions or cracks can be more frequent than for parts manufactured from one piece of bulk material. Another disadvantage is that with the current technologies the surface roughness of printed parts is significantly higher than typical machined parts. Finally, while AM allows for very complex geometries, manufacturing still has to be taken into account during the design process and limitations such as overhang angles, bridging and closed voids have to be taken into account. [2, 4, 9, 7, 8]

2.2.2. Common metal additive manufacturing technologies

In metal additive manufacturing one can distinguish between three common AM technologies, Directed Energy Deposition (DED), Powder Bed Fusion (PBF) and Binder Jetting (BJ), all with their own benefits and drawbacks.

DED is a process in which the printing head deposits the feedstock metal on the build plate / previous layer, while simultaneously melting it. The feedstock is either under powder or wire form and the heat source can be a laser, electron beam or plasma arc. DED could be compared to Metal Inert Gas (MIG) welding, a process in which the welding filler material is extruded through the welding torch. The produced parts can be used as printed or further processed to relieve internal stresses and reduce surface roughness. The main advantages of this technology are that it can achieve high feed rates and is not confined to an enclosed environment. Indeed, the printing head can in theory be mounted to any kind of robotic arm or gantry, since the inert gas used to prevent oxidation can be directly supplied from the printing head. On the flipside, this process can however not resolve very fine details and achieve high accuracy. This makes DED ideal for printing larger parts that do not have small features requiring tight tolerances. [11, 4]

PBF differs from DED by the fact that instead of material being deposited and fused only where needed, the whole build surface is covered in feedstock, under the form of a very fine powder. The printer then selectively melts and fuses the powder along the cross-section of the part, before the next layer of powder is deposited and the process repeated. The energy source used to fuse the powder

can either be an electron beam or a laser, in which case the process is sometimes also called Selective Laser Melting (SLM). Once the printing process is completed, the fused part needs to be separated from the printing surface and the unfused powder can be removed. Parts are usable as printed, but can benefit from post processing to relieve thermal stresses or improve material properties. PBF can achieve finer details than DED, but part size is limited by the dimensions of the printing enclosure. This makes it more suitable for smaller, more detailed parts. [11, 16, 4]

The binder jetting process is similar to PBF. Powder is deposited over the entire printing surface and gets fused where necessary. The main difference is that instead of using an energy source to melt the metal powder, a binding agent is projected onto the powder to join the particles. This means that the printing process can be performed at low temperature and does not require an inert atmosphere. Once the part has been fully printed, the loose powder should be removed. The difference between BJ and the two other technologies is that the parts have poor mechanical properties when they come out of the printer, since it is just metal powder held together by a binding agent. The parts are thus usually not used as printed, but instead the binding agent is first burned out and the part heat treated to sinter the metal particles together. The resulting parts can have similar structural properties as the ones produced via the other processes, but the heat treatment process causes severe amounts of shrinkage, leading to poor dimensional accuracy if this is not correctly accounted for. [11, 17]

From the three technologies that have just been presented, DED is the least suitable one for resistojet components due to its inability to resolve fine details. Between PBF and BJ, PBF is the technology that has seen more research and is therefore better understood. Since the limited understanding of the 3D printing technologies is one of their major drawbacks, one can minimize the disadvantage of using AM by using the more well researched AM technology. Hence why PBF fusion is currently the more suitable type of 3D printing technology for resistojet components.

2.3. State of the art in 3D printing of resistojet components

In preparation to this thesis project a literature study was carried out. This section contains a summarized version of the findings from this study. First two research projects on the use of AM for resistojet heaters and nozzles are presented. This is followed by the presentation of the only known AM resistojet to have flown on a mission. Lastly, the findings of a few studies on 3D printed tanks are summarized.

2.3.1. STAR thruster

One of the first projects to look into the use of AM for resistojet thrusters is the Super-high Temperature Additive-manufactured Resistojet (STAR) project by a team from the University of Southampton and Surrey Satellite Technology Ltd. (SSTL). The initial goal of the project was to design a resistojet that would be an attractive option as an attitude control thruster for geosynchronous satellites and as an orbit keeping thruster for SmallSats [23]. To avoid the need for a second type of propellant onboard geosynchronous satellites that already have an electric main propulsion system, it was decided that the new resistojet should operate on Xenon [23]. To make it competitive with other types of propulsion systems typically used in these applications, the STAR thruster should achieve a specific impulse in the 80 s range, requiring an operating temperature of 2400 K.

High performance resistojets operating at these kinds of temperature had already been developed prior to the STAR project. One of these is the 3 kW Concentric Tubular Resistojet developed by the Marquardt Corporation in the 1960s [13]. This resistojet featured a heat exchanger with concentric tubular channels, allowing the propellant (hydrogen in this case) to flow from the outer channels to the inner channels before being expelled through the nozzle. The heat exchanger structure was made by chemical vapor deposition out of tungsten and acted not only as a heat exchanger, but also as a resistive heat source, when electricity was allowed to flow through it. Thanks to its geometry and the resulting recirculating flow path, the outer channels could be kept at a relatively low temperature, while the necessary high temperatures were reached in the inner channels. The complexity of the manufacturing and assembly process, as well as the challenges of long term storage of hydrogen however meant that this promising design never saw any use in space missions [10].

Having identified the potential of these 1960s designs, the STAR project team realised that the manufacturing challenges of such designs could largely be circumvented by the use of AM. Indeed, thanks to the geometrical freedom of AM, tubular concentric structures and internal channels are relatively easy to achieve and recent developments in 3D printing even make it possible to print refractory

metals, such as tungsten or tantalum. The STAR project thus focused on developing an AM tubular concentric resistojet heater exchanger, also using the structure as a heating element. [23]

First prototypes were designed and manufactured in stainless steel 316L to investigate the feasibility of 3D printing the desired geometries. Despite a Design for Additive Manufacturing (DfAM) approach, some printing defects still lead to the first prototype being unusable, as partially fused powder left between the layers would have obstructed the propellant flow path and shorted the resistance. Despite also suffering from small defects, a second prototype with a slightly altered geometry was deemed satisfactory. One of the design elements of the STAR thruster, made possible by AM, was the nozzle integrated into the heat exchanger design. To investigate this particular aspect of the design, nozzles with four different divergence angles ranging from $10°$ to $30°$ were printed. The goal was to determine if larger divergence angles, i.e. larger overhang angles, could be detrimental to the quality of the nozzle throat and diverging section surface finish. The conclusion was however, that the nozzle throat was undersized and too irregular to be used as printed for any of the overhang angles. Thus post-machining was deemed necessary for the nozzle. [23]

During a first series of tests, the concept of an additively manufactured concentric tubular heat exchanger with integrated nozzles was demonstrated to be viable. Even though a non 3D printed ceramic insulator suffered from a crack, which lead to leakage, the thruster was able to produce thrust and heat the argon propellant (to be replaced by Xenon in later stages) up to 400 °C [24]. Later tests with an unbroken insulator, still using a stainless steel exchanger, showed that the thruster was able to achieve a specific impulse of up to 75 s [25]. After experiencing some failures in first endurance tests, the design was adjusted and new heat exchangers made out of Inconel 625 and tantalum were used for further endurance testing. The STAR project team was able to demonstrate reliable operation of these heating chambers for over 6000 cycles at 30 W (corresponding to an I_{sp} of 60 s and a thrust of 70 mN) for Inconel chambers and for over 10000 cycles at 60 W (corresponding to an I_{sp} of 80 s and a thrust of 70 mN) for tantalum chambers [21, 22].

With this the STAR project has thus shown that it is possible to produce and operate a high performance additively manufactured resistojet heating chamber.

2.3.2. High-efficiency hydrogen resistojet

Over the last couple of years a team of researchers from Japan also started to investigate the use of AM for a resistojet thruster. The goal of their project is to develop a high performance hydrogen resistojet that can be used on all-electric spacecrafts as an orbit raising thruster. By reaching high temperatures in excess of 2000 K, a hydrogen resistojet can achieve a specific impulse of 700 s to 800 s. Additionally, such thrusters inherently can achieve better specific power and higher thrust than comparable electric propulsion systems. This would make a high temperature hydrogen resistojet competitive with plasma and hall-effect thruster. [10]

The team working on this project also drew inspiration from the early high temperature resistojets of the 1960s. However, unlike the STAR project, their adaptation of those designs to AM retains hydrogen as the propellant. A first prototype has been designed and tested as part of a proof of concept study. This design is manufactured via SLM (selective laser melting), a type of PBF, out of Inconel 718, features 12 concentric layers, an integrated nozzle and also uses the heat exchanger body as the heating resistor. [10]

The Inconel prototype has been tested and shown to work with Nitrogen. With this propellant, it was able to reach a temperature of 747 K when operating at 75 W with a mass flow rate of 0.2 g/s, giving it an I_{sp} of 108 s and a heater thermal efficiency of 72 %. The success of these tests opens the door for future tests with the intended propellant, hydrogen, and for new prototypes made out of tungsten. Based on the performance of the first prototype, these changes should allow the thruster to achieve the desired temperature of over 2000 K and an I_{sp} in excess of 700 s. [10, 20, 19]

2.3.3. AQUARIUS propulsion system

While the two previously mentioned project are very promising, they are still at the experimental level and need some further maturing before they can be integrated into a spacecraft. The AQUARIUS (AQUA ResIstojet propUlsion System) water resistojet, developed by the university of Tokyo, however is at a more advanced development stage. This propulsion system comprises one main vaporization chamber, linked to six thrust heads with integrated pre-heaters. Two of those heads can be used for delta-V manoeuvres, while the remaining four serve as reaction control thrusters. The vaporization

chamber is fabricated via AM out of aluminium, as are the pre-heaters of the thrust heads. This allows the pre-heaters to have helical flow paths, designed to minimize heat losses. While the main mission the AQUARIUS system has been designed for, EQUULEUS (EQUilibriUm Lunar-Earth point 6U Spacecraft), is yet to take place, this propulsion system has already been flight-tested during the AQT-D (AQua Thruster-Demonstrator) mission. During this mission, the propulsion system, integrated into a 3U cubesat was deployed from the ISS (International Space Station), in November 2019 and has re-entered the atmosphere in April 2022. This makes it the only known AM resistojet propulsion system to have flown on a mission. Unfortunately, there is little information published about the design process of its 3D printed components and no information on its flight performance could be found. [30, 1]

2.3.4. Non-resistojet related projects

Studies on the use of AM for resistojet components are not very numerous. However, the heat exchanger and nozzle are both covered by some of those studies. The tank meanwhile is not considered in any of the studies related to resistojets and AM. Tanks only being a simple pressure vessel, the type of propulsion system they are part of is only of limited relevance. Thus, AM tanks for chemical and cold gas thrusters were also considered during the literature review. In a study by Easley et al. [12], the possibility of combining elements of the satellite structure with the tank was explored. This was done through CAD design, which involved topological optimization and finite element analyses (FEA). The report concluded that while the design was acceptable and met the performance criteria, further optimization to improve the structural performance and better application of design for AM guidelines should be performed before manufacturing and testing a first prototype. Solorzano [26] also investigated the use of AM for a propellant tank. His research involved designing and manufacturing two prototypes. The manufacturing process did not include any post processing heat treatments such as HIP (Hot Isostatic Pressing) to reduce porosity and improve mechanical properties. One of the prototypes was pressure tested up to failure. The test results generally seemed to agree with the FEA analysis and the tank was able to exceed the structural requirements. It was however judged that here as well, the design could benefit from further optimization. A study by Nahmany et al. [18] evaluated the performance of a pressure vessel manufactured out of AlSi10Mg via SLM and joined by electron beam welding (EBW). With a leak rate of less than 1×10^{-8} scc/s, the vessel was deemed to be gas-tight. Furthermore, its structural performance can also be regarded as acceptable with a residual deformation of up to 2.3 % for a pressure of 30 MPa. These are only a few examples of studies related to tanks of micro propulsion systems and AM. If one widened the scope and looked for 3D printed pressure vessels of a similar scale, more studies could be found. However, the three studies presented here are sufficient to show that a resistojet propulsion system could potentially make use of a 3D printed tank.

2.4. Conclusions and definition of research objective

Based on the literature currently available on the 3D printing of resistojets, one can conclude that the feasibility of using AM components in this type of propulsion system has already been partially studied and confirmed. It has been shown that it is possible to 3D print functional heating chambers prototypes that combine the roles of heat exchangers and resistive heaters. Resistojet nozzles can also be printed, but can only be used as printed if they are above a certain size, otherwise they require an additional machining step. While tanks have not been 3D printed for resistojets specifically, studies have shown that this is already possible for other types of micro-propulsion and there is no reason to believe that this would be any different for resistojets.

The Comet-1000 thruster, on which this study is referred, differs from the AM resistojets already covered by other studies. The two main differences are that it uses a propellant stored under liquid form, water, and that it uses a dedicated heating element as its heat source, rather than using the whole heating chamber as a resistor. Given these differences, it was deemed that it would still be valuable to investigate the use of AM on the these components.

Furthermore, the Comet system being an existing, fully functional and flight proven propulsion system, allows for an easy comparison between this baseline design and the proposed design, incorporating AM components. This is ideal to evaluate if the use of AM components can be beneficial to resistojets and their performance, an aspect that has not been well covered by previous studies. Indeed these studies claim that there are significant benefits to using AM, but without a direct comparison,

this question cannot be categorically answered.

For these reasons it was decided to define the following, twofold research objective:

”To demonstrate the feasibility of using additively manufactured components as part of a resistojet propulsion system and demonstrate the resulting advantages, by designing, manufacturing and testing additively manufactured components for a resistojet propulsion system.”

The research objective is complemented by two main research question and their associated sub-questions.

1) Can the key components of a resistojet propulsion system be manufactured with additive manufacturing technologies?

1.1) Can the tank be manufactured with additive manufacturing technologies?
1.2) Can the heating chamber be manufactured with additive manufacturing technologies?
1.3) Can the nozzle be manufactured with additive manufacturing technologies?

2) Can additive manufacturing of the key components of a resistojet propulsion system be beneficial to the system design and performance?

Given the limited time available for this research project, it was deemed that only an in depth investigation of one of the main components would be possible and thus only one of the sub-questions of question #1 could be treated. The next chapter deals with the selection of the component that the project focuses on and provides preliminary answers to the first set of questions. Furthermore, sub-questions relevant to the selected component are formulated for question #2.

3

Identification of components suitable for additive manufacturing

The main components of a resistojet propulsion system are the tank, nozzle and heating chamber. In this chapter an analysis will be conducted for each of these components to determine if they are likely to be manufacturable via AM and whether it makes sense to consider using AM. This will be done both in the general context of resistojets and taking into account the Comet-1000 propulsion system configuration. The goal of this chapter is to identify which component is sufficiently promising to warrant a more detailed analysis. This is necessary, since the time-frame and resources that can be allocated to a thesis project do not allow for an in-depth analysis of all three components.

3.1. Tank

3.1.1. General considerations

As discussed in section 2.3.4, it has already been shown that tanks of micro-propulsion systems and pressure vessels can be 3D printed. Tanks are hollow structures which are typically made either by forming methods, such as deep drawing, or milled/lathed out of one solid piece of material. For forming, a material with good plastic properties is needed. This limits the available options in terms of tank materials and thus a compromise has to be made between good forming properties and good properties of the finished tank. In the case of subtractive machining, one of the major drawbacks is the generation of significant amounts of waste material in the form of chips. Furthermore, certain materials are subject to work hardening or have other attributes that make them challenging to machine. By directly depositing the material in its final shape, AM circumvents these issues, potentially making it a competitive manufacturing method for tanks.

The key benefit of 3D printed tanks is however the possibility of integrating additional features directly into the tank design. As demonstrated by Easley et al. [12] and Solorzano [26], pipe fittings, mounting brackets and structural elements can be incorporated into the part that forms the tank. The solidification of these components can significantly reduce the part count, making the assembly simpler and reducing the risk of failures at mounting interfaces. At the same time, topological optimisation can also be implemented to reduce the mass of the tank and the additional features integrated into it without compromising their performance or significantly complicating the manufacturing process.

So, from a general point of view, it would indeed be interesting and relevant to perform a more detailed analysis on the feasibility and benefits of 3D printed resistojet tanks. This is especially true since no examples of AM resistojet tanks could be found in literature.

3.1.2. Specific considerations

Since the feasibility study is performed by using Bradford Space's Comet-1000 thruster and adapting selected components to AM, it is important to also consider if it makes sense to use 3D printing for the tank of this specific propulsion system. To benefit from the geometrical freedom of moving to AM, part solidifaction could be applied, meaning that the mounting brackets, shown in fig. 3.1 could be

integrated into the tank design. However, these brackets are meant to be adapted to customer needs and many different variants exist. While it can make topological optimisation somewhat harder, this should in principle not be a problem, since the bracket part of the AM tank design could still be adapted to customer needs. However, as it is a pressure vessel, the tank design needs to be tested and certified to get flight rated. Modifying an aspect of the design, such as the brackets, would require a new testing and certification process for each redesign. Thus each time a customer needs a new type of bracket, certifying a new tank design would increase the costs and lead times. For this reason, in the context of the Comet 1000 thruster, integrating structural elements is not desirable. An AM version of the current design would mostly be a one to one copy of this design with only the necessary changes to make it 3D printable and adapted to different material properties.

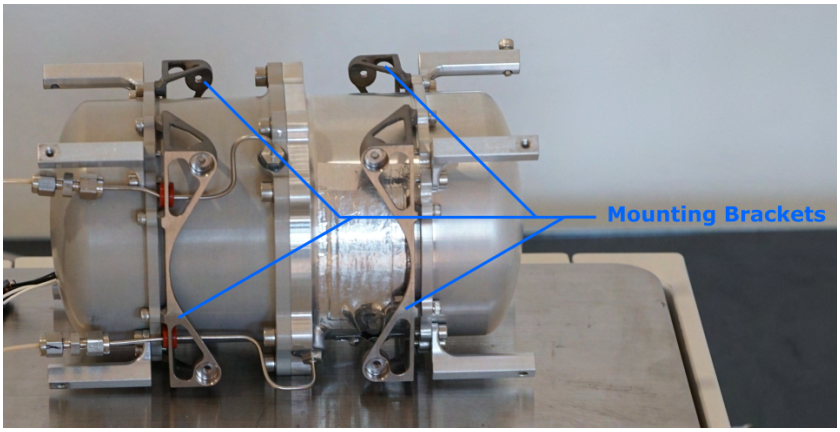

Figure 3.1: Comet-1000 tank with mounting brackets

In this case only a change in material could justify moving to AM. The current version of the thruster uses an aluminium tank, which, given the water content of the tank, poses material compatibility challenges with other components, like the stainless steel pipe fittings. This combination of materials can give rise to galvanic corrosion in the presence of water, if not properly controlled, which could compromise the structural integrity of components or lead to the formation of oxide deposits that can clog piping, valves or even the thruster nozzle. Switching from aluminium to titanium would alleviate this challenge while also being beneficial in terms of mass, since titanium has better structural properties than aluminium. While this change in material could be done without altering the type of manufacturing process, given the price of titanium stock, its poor machinability and the relative ease with which it can be 3D printed, a switch to AM would make sense.

In the standard configuration, to regulate the pressure of the propellant inside of the tank, a phase change material along with heaters placed on the outside of the tank are used. This means that the heat from these heaters needs to be transferred by the tank to its content. Given the much lower thermal conductivity of titanium compared to aluminium, concerns were raised on the impact that switching to titanium would have on the ability to regulate the tank pressure. It was thus decided to perform a brief analysis of the implications of adapting the tank design to titanium, as presented in section 3.1.3.

3.1.3. Analysis on the use of titanium for the tank

The first step in determining what impact a move from aluminium to titanium would have for the tank is to determine how the wall thickness would have to be changed to still achieve the same structural properties. Since the tank is a pressure vessel, the required wall thickness can be determined with the radial and axial hoop stress formulae for a cylinder and for a sphere, eq. (3.2), eq. (3.2) and eq. (3.3), where σ is the tensile stress inside of the wall, r the radius of the vessel, P the pressure difference between the inside and outside of the vessel and t_{wall} the wall thickness. From these equations one can see that for a given pressure and radius, the wall thickness required to not exceed the failure stress of the tank material is inversely proportional to that stress. For example, for an aluminium tank configuration with a wall thickness between 1.2 and 2.0 mm. Aluminium has a yield strength of 180 MPa, meaning that an equivalent titanium tank with a yield strength of 190 MPa would have a wall thickness between 0.237 and 0.395 mm. Since typical metal 3D printers can only achieve wall thicknesses of

0.5 mm or larger, the thickness of a titanium tank would not be limited by structural concerns but by manufacturing limits.

$$\sigma_{cylinder,radial} = \frac{Pr}{t_{wall}} \tag{3.1}$$

$$\sigma_{cylinder,axial} = \frac{Pr}{2t_{wall}} \tag{3.2}$$

$$\sigma_{sphere} = \frac{Pr}{2t_{wall}} \tag{3.3}$$

For tanks with otherwise equal proportions and properties, one can show that the mass is proportional to the wall thickness multiplied by the density of the tank material and the heat capacity is proportional to the mass times the specific heat coefficient of the material. Using the properties shown in table 3.1, one can thus determine that a titanium tank would only have 69.0 to 41.4 % of the mass of an aluminium tank and 42.5 to 25.5 % of the heat capacity. These are two desirable consequences of using titanium over aluminium, since lighter components are always favorable for spacecrafts and a lower heat capacity would make the temperature control and thus pressure control of the tank faster and more accurate.

Table 3.1: AlSi10Mg and Ti6Al4V material properties[1]

Material	AlSi10Mg	Ti6Al4V
$\sigma_{yield}\ [MPa]$	190	900
$\rho\ [kg/m^3]$	2650	4390
$k\ [W/(m \cdot K)]$	130	6.8
$C_P\ [J/(kg \cdot K)]$	910	560

The main problem with a titanium tank is thus its low conductivity. This could create an excessive temperature difference between the inside and outside of the tank, leading to losses through radiation. To determine if this can indeed be a problem, it was decided to perform a simplified 2D analysis. In 2D, the cross-section of the tank, its content and the external heaters can be represented as shown in fig. 3.2. To heat a phase change fluid, the heat has to travel from the heated surface through the tank wall, towards the inside. When further simplifying the problem by ignoring the curvature (thin wall assumption) and only considering the radial heat transfer, one can obtain the 1D case as shown in fig. 3.3. Based on this case, using the thermal conduction eq. (2.11), rewritten for this specific case as shown in eq. (3.4), one can determine that when the heaters generate a heat flux of 800 W/m^2, the temperature difference between the inside and outside of the tank wall is between 0.0074 and 0.0123 °C for an aluminium tank and 0.59 °C for the titanium equivalent. While in relative terms, the temperature difference is significantly larger for the titanium tank than for the aluminium one, in absolute terms it is still sufficiently small to not be concerning.

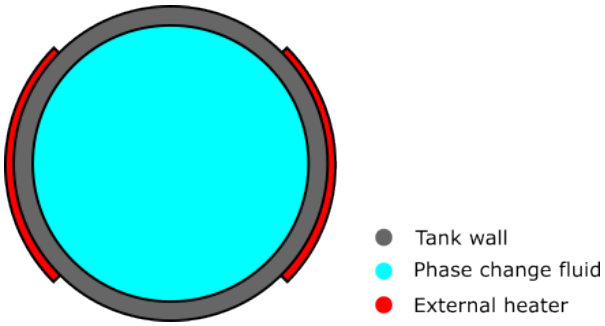

Figure 3.2: Schematic cross-section view of the propellant tank and its external heaters

[1] `https://www.materialise.com/en/industrial/3d-printing-materials` accessed: 10.2022; `https://www.makeitfrom.com/` accessed: 10.2022

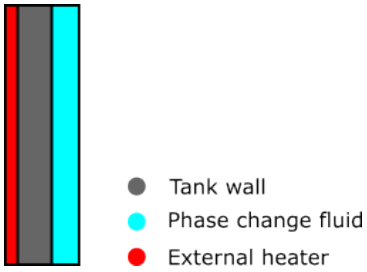

Figure 3.3: Schematic representation of the simplified 1D thermal conduction analysis of the propellant tank

$$q" = -k\frac{\Delta T}{t_{wall}} \Rightarrow \Delta T = \frac{q"t_{wall}}{k} \tag{3.4}$$

3.1.4. Conclusion

To conclude this discussion on AM resistojet tanks, one can say that based on literature it seems highly likely that it is feasible to manufacture such a tank. This thus indicates that one could answer research question #1.1 positively. An AM tank also brings a number of benefits and it would thus be valuable to investigate this further. In the context of the present study however, the potential benefits are far more limited since part solidifaction is not an option. Only the transition from milled aluminium to 3D printed titanium could bring appreciable benefits. In the case of the baseline tank, the tank is thus not the ideal component to demonstrate the potential for benefits that comes from using AM.

3.2. Nozzle

3.2.1. General considerations

For the nozzle the same general advantages apply as for most other components when considering 3D printing. The geometrical freedom makes more complex shapes possible, meaning that one can easily achieve optimized nozzle designs with little added manufacturing complexity compared to conical nozzles. Furthermore, additional features, such as cooling channels can also be integrated into the nozzle design or the nozzle can itself be integrated into other components like the heating chamber. Finally, it can once again be easier to use certain materials in combination with AM rather than with conventional machining processes.

Resistojets being mostly used for micro-propulsion are typically quite small. Given the current resolution limits of AM, their scale limits the possibilities to integrate small features such as cooling channels into the nozzle. Furthermore, the surface roughness that is characteristic of AM parts can also become problematic at those scales. Thus, whether it is desirable or even possible to 3D print a resistojet nozzle depends on the scale of the specific system considered.

3.2.2. Specific considerations

With a rated thrust of 17 mN and an operating power between 25 and 55 W, the Comet thruster is clearly not a large resistojet propulsion systems. The studied design is based on a convergent divergent nozzle with a throat diameter of smaller than 0.4 mm. Some marginal benefits could probably be obtained by optimizing the nozzle shape, however, the surface roughness would likely negate those benefits. Furthermore, depending on the process, machine and supplier that is chosen for printed parts, details smaller than 40 mm cannot be resolved[2]. Indeed, Romei et al. [23] investigated the use of AM for resistojet nozzles with a throat nozzle of 0.42 mm and found that already at this scale, 3D printing was not able to produce satisfactory results. The nozzle throats were consistently undersized and not circular.

To obtain an AM nozzle with a smooth surface finish and sufficiently precise throat, one would have to machine the throat and outlet section after the printing process. This would again make it difficult to obtain anything other than a conical nozzle at this scale and thus negate most of the advantages of AM. The only benefit that one could still exploit would be the integration of the nozzle into the heating chamber, if that part is also 3D printed.

[2] `https://www.materialise.com/en/industrial/3d-printing-materials/inconel-718` accessed: 11.2022

3.2.3. Conclusion

The analysis on whether the nozzle could potentially be 3D printed and if this would be beneficial can be concluded by saying that for small thrusters, like the one being studied, no significant benefits should be expected. So, the answer to research question #1.3 depends on the scale of the propulsion system in question. For this project, the nozzle should only be printed if the heating chamber is also printed and it is judged to be useful to solidify both of these components into a single part.

3.3. Heat exchanger

3.3.1. General considerations

The literature study presented in section 2.3 has shown that it is already possible to 3D print resistojet heating chambers. Furthermore, while the possibility to use high temperature rated materials, such as tungsten [19], is an advantage over conventional machining methods, it is once again the geometrical freedom that seems to be the main driver for using AM. Mounting brackets can be integrated in the chamber design and parts can be solidified to reduce the part count. More importantly, significant performance improvements can be achieved at little to no additional manufacturing complexity, by optimizing the flow geometry to reduce heat losses.

3.3.2. Specific considerations

For this study, some considerations have to be made if one is to design an AM heating chamber with a geometry tailored for a reduction in heat losses. While the two projects that have previously explored the possibilities of AM tubular concentric heating chambers were using the chamber itself as the resistor and heating element, a dedicated heating element will be used for the purposes of this study. Indeed, a redesign to AM should be based around the types of heating elements that allow for the integration of the proposed chamber into the test equipment based on the Comet design. While this should not hinder the change in manufacturing process or negate the expected benefits, it will provide slightly different challenges and necessitate a different design approach.

As a further consequence of using test equipment intended for the Comet thruster, it was decided that it would be preferable to aim for operation at a constant temperature of no more than 750 °C. This limitation means that investigating the use of AM refractory metals is not possible. The study should thus focus more on the benefits that AM can have in terms of geometry rather than material selection. As such, the capability of AM heating chambers to operate at the same temperature, but with higher efficiency than conventional designs without added manufacturing complexity should be demonstrated.

The two previous projects on AM resistojets both used propellant in the gaseous phase at the chamber inlet. The Comet thruster, meanwhile is designed to operate with water and thus also the AM design developed for this study. This is something that needs to be taken into account when designing an AM heating chamber, as corrosion becomes a much more prevalent concern and the phase transition can also influence the geometrical design of the chamber.

3.3.3. Conclusion

The conclusion of the analysis on the heating chamber as a potential candidate for investigating the use of AM can be summarized as follows. In general 3D printed heating chambers seem feasible and no aspect resulting from the use of the Comet thruster as a base design should be an obstacle to using AM for the chamber. Clear benefits can be expected from an AM chamber and the demonstration of potential for efficiency improvements should be the main focus of the second research question. Furthermore, the particularities of Comet and associated test equipment, i.e. the use of a dedicated heating element and water as the propellant, mean that research on the use of AM for its heating chamber would not just be a repetition of previously performed studies, but introduce new aspects and challenges, increasing the scientific value of the project.

3.4. Conclusion

From considering the three main components of a resistojet propulsion system it can be concluded that for this study, 3D printing the heating chamber has the highest chances of success and of being beneficial. The tank should also be printable and can bring some advantages, but since the possibilities are far more limited this should not be the main focus of this project. It could however still be the subject

of later studies. Finally, the only advantage that could be obtained from printing the nozzle would be the possibility to integrate it into the heating chamber. To simplify comparisons between a new AM design and the reference design of the chamber it is however better to use the same nozzle. Thus, to allow this study to be completed within the time-frame allocated to the thesis it was decided to focus the research on only demonstrating the feasibility of using an AM heating chamber and investigating the potential for efficiency improvements that this allows.

Thus from this point onward the goal of this research should be to answer the following research questions:

1) Can the key components of a resistojet propulsion system be manufactured with additive manufacturing technologies?

1.2) Can the heating chamber be manufactured with additive manufacturing technologies?
  1.2.1) Can the 3D printed heating chamber be integrated into a complete propulsion system?
  1.2.2) Can the 3D printed heating chamber be used as part of a propulsion system to produce thrust?

2) Can additive manufacturing of the key components of a resistojet propulsion system be beneficial to the system design and performance?

2.1) Can 3D printing of the heating chamber lead to a thermal efficiency increase?

4

Heating chamber prototype design

To investigate the feasibility of using an AM heating chamber as part of a resistojet propulsion system, it was decided to design, manufacture and test a prototype chamber. This chamber should also be designed in such a way that it can be used to explore the potential for benefits that the use of AM offers in this context. In this chapter the design process of this prototype is presented. First, the design and manufacturing constraints and requirements will be established in section 4.1. This is followed by the presentation of the design process itself in section 4.2.

4.1. Design and manufacturing constraints

In this section, the design and manufacturing constraints are discussed. Where necessary a justification is given for these constraints before they are turned into requirements. First, the manufacturing limitations are presented, followed by the design and integration requirements. Finally, the functional and performance requirements are also discussed.

4.1.1. Manufacturing requirements

Even though AM offers much more design freedom than many other manufacturing methods, there are still a number of constraints that should be taken into account when designing AM components. Additionally to the general DfAM rules, one also needs to consider the capabilities and limitations of the specific machine that will be used. It is therefore important to already know which supplier and what machine will be used. Two AM parts suppliers were contacted early on in the project: Materialise[1] and Velo3D[2]. Materialise is a european consolidated 3D printing company, offering PBF printing services for a wide range of applications. Velo3D meanwhile were contacted because they offer high quality prints in high temperature rated alloys, such as Hastelloy and Scalmalloy and claim that their machines allow for more geometrical complexity than typical metal 3D printers. Furthermore, they are already well established in the space industry. In the end, it was decided to work with Materialise, despite the slightly more limited capabilities of their printers. The reason for this is that they could guarantee shorter lead times for printing the parts.

For PBF AM, the main design constraints are overhang angles, unsupported surfaces, enclosed volumes, minimum wall thickness and minimum feature size. Typically the maximum overhang angle (angle of an overhanging wall from the horizontal) should not be below $45°$. However, following discussions with Materialise it was decided that the limit should be set to $50°$ to guarantee a better surface finish. While unsupported surfaces can be printed with the help of sacrificial support structures that are removed after the printing process, this is only an option for features that are accessible. Thus internal surfaces cannot have any unsupported surfaces. Enclosed volumes are problematic because they do not allow for the removal of loose, unfused powder after printing. In fact internal volumes should ideally have two openings with a clear flow path linking them together to allow for pressurized gas to be used to blow the loose powder out of the part. The minimum wall thickness is a property of the printer and

[1] `https://www.materialise.com/en` accessed: 11.2022

[2] `https://velo3d.com/` accessed: 11.2022

a consequence of how well tuned it is. On their website[3], Materialise indicate that the minimum wall thickness for all of their metals is 0.5 mm except for inconel where it is 1.0 mm. During discussions with them it was however made clear that for vertical walls the thickness could also be reduced to 0.5 mm for inconel. Finally, the minimum feature size that Materialise can guarantee for any of their materials is 0.4 mm. All of these manufacturing constraints are reflected in the following requirements:

REQ-PR-M: Manufacturing requirements

REQ-PR-M-1 The prototype shall have a minimum wall thickness of 0.5 mm.

REQ-PR-M-2 The prototype shall have a minimum feature size of 0.4 mm.

REQ-PR-M-3 The prototype shall have no features with an overhang angle of less than 50° (from horizontal).

REQ-PR-M-4 The prototype shall have no internal features requiring support material.

REQ-PR-M-5 The prototype shall allow for the removal of the unfused powder.

REQ-PR-M-6 The prototype shall be made out of a 3D printable material.

4.1.2. Design and integration requirements

As already mentioned in chapter 3, the AM heating chamber will use an internal heater and a separate nozzle to be compatible with the test setup. This is reflected by the first two design requirements, REQ-PR-D-1 and REQ-PR-D-2. Furthermore, to allow for testing, the chamber needs to be integrated into the aforementioned test setup. The integration requirements defining some of the main dimensions and highlighting the fact that some areas need to remain accessible for welding are there to ensure a smooth integration process.

Additionally there are two more design requirements, REQ-PR-D-3 and REQ-PR-D-4 dictating the general geometry of the heating chamber. These are not necessary for the feasibility demonstration, but for the investigation of potential benefits. Given that previous studies claim that AM tubular concentric heating chambers can contribute to improving the performance and efficiency of resistojets, this type of chambers should be the type investigated as part of this study.

REQ-PR-D: Design requirements

REQ-PR-D-1 The prototype shall use a central heating element compatible with the test equipment.

REQ-PR-D-2 The prototype shall use a nozzle similar to the one used on the Comet propulsion system.

REQ-PR-D-3 The prototype shall feature concentric tubular channels.

REQ-PR-D-4 The prototype shall feature a flow path going from the outer to the inner channels.

REQ-PR-I: Integration requirements

REQ-PR-I-1 The prototype shall allow for welding of a central heating element.

REQ-PR-I-2 The prototype shall have a mounting interface compatible with the test setup.

REQ-PR-I-3 The prototype shall have an inlet designed for a feedline compatible with the test setup.

REQ-PR-I-4 The prototype shall allow the welding of the feedline.

REQ-PR-I-5 The prototype shall allow the welding of the nozzle.

REQ-PR-I-6 The prototype shall have a maximum diameter of 40 mm.

REQ-PR-I-7 The prototype shall have a maximum length of 75 mm.

[3] `https://www.materialise.com/en/industrial/3d-printing-materials` accessed: 11.2022

4.1.3. Functional and performance requirements

Only the need to be able to place thermocouples in relevant locations is reflected by the functional requirements. This is needed to ensure that data can be gathered that can be used to validate the temperature distribution predicted by the numerical model developed in chapter 5.

The performance requirements meanwhile are applicable to both feasibility and performance testing. Indeed, the heating chamber needs to be able to fully vaporize the water it is supplied, otherwise it would compromise the tests and could potentially damage test equipment. During the tests the heater will be operated at a temperature of up to 750 °C. Since the chamber and heater are in close proximity, the chamber also needs to withstand this temperature. Finally, the propellant tank and supply system is set to withstand a pressure of up to 1.0 MPa. Multiplying this by a safety factor of 1.5 means that the chamber must be able to withstand an internal pressure of up to 1.5 MPa to prevent a failure.

REQ-PR-F: Functional requirements

REQ-PR-F-1 The prototype shall allow for the placement of thermocouples along the outer wall during operation.

REQ-PR-F-2 The prototype shall allow for the placement of thermocouples along the walls of the inner channels during operation.

REQ-PR-P: Performance requirements

REQ-PR-P-1 The prototype shall vaporize the propellant supplied at an initial temperature of 20 °C under nominal operating conditions.

REQ-PR-P-2 The prototype shall have a maximum operating temperature of no less than 750 °C.

REQ-PR-P-3 The prototype shall withstand an internal pressure of 1.5 MPa.

4.2. Prototype design

In this section, the prototype design process is presented. First, the material selection is explained. This is then followed by the presentation of the design of the main chamber features as well as some of the minor additional features.

4.2.1. Material selection

For the material selection, the range of materials that can be considered is limited by the choice of manufacturer. Materialise can print five different metal alloys: Aluminum (AlSi10Mg), Titanium (Ti6Al4V), Stainless Steel (SS316L), Inconel (IN718) and Stainless Steel (C465). To select the most appropriate metal for the heating chamber it was decided to perform a simple trade-off. The criteria shall be given a weight of 1, 2 or 3 and the alloys can score a value from 1 to 5, representing unacceptable, poor, marginal, good and excellent performance.

The first and most important criterion is the maximum operating temperature of the material. As highlighted by requirement REQ-PR-P-2, the chamber needs to be able to operate at the same temperature as the heating element. So, the selected material should not be severely weakened by the high temperature and should ideally also not suffer from excessive corrosion under these conditions. Given its importance this criterion is given a maximum weight of 3.

The thermal conductivity of the material should also play an important role in the selection of the alloy. Indeed, as will be explained in more detail during the design process, reducing the amount of heat that is being conducted through the chamber to the satellite structure can greatly improve the efficiency of the system. While this can be influenced by geometrical features, having a low material conductivity helps greatly with this. Hence why thermal conductivity has a weight of 2.

As already discussed in section 3.1.3, for tubular pressure vessels the strength-to-density ratio of a material is an important factor, as it is determining for the mass of the vessel. During operation, the heating chamber structurally behaves like a cylindrical pressure vessel. Thus the strength-to-density ratio should also be taken into account in this trade-off. Since the wall thickness is however also likely to be driven by manufacturing limits rather than only by part strength, this criterion only gets a weight of 1.

The surface roughness of the 3D printed parts that can be achieved by the manufacturing company should also be taken into account as a criterion. The reason for this is that the heating chamber will

feature narrow channels. If these channels have a high roughness, this could locally narrow or widen the channels and affect the flow in unpredictable ways. This criterion is however not of high importance as all five materials have roughness values within a narrow range, so this criterion shall have a weight of 1.

The performance of each metal alloy is presented in table 4.1. The values used in this table were taken from Materialise's own website[4] for the surface roughness and strength-to-density ratio, and from the MakeItFrom[5] engineering materials database for the operating temperature and thermal conductivity, except for the thermal conductivity of C465 stainless steel which was found on ACNIS International's website[6]. For Ti6Al4V, SS316L and C465 the properties of the annealed material were used and for IN718 the as-fabricated properties were taken, while for AlSi10Mg only one set of properties is available. The strength used in the strength-to-density ratio is the yield strength. For the maximum operating temperature, the lower of either the mechanical or corrosion maximum temperature was used.

Table 4.1: AM metal properties used in material selection trade-off

Materials	Operating temperature $[°C]$	Thermal conductivity $[W/(m \cdot K)]$	Strength-to-density $[MPa \cdot cm^3/g]$	Surface roughness $[\mu m]$
AlSi10Mg	160	130	71.6	70
Ti6Al4V	330	6.8	205.0	80
SS316L	410	15	42.8	70
IN718	980	11	92.9	60
C465	680	15	191.3	70

To convert these values into unacceptable, poor, marginal, good and excellent performance scores, one needs to define the thresholds for each score. These thresholds are shown in table 4.2. Doing the conversion yields table 4.3. This table also includes the total score for each material, which is obtained by multiplying the score for each parameter with the corresponding weight and adding those values together.

Table 4.2: Material selection trade-off scoring thresholds

Materials	Operating temperature $[°C]$	Thermal conductivity $[W/(m \cdot K)]$	Strength-to-density $[MPa \cdot cm^3/g]$	Surface roughness $[\mu m]$
Excellent	>950	<10	>200	<55
Good	>850	<15	>120	<65
Marginal	>750	<25	>75	<75
Poor	>650	<45	>50	<85
Unacceptable	<650	>45	<50	>85

Table 4.3: Material selection trade-off results

Materials	Operating temperature	Thermal conductivity	Strength-to-density	Surface roughness	Total score
Weight	3	2	1	1	
AlSi10Mg	1	1	2	3	10
Ti6Al4V	1	5	5	2	20
SS316L	1	4	1	3	15
IN718	5	4	3	4	30
C465	2	4	4	3	21

[4] `https://www.materialise.com/en/industrial/3d-printing-materials` accessed: 11.2022
[5] `https://www.makeitfrom.com/` accessed: 11.2022
[6] `https://acnis-titanium.com/wp-content/uploads/2020/06/UK-Custom465_-FT039.pdf` accessed: 11.2022

From table 4.3, one can see that the most suitable metal alloy for the heating chamber is Inconel 718, since it has the highest overall score and is the only option that has a maximum operating temperature in excess of the required 750 °C. In case an alternative option is needed, stainless steel C465 could be used, as it has the second highest score and its maximum operating temperature, while being less than required, is still not unreasonably low.

4.2.2. Chamber geometrical design

The geometrical design of the heating chamber needs to incorporate a number of features to comply with the requirements introduced in section 4.1. The process of implementing these features is schematically summarized in fig. 4.1. The first illustration of this figure shows the simplest possible design for a tubular heating chamber around a central heating element. The channel width has been set to 0.5 mm to comply with REQ-PR-M-2. The wall thickness is set to 0.8 mm for manufacturability purposes. While according to REQ-PR-M-1 a thickness of 0.5 mm would be acceptable, it was decided to add some margin to this dimension to reduce the risks of a failed print. Indeed, due to the time constraint of this project, it was clear that it would not be possible to make design changes and get a second version of the chamber manufactured on time if the first one was deemed unfeasible. Hence why a rather conservative design approach was chosen. The length of the channel from the inlet to the outlet was set to 41.3 mm, to match the dimensions of the heating element and include a 2 mm tall open volume above the heater before the flow reaches the nozzle.

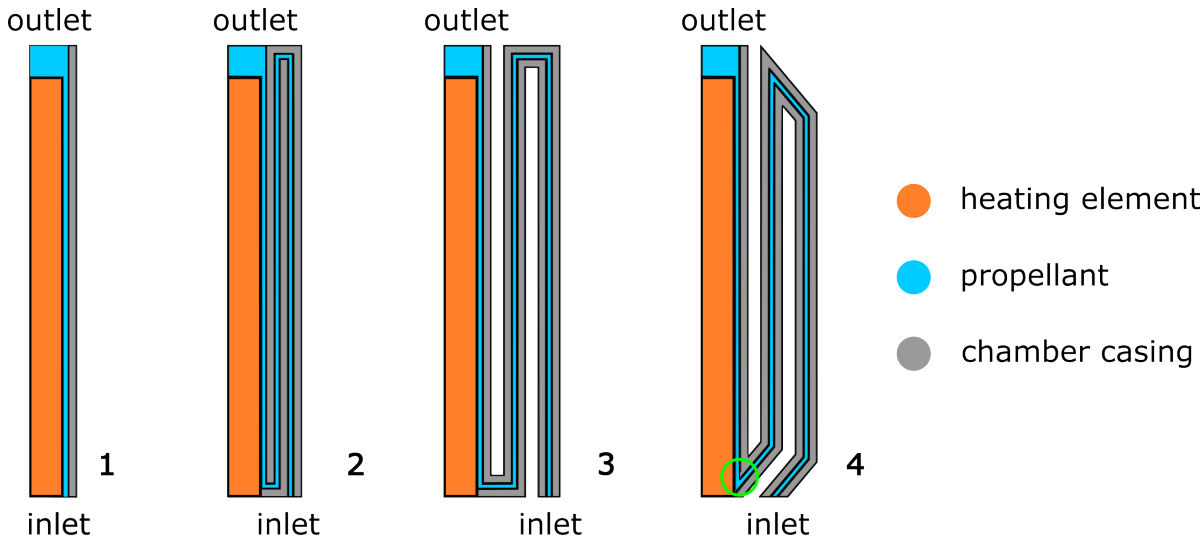

Figure 4.1: Half cross section schematic of AM heating chamber at different stages of the design process

To comply with REQ-PR-D-3 and REQ-PR-D-4, the number of channels was then increased from 1 to 3 as illustrated by the second image of fig. 4.1. The reason for choosing three layers is that this is the minimum number of layers that allows the chamber to feature each type of possible layer: an inner layer with the heater as the channel inner wall; an intermediate layer surrounded by other layers on the inside and outside and an outer layer exposed to the external environment. Having these three types of layers should help with gaining a better understanding of the heat transfer mechanisms during the performance investigation phase of the project.

Next, as a measure to reduce heat losses by conduction from the inner layers to the outer layers, the layers were separated by a gap. This considerably increases the path the heat has to travel to reach the outer layer of the chamber, as the layer walls can only transfer limited amounts of heat directly to each other via radiation. Furthermore, these gaps also allow for the placement of thermocouples along the walls of the inner layers, making the design compatible with REQ-PR-F-2. This design feature is not found in the two other projects using AM for tubular concentric heating chambers. The reason for this is that in those projects, the chamber walls also serve as the heating resistance, while here the heat is generated by a central heater. Not having to take into account the resistivity of the chamber

allows for more design freedom as illustrated by the addition of these inter-layer spacings.

The forth step shown in fig. 4.1 is necessary to make the design compliant with REQ-PR-M-3 and REQ-PR-M-4. This is achieved by inclining the horizontal surfaces found in the third step to an angle of $50°$. This only leaves one problem area, circled in green, where an internal feature is unsupported. A solution to this issue was implemented by extending the problematic wall edge down all the way to the lower wall. To still allow the flow to pass through this now closed passage, holes were distributed circularly in this area to link the two channels back together. This is shown in fig. 4.2, circled in green. Furthermore, instead of having an annular inlet as shown in fig. 4.1, the lower opening of the outer layer channel was closed off and a smaller inlet was added on the side of the chamber. This inlet feeds the fluid tangentially to the circular channel and makes the design compatible with the feedline and compliant with REQ-PR-I-3. The inlet is shown in fig. 4.2, circled in orange.

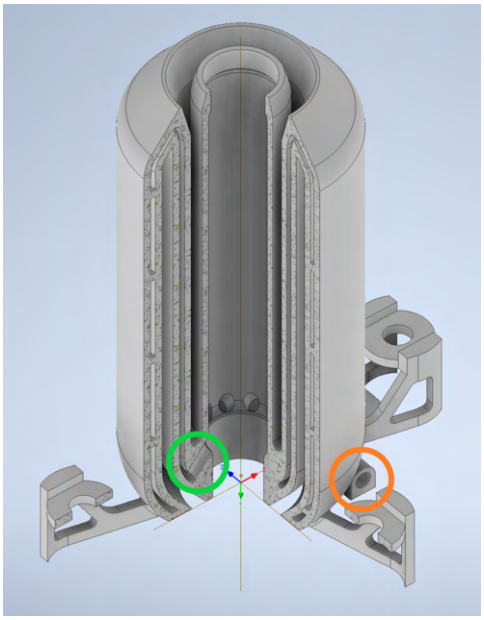

Figure 4.2: Quarter section view of the heating chamber design with passage from intermediate-to-inner layer circled in green and tangential inlet circled in orange

To better contain the heat and improve the performance of the chamber, the outer layer could have been extended to better shield the base of the heater and the nozzle from the environment. However, these areas need to remain accessible to allow for welding of the additional components, as specified by REQ-PR-I-1 and REQ-PR-I-5. Thus, the outer layers were not extended past the base of the heater and the interface with the nozzle.

Now that a first rough design of the heating chamber has been completed, it is important to also check that it is structurally sound and can withstand the internal pressure specified in REQ-PR-P-3. Since the entire inside of the chamber will be at or near the pressure at which the propellant is supplied, it is only necessary to check the outer layer. Accounting for the heater dimensions, wall and channel thicknesses, the outer radius of the chamber is 11.09 mm. Using a rewritten version of eq. (3.1), with the 11.09 mm radius, a wall thickness of 0.8 mm and the yield strength of 3D printed inconel (750 MPa[7]), one obtains a maximum operating pressure of 54 MPa for the chamber, well above the required 1.5 MPa. So, as expected, the chamber is structurally over-designed and the wall thickness is limited by the manufacturing process rather than its strength.

4.2.3. Additional features

Having completed the design of the heating chamber itself, some additional features still needed to be implemented. The mounting brackets shown in fig. 4.3 were designed to allow for the integration of the chamber with the test setup without needing a separate mounting bracket. Additionally to working as mounting brackets, they also increase the length of the heat path from the chamber to the interface.

[7] `https://www.materialise.com/en/industrial/3d-printing-materials/inconel-718` accessed: 11.2022

Another feature that was also added are mounting points for a radiation shield that might be used in future testing.

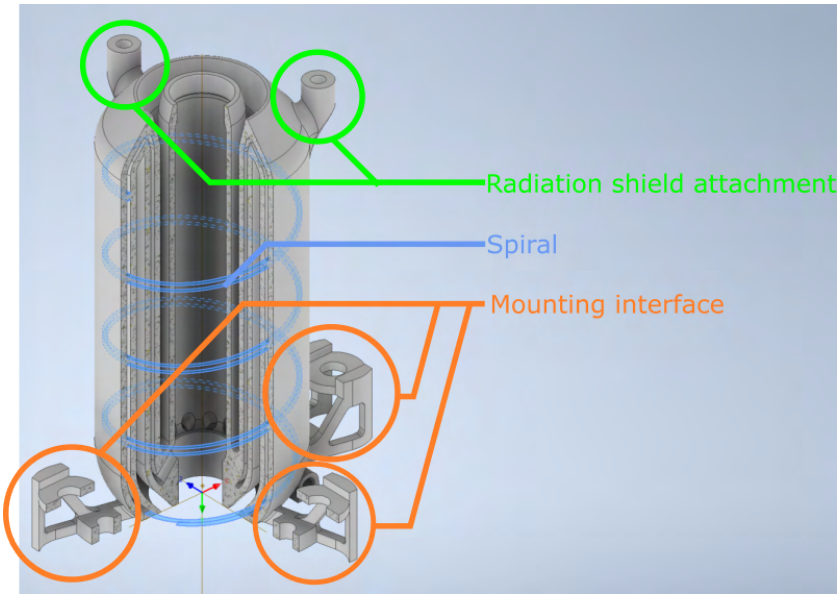

Figure 4.3: Quarter section view of the heating chamber design with radiation shield attachment points, outer layer spiral and mounting interface

Finally, during discussions with the manufacturing company, concerns were raised about the post printing powder removal process. Indeed, the fine and long channels coupled with the small inlet located on only one side of the chamber might allow some loose powder to remain trapped even when compressed air is injected into the chamber. As a possible mitigation, a spiral was added to the channel in the outer layer, see fig. 4.3. This feature should force the compressed air to flow through the entirety of the chamber, carrying any loose powder away with it. At the same time, this feature should also help distribute the water more evenly throughout the chamber during operation, avoiding the formation of hot spots. The technical drawings of the complete heating chamber design are included in appendix A.

5

Numerical model

In this chapter a numerical model developed to simulate the heat transfer within tubular concentric heating chambers and predict their performance is introduced. The goal of this model is to help understand the design parameters that can help improve the performance of AM resistojet heating chambers and serve as a design tool for future chambers. It should also help to demonstrate the potential for improvement that AM offers. These design objectives for the numerical model are discussed in more detail in section 5.1. This is followed by section 5.2 where the main requirements for the numerical model are defined. Section 5.3, itself divided into three subsections, then explains the development process of the model. Finally, in the last section, section 5.4, the verification and validation as well as a brief sensitivity analysis of the simulations are discussed.

5.1. Design objective

In the previous chapter, a prototype heating chamber, adapted to AM, was designed. During this design process, little to no considerations were made to tailor the performance of the prototype. Indeed, its design is mostly based on design limitations dictated by AM and the need to make it compatible with the GSE (Ground Service Equipment) used as part of the test setup.

Ideally, performance requirements should have been defined before the design process. Either thermodynamic theory or numerical simulations or ideally both should then have been used to tailor features and dimensions such as the number of concentric layers, channel widths, wall thicknesses etc. in a way that ensures the requirements are met. Due to lead times of AM part production and post processing, it was judged safer to rapidly generate a first design and send it into production before a full understanding of the thermodynamics of a resistojet heat exchanger had been gained.

While this is acceptable for a first design that only needs to serve as a proof of concept, a good understanding of the heat transfer from the heating chamber to the propellant is still necessary. This knowledge would help to ensure that future AM heat exchangers can be optimized and meet performance requirements and to gain a better understanding of the potential for improvement made possible by the use of AM technologies and the associated geometrical design freedom. For these reasons it was decided that a numerical simulation tool capable of predicting the heat transfer within the heat exchanger would be necessary.

At first, the use commercial simulation softwares such as ANSYS Fluent and Star CCM+ was considered. However, the challenges of simulating two phase flow (water and steam) and the transition from one to the other coupled with the lack of high performance computing equipment lead to the decision to develop a simplified custom numerical model in house, based on the equations shown in section 2.1.3.

The objective of this model is to both serve as a design tool for future AM resistojet heating chambers and help demonstrate the potential of designs made possible by AM. To achieve this objective, the model should be able to predict the performance of a heating chamber based on a range of input parameters without requiring excessive computing power. To ensure that state-of-the-art AM heating chambers can be evaluated, the numerical model should be based around the concept of circular concentric heating chambers. In the next section, the requirements to guarantee that this objective is achieved are detailed.

5.2. Requirements

To fulfill its objective, the numerical model needs to be able to predict the performance of the heating chamber. The main parameter that describes the performance of a resistojet heating chamber is the temperature of the propellant at its outlet. Indeed, as can be seen from the equations introduced in section 2.1.1, for a given operating pressure, throat area and propellant, the mass flow rate and specific impulse are dictated by the chamber outlet temperature. To determine this outlet temperature for a given input power, the model needs to determine the amount of heat that is transferred to the propellant and wasted via conduction or radiation. This gives rise to the first set of functional requirements REQ-NM-F-1 to REQ-NM-F-1.3.

However, to be useful as a tool to help understand the heating process within the chamber, the model should provide more than just the temperature at the outlet. Knowing the temperature along the flow path and the chamber walls would help to understand where boiling occurs and where conduction and radiation losses are the most severe. Hence requirements REQ-NM-F-2 to REQ-NM-F-2.2 are defined.

Since the model should serve as a design tool and not just as an analysis tool for one specific case, it should be able to take a number of parameters as input variables into account. These parameters should allow the user to simulate the heating chamber at different operating conditions. Requirements REQ-NM-F-3 to REQ-NM-F-3.5 should ensure the model can replicate various operating conditions of the heating chamber typical of resistojets.

REQ-NM-F: Functional requirements

REQ-NM-F-1 The numerical model shall predict the the outlet temperature of the fluid.

REQ-NM-F-1.1 The numerical model shall predict the power lost to the environment by radiation.

REQ-NM-F-1.2 The numerical model shall predict the power conducted to mounting interfaces.

REQ-NM-F-1.3 The numerical model shall predict the power transferred to the fluid by convection.

REQ-NM-F-2 The numerical model shall predict the temperature distribution of the heating chamber.

REQ-NM-F-2.1 The numerical model shall predict the temperature distribution along the casing walls.

REQ-NM-F-2.2 The numerical model shall predict the temperature distribution along the fluid inside of the channels.

REQ-NM-F-3 The numerical model shall accept variable input parameters.

REQ-NM-F-3.1 The numerical model shall predict the performance of the heating chamber for varying operating pressures.

REQ-NM-F-3.2 The numerical model shall predict the performance of the heating chamber for varying operating mass flow rates.

REQ-NM-F-3.3 The numerical model shall predict the performance of the heating chamber for varying inlet fluid temperatures.

REQ-NM-F-3.4 The numerical model shall predict the performance of the heating chamber for varying power inputs.

REQ-NM-F-3.5 The numerical model shall predict the performance of the heating chamber for varying mounting interface temperatures.

In terms of performance requirements, only the accuracy of the results has been defined, see REQ-NM-P-1. This requirement applies to all of the results as prescribed by the functional requirements. For example, the outlet temperature prediction should be within +/- 10 % of the real value. The value of 10 % was chosen as it is precise enough to allow to draw conclusions from results, while not being unrealistically demanding of a simple numerical model based on many assumptions.

REQ-NM-P: Performance requirements

REQ-NM-P-1 The numerical model shall be accurate to +/- 10 %.

Finally, the numerical model needs to be able to simulate the type of heating chamber relevant for resistojets. This means it should be able to represent tubular concentric heating chambers heated by a central electrical heater. This is reflected by the design requirements, REQ-NM-D-1 to REQ-NM-D-4.

REQ-NM-D: Design requirements

REQ-NM-D-1 The numerical model shall be able to represent heating chambers using a central electrical heater as the heat source.

REQ-NM-D-2 The numerical model shall predict the temperature measured at the heat source.

REQ-NM-D-3 The numerical model shall be able to represent tubular concentric heating chambers.

REQ-NM-D-4 The numerical model shall be able to represent heating chambers made out of common AM materials.

5.3. Model development

In this section, the development of the numerical model used for the simulation of concentric tubular heating chambers is presented. The model was developed in Python. The decision to use this language was based on the fact that the model was not expected to be too computationally expensive and thus did not warrant a faster programming language. Furthermore compared to MatLab which could also have been used, Python, being free and open source makes the model more accessible to any researchers who would like to experiment with it or develop it further. In this section, first the simplifying assumptions that allow the model to not be too computationally demanding are introduced, followed by explanations on how the heat transfer modeling was implemented. Finally, the main functionalities of the model are explained along with the required inputs and generated outputs.

5.3.1. Simplifying assumptions

When developing the numerical model, of the most important steps was to make the right assumptions that would make the model simple enough to not be too resource intensive to run and time demanding to develop, while still producing sufficiently accurate results.

The first simplifications that can be made are related to the geometry. Since the heat exchanger is axially symmetrical, it could be simplified to a two dimensional geometry. However, this can only be done if there is only axial and radial flow but no tangential flow. The tangential inlet and spiral in the outer layer pose a problem in that regard. While the spiral and resulting tangential flow will increase the velocity magnitude of the flow, it should not affect the axial velocity in the first layer. Indeed, a particle of water should take the same amount of time to travel from the inlet to the outlet of the first layer regardless of whether it is traveling along a channel with or without a spiral, as long as the mass flow rate is the same in both cases. Thus, ignoring the spiral in the heating chamber and assuming that the propellant is flowing axially through the first layer does not change the amount of time a particle spends in the outer layer, meaning that it also does not affect the heat it receives from the walls. So, one can make the simplifying assumption that the flow is two dimensional.

Furthermore, since the channels are very narrow, one can also assume that for any given axial position along a channel the fluid has uniform properties. If one now also ignores the short radial portions and corners of the flow path one can make the flow pseudo one dimensional, with only the cross-section of the channel changing when going from one layer to the next. Similarly one can also assume that for any given axial position along a channel the walls have a uniform temperature, meaning that the inner and outer walls of a channel have the same temperature distribution. While there should be a temperature gradient from the inner to the outer wall, given the small wall thickness and channel width, one can assume that the heat transferred through the water and radiated from one wall to the other should be enough to keep this gradient negligible.

By assuming that the flow is one dimensional, one already overlooks the local effects of turbulences. One can however even further simplify the problem by assuming laminar or even inviscid flow. This assumption should be acceptable, because the mass flow rate and thus also the flow velocity are very low and the channel dimensions are very small, meaning that the Reynolds number will also be small. Therefore no turbulences and a negligible pressure drop should be expected, justifying the assumption of inviscid flow. This also means that one can assume that the pressure is constant throughout the heating chamber.

Since the pressure is constant and the fluid properties are assumed to be uniform at any given axial position, one can assume that the fluid properties only vary along the flow path as a consequence of the heat input. Thus, one can tie all of these local properties to the enthalpy of the fluid. This makes it possible to simplify the phase transition and assume that during the boiling process, the flow properties are simply the weighted average of water and steam at the saturation temperature, with the weights being dependant on the enthalpy.

A few assumptions can also be made with regard to the heat transfer. The only heat transfer mechanisms that should be considered are the conduction through the heater walls and from the heater to its mounting points, the radiation from the outer heater wall to the environment, the radiation between the layers (grey body radiation) and the convection between the fluid and channel walls. For the radiation between the layers it is assumed that the chamber walls can be modeled as infinite cylinders. Furthermore, for the convection, a constant Nusselt number is assumed. Additionally, the only heat input that the heater receives is a constant heat flux. Finally, the last assumption is that the heating chamber is operating at thermal steady state, meaning that the temperature distribution inside the chamber is not time dependent. This assumption is valid if the thruster is given sufficient time to reach an equilibrium temperature and if no transient effects, such as boiling point fluctuations occur. However, given the much larger timescale it takes for the casing walls to change temperature compared to the time it should take for the boiling point to move, this assumption should even stay valid in the case of rapid oscillations in the flow properties.

5.3.2. Heat transfer modeling

When looking at the cross-section of a tubular concentric heat exchanger as designed in chapter 4 and shown in fig. 5.1, one can see that the propellant flows inwards from the bottom of the outer layer, up and down the channels to the central chamber outlet, corresponding with the nozzle inlet. The heat meanwhile flows from the centrally located heater, outwards along the walls, to the bottom of the outer layer, where the mounting interface with other components of the propulsion system is located. This is illustrated in fig. 5.1a and fig. 5.1b. Since both the heat and propellant essentially flow along the same path, but in opposite directions, one can model the heating chamber as shown in fig. 5.2a. In this model each channel and its inner and outer wall is represented by a single axially oriented line.

(a) Heating chamber section cut view with flow path highlighted by light blue arrows

(b) Heating chamber section cut view with heat conduction path highlighted by red arrows

Figure 5.1: Section cut view of the type of heating chamber simulated by the numerical model, with propellant channels (blue), heating element (green) and gaps between layers (yellow)

To make this very simplified model even easier to model, at first only the heat input and conduction are taken into account. This is illustrated by the schematic in fig. 5.2b. In this case a distributed heat input is applied to the central layer to represent a heat source, this heat is being conducted along the axial channel walls and exits the system at the mounting interface. Since there is no power source at or before the outlet, the conducted power at this location is zero. Due to the absence of any other forms of losses, all of the power supplied by the heater, leaves the system at the mounting interface / inlet. So, at this point, the two unknowns are the temperature of the wall at the inlet and outlet. If either one of these is known, one can determine the other one by integrating the heat conduction equation, see eq. (2.11), along the heat path. One thus needs to fix one of these temperatures as a boundary condition. During the development of the model it was judged that it would be easier to estimate realistic

inlet temperatures and experimentally it should also be easier to set the inlet temperature or at least monitor it, by setting the temperature of the system the chamber is mounted to. For this reason, the inlet temperature was chosen as the additional boundary condition.

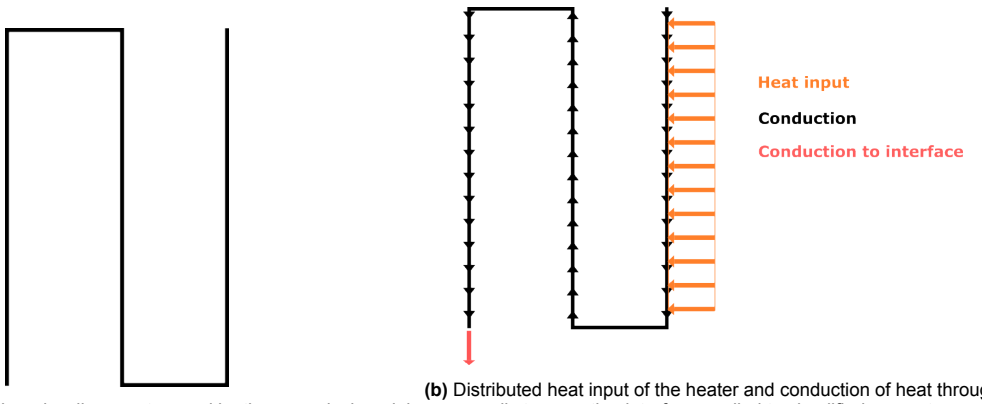

(a) Simplified flow path and wall geometry used by the numerical model

(b) Distributed heat input of the heater and conduction of heat through walls to mounting interface applied to simplified geometry

Figure 5.2: Schematic representation of simplified geometry and heat transfer mechanisms used by the numerical model

While at this stage, one can still easily solve the problem analytically, once the other heat transfer mechanisms are introduced this becomes much more challenging. Hence why numerical integration of the temperature distribution is needed and can already be introduced. To numerically solve the temperature distribution, the layers of the heat path shown in fig. 5.2a are divided into N elements of length $dx = L/N$, where L is the total length of the layer. Starting with the first element at the inlet, its temperature is set as prescribed by the boundary conditions and the power being conducted through it is set equal to the total input power. Using eq. (5.1), where q_i, k_i and A_i are the conducted power, thermal conductivity and cross-sectional surface area of the element, the temperature of the next element can be determined. For the first two layers q_i remains constant and only $A_{cross,i}$ changes at the layer transition, while k_i can optionally be made temperature dependent. For the inner layer, once the elements are within the area of the distributed heat source, the conducted power for each subsequent element can be determined with eq. (5.2), where P_{heater} is the total input power supplied by the heater and L_{heated} is the length over which the heater is acting.

$$T_{i+1} = T_i + \frac{q_i \cdot dx}{k_i \cdot A_{cross,i}} \tag{5.1}$$

$$q_{i+1} = q_i - q_{heater,i} = q_i - \frac{P_{heater} \cdot dx}{L_{heated}} \tag{5.2}$$

Having the temperature distribution throughout the heating chamber purely based on conduction is however not very useful, since it does not account for any losses and for the transfer of heat to the fluid. So, the next step is to add the effect of external radiation. This effect is only applicable to the outer layer. The power radiated away by each element can be computed with eq. (5.3), where $A_{ext,i}$ is the external surface area of an element and $T_{ambient}$ the ambient temperature. Still integrating from the inlet to the outlet, the conducted power can now be found with eq. (5.4) in the outer layer, it then remains constant in the second layer, until eq. (5.2) is again applied in the inner layer.

$$q_{rad,ext,i} = \sigma \cdot \epsilon \cdot A_{ext,i} \cdot (T_i^4 - T_{ambient}^4) \tag{5.3}$$

$$q_{i+1} = q_i + q_{rad,i} \tag{5.4}$$

The fact that power is now being lost however means that the conducted power in the inlet element is not equal to the total input power anymore but is in fact an unknown that needs to be solved for. This can be done iteratively by choosing an interval of realistic inlet powers, taking its middle value as a first guess for the inlet power and solving for the temperature and conducted power distributions. If the power at the outlet is found to be positive, the initial guess was too high, so the range can be reduced to its lower half and the process repeated. In the case of a negative value, the opposite is

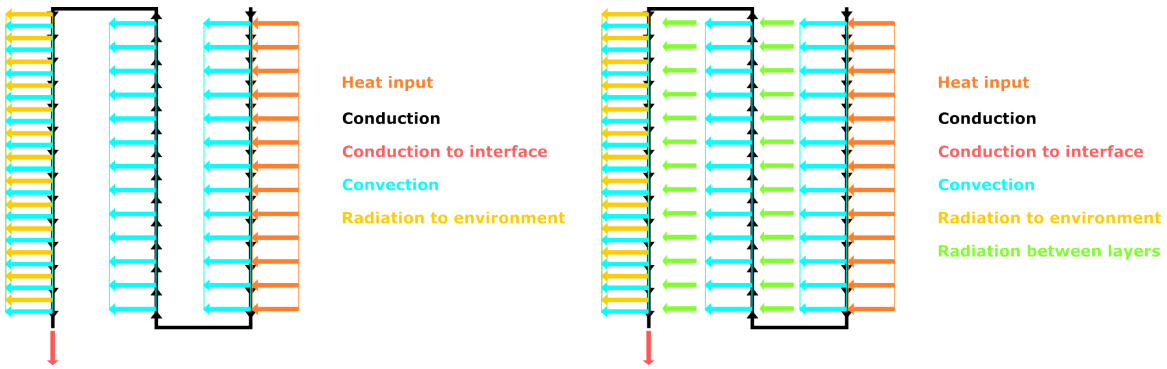

(a) Convective heat transfer and radiation to environment applied to simplified geometry

(b) All heat transfer mechanisms including inter-layer radiation applied to simplified geometry

Figure 5.3: Schematic representation of simplified geometry and all heat transfer mechanisms used in the numerical model

done. This is repeated until the interval has been reduced to an acceptably small size or the magnitude of the residual power at the outlet is below a certain threshold. The last inlet power guess is then the approximate boundary condition for the power conducted to the mounting interface. This iterative approach to solving the boundary condition is illustrated by the flow diagram shown in fig. 5.4.

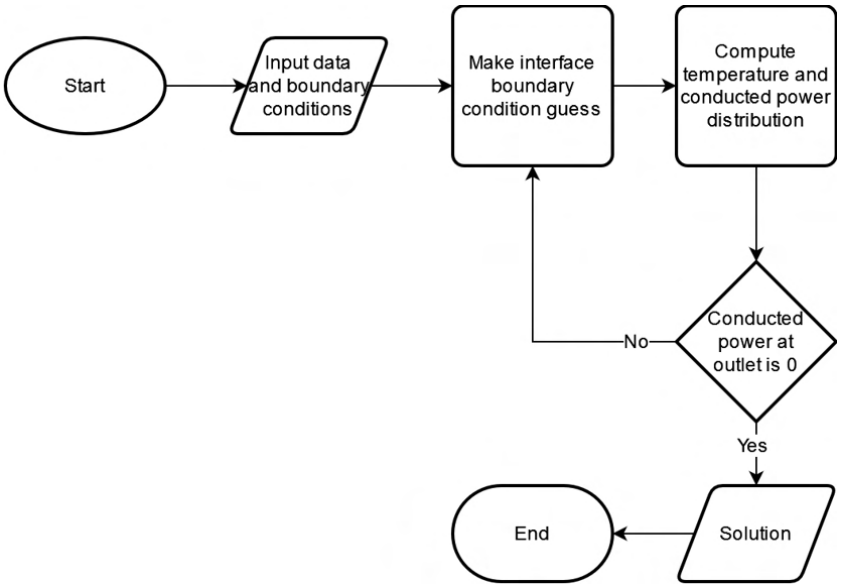

Figure 5.4: Flow diagram of numerical model including the iteration loop required to solve for inlet conditions

Convection can be taken into account via eq. (5.5), where h, the convection coefficient can be obtained with eq. (2.16), $A_{channel,i}$ is the surface area of channel wall in contact with the fluid and $T_{fluid,i}$ is the temperature of the fluid at the current element. This however means that the temperature of the fluid and its thermal conductivity (to compute h) need to be known. This can be achieved by keeping track of the enthalpy of the fluid as a reference property and determining the temperature, conductivity and any other necessary properties as a function of the enthalpy. By specifying a starting enthalpy, obtained from the inlet temperature of the fluid, as an additional boundary condition, one can then compute the enthalpy of each subsequent fluid element with eq. (5.6). So, now for each element three properties need to be computed, the wall temperature, the conducted power and the fluid enthalpy. By knowing the fluid enthalpy and converting it to the fluid temperature distribution, one can now also determine the outlet fluid temperature and thus the performance of the chamber.

While one could use theory based or empirical relations between the fluid enthalpy and the other properties to obtain the desired values at each step, it was decided to instead use data collected from the NIST (National Institute of Standards and Technologies) Chemistry WebBook [29, 14]. This was

achieved by saving the isobaric properties of the propellant at 1 K intervals over a range of expected temperatures and using linear interpolation to obtain the values at the exact enthalpy that is needed.

$$q_{conv,i} = h \cdot A_{channel,i} \cdot (T_i - T_{fluid,i}) \tag{5.5}$$

$$H_{fluid,i+1} = H_{fluid,i} + \frac{q_{conv,i}}{\dot{m}} \tag{5.6}$$

Conduction along the heat exchanger is expected to be the dominant heat transfer mechanism responsible for dissipating the heat from the inside of the chamber to the outside. Thermal radiation from the outer wall of the inner layer to the inner wall of the intermediate layer and from the outer wall of the intermediate layer to the inner wall of the inner layer will however also have an impact. This is illustrated by fig. 5.3b, which includes all of the heat transfer mechanisms taken into account by the model. As previously stated, for the internal radiation the chamber walls are assumed to be infinite cylinders. This assumption is reasonable given the small size of the space between the walls compared to their length. The heat transfer is assumed to only occur from one element to the adjacent element. This means that for an element in the first layer, the radiated power can be obtained with eq. (5.7), where $A_{in,i}$ is the surface area of the element in question facing the adjacent element, T_{adj} is the temperature of the adjacent element, r_i is the inner radius of the element in question and r_{adj} is the outer radius of the adjacent element in the second layer.

$$q_{rad,in,i} = \sigma A_{in,i} \frac{(T_i^4 - T_{adj}^4)}{\frac{1}{\epsilon} + \frac{1-\epsilon}{\epsilon}\frac{r_i}{r_{adj}}} \tag{5.7}$$

So, to summarize, the temperature of an element can still be obtained from eq. (5.1), the enthalpy of the fluid from eq. (5.6) and the conducted power is determined with eq. (5.8), where $q_{rad,out,i}$ is the equivalent of $q_{rad,in,i}$, but when an elements radiates heat away to an element in the outer adjacent layer rather than the inner one, i.e., from layer three to layer two. Of course for some elements certain terms of eq. (5.8) are zero, like, e.g., $q_{heater,i}$ for any elements in the first and second layers.

$$q_{i+1} = q_i - q_{heater,i} + q_{rad,ext,i} + q_{conv,i} + q_{rad,in,i} + q_{rad,out,i} \tag{5.8}$$

The addition of the radiation between layers poses a problem for the numerical integration. Indeed, without internal radiation, the solver can start at the first element and sequentially compute the properties of the next elements to obtain the temperature distribution. In this way, aside from the boundary condition problem requiring iterations described earlier, the first element is independent from all other elements, the second one is only dependent on the first one, the third one only directly on the second one etc. With the addition of internal radiation however, the first element is already dependent on the temperature of an element in the second layer, which is still unknown when solving for the first element.

To solve this problem, the model was coded so that it first computes the complete temperature distribution of the chamber without internal radiation. This distribution is then used as a starting point for computing a second solution with internal radiation. In this second solution, the model uses the temperature from the first solution to compute the radiation between two adjacent elements. A third solution can then be computed by using the second one as a starting point and this can be repeated until the temperature distribution converges to its final solution.

Unfortunately, when implementing this solving method, it quickly became apparent that the solution was not converging, but oscillating between extreme values, while the real solution is likely an average of these extremes. In an attempt to prevent the solution from overshooting the real solution, a relaxation factor was introduced. When iterating from one temperature distribution to the next, rather than taking the new distribution as the input for the next one, a weighted average of the old and new solutions is used. This is illustrated by eq. (5.9), where T_{new} is the temperature distribution that will be used as an input for the next iteration, $T_{current}$ is the solution of the current iteration, $T_{previous}$ the input used to obtain the current solution and Rf the aforementioned relaxation factor.

$$T_{new} = Rf \cdot T_{current} + (1 - Rf) \cdot T_{previous} \tag{5.9}$$

When keeping the relaxation factor sufficiently low, the solution was able to converge, although at a slow rate. With the addition of internal radiation, the model becomes a bit more complex. Indeed now

to obtain a solution, it has to start out with a guess for the conducted power at the inlet, perform the iterations to solve for the internal radiation, update its inlet power guess, perform new internal radiation iterations, etc. until the solution has converged, both in terms of temperature distribution and inlet power. This solving process with two layers of iterations is illustrated by fig. 5.5.

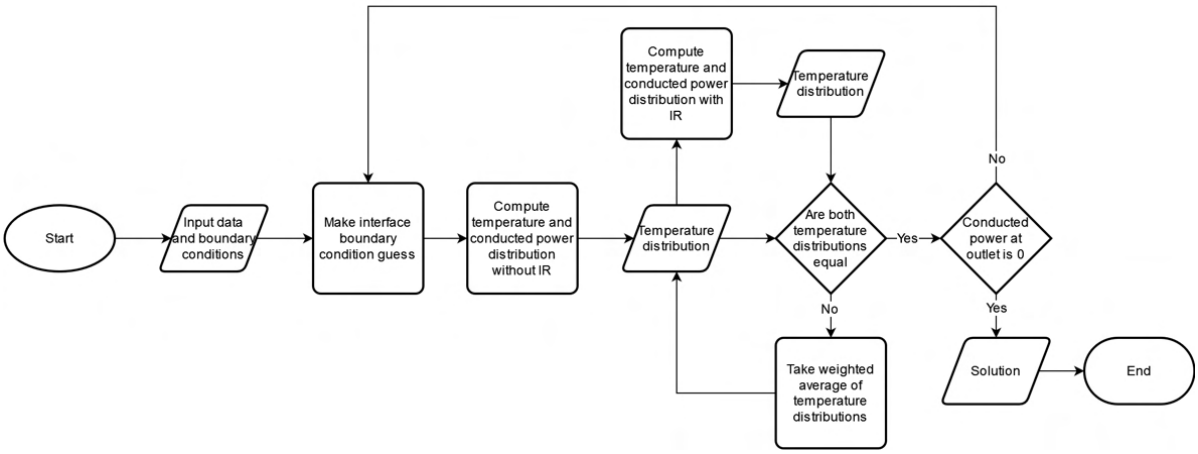

Figure 5.5: Flow diagram of numerical model including the two levels of iteration loops required to solve for internal radiation and inlet conditions

5.3.3. Model functionalities

As prescribed by the requirements, the numerical model allows the user to define the boundary conditions to reflect different operating conditions. By importing different sets of reference data retrieved from the NIST WebBook, he/she can for example configure the model to run at different operating pressures or with different propellants. The model also allows for the simulation of heat exchangers with different geometries. One can set the number of concentric layers, their lengths, the wall thickness, channel width and spacing between the layers. Additionally, the user can also define the dimensions of the heater, the area over which the heat is supplied and the amount of power that is supplied.

To explore the effects of the different heat transfer mechanisms, the model also allows those mechanisms to be selectively turned on or off. This is particularly useful for the internal radiation. Indeed, the addition of the iteration loop to solve for radiation considerably increases the time it takes to get a solution, while not always having a significant impact on the outcome. Therefore, being able to neglect the internal radiation can be very valuable during design exploration phases where the accuracy of results is less crucial.

The user can of course also define material properties such as the emissivity and thermal conduction as well as boundary conditions. The boundary conditions that can be set include the fluid inlet temperature and mass flow rate, the ambient temperature and either the temperature or the conducted power at the mounting interface. Finally, one can also define the number of elements per layer and the limit used to check the convergence of the iteration loops.

As main outputs, the model produces the temperature distribution of the heater walls and fluid, as well as the distribution of conducted power. From these results it extracts the outlet temperature, heat exchanger efficiency and losses. Furthermore, the numerical model has been set to also output four plots by default. These plots show the temperature, conducted power, phase and convected heat plotted against the path length. This is illustrated by fig. 5.6 which shows one such set of plots with arbitrary input parameters.

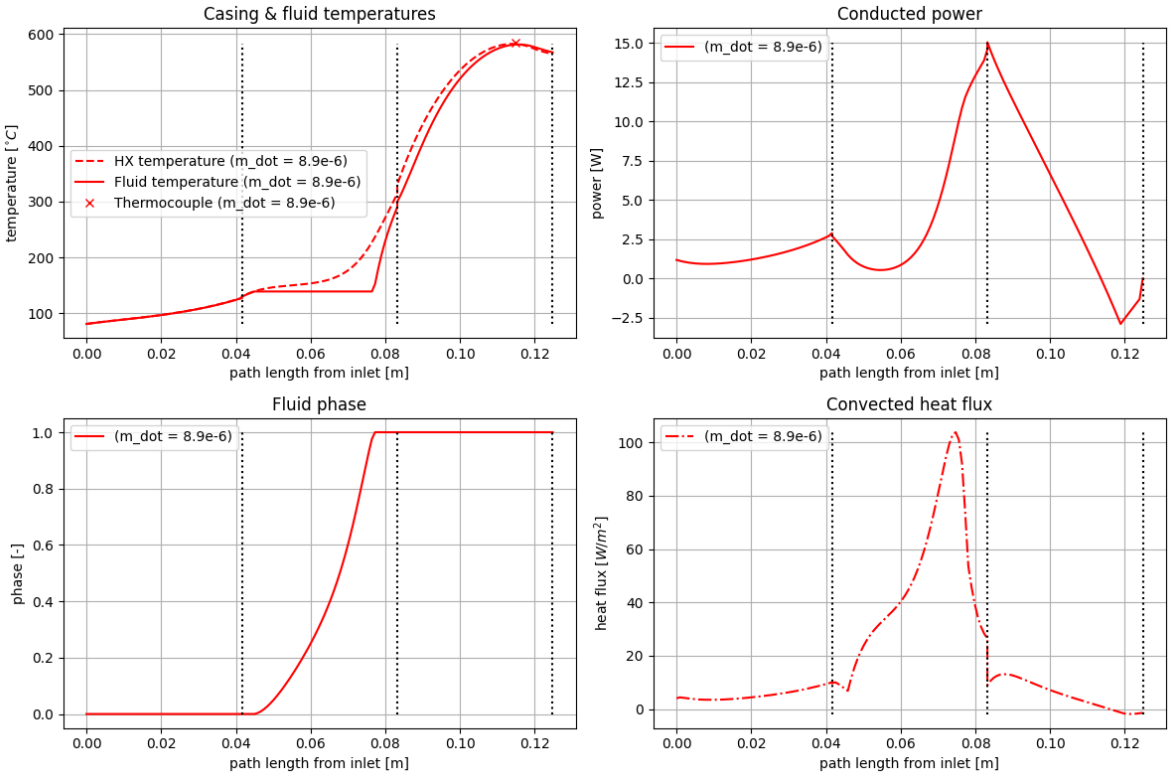

Figure 5.6: Typical output plots that can be generated by the numerical model, showing the fluid and wall temperature, conducted power (> 0 means flow from outlet to inlet), phase (0 = water, 1 = steam), and convected heat distributions

5.4. Verification, validation and sensitivity analysis

In this section the verification and validation process of the numerical model is detailed. Additionally, a sensitivity analysis is also presented.

5.4.1. Verification

The first step in the verification process of the numerical model is to ensure that the energy balance of the results produced by the model is correct. If one considers the case illustrated by fig. 5.6 as a verification example one can verify that the losses and energy transferred to the fluid add up to the 32 W defined as an input power. For this case, the model predicts an efficiency (power transferred to the fluid / input power) of 91.7 %, which is equivalent to 29.34 W. The predicted losses are 2.98 W via radiation and −0.317 W via conduction. The negative value means that at the mounting interface the chamber is colder than the defined interface temperature of 80 °C and heat is being transferred to the chamber. Adding up those values, the total power output is 32 W. Furthermore, in this exercise, with a specified mass flow rate of 8.9 mg/s an inlet temperature set to 80 °C the model predicts an outlet temperature of 567.3 °C. This is equivalent to an enthalpy change from 323.44 to 3631.4 kJ/kg for water at 3.5 bar. With the aforementioned mass flow rate one can compute that the power input into the propellant is 29.4 W, which is only 0.34 % off from the value obtained when using the efficiency. This minor difference is likely due to rounding errors or inexact convergence of the solution during either one of the iterative loops.

Another simple verification of the numerical model can be done by checking the boiling temperature. For example, for water at 3.5 bar, the saturation temperature is 139 °C. When looking at fig. 5.6, one can see that this is exactly the value at which the fluid temperature stagnates over a certain distance, while the phase goes from liquid to gaseous. Based on these two simple verifications, the power balance and boiling temperature, one can determine that the numerical model appears to produce plausible results.

The next step in verifying the numerical model is to check if the number of elements in each layer is sufficiently high and the convergence criterion sufficiently low. The convergence criterion is the limit

that is applied to both the internal radiation iterations and the inlet power iterations. Simulations with the same input settings and different values for the convergence criterion were performed. The values are 10^{-1}, 10^{-2} and 10^{-3}. As can be seen from the results shown in fig. 5.7, the convergence criterion has a very limited impact on the results. However, it was noticed that in some cases when the convergence criterion was set to 10^{-1}, the solution did not fully converge. This is likely due to the fact that the loose convergence criterion for the inner radiation loop allowed for too much fluctuation between the solutions and prevented the main inlet power iterations from converging. Thus, it was decided to set the convergence criterion to 10^{-2} for all subsequent simulations.

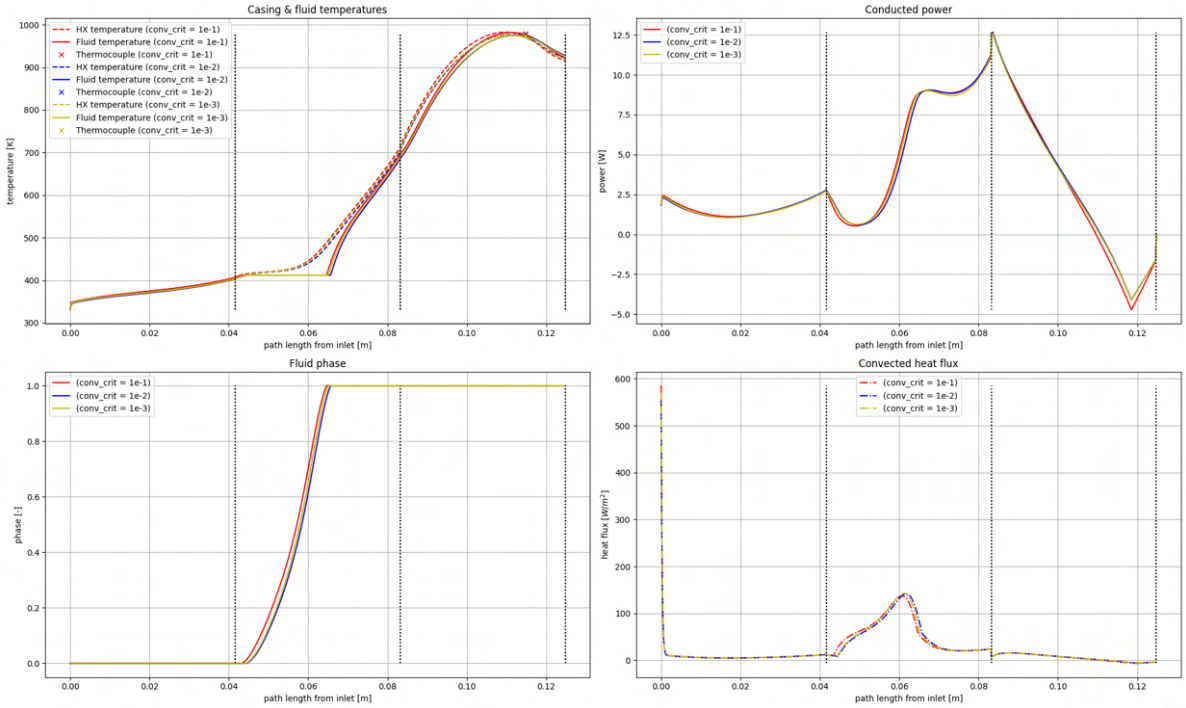

Figure 5.7: Results from simulations with varying convergence criterion values used in the verification process

For the number of elements, the same simulation was performed with 50, 100, 200, 400 and 800 elements per layer. The results are shown in fig. 5.8. As can be seen from those plots, the results are once again relatively close for all five cases. However, one can also see that there is a noticeable change when going from 50 to 100 to 200 elements while between 200, 400 and 800 elements the change is really minimal. From this one can conclude that for quick simulations that do not require the highest accuracy, 50 elements are sufficient. For simulations requiring better accuracy 200 elements are recommended, while higher element counts do not really add any benefits. This concludes the verification of the convergence and mesh size verification.

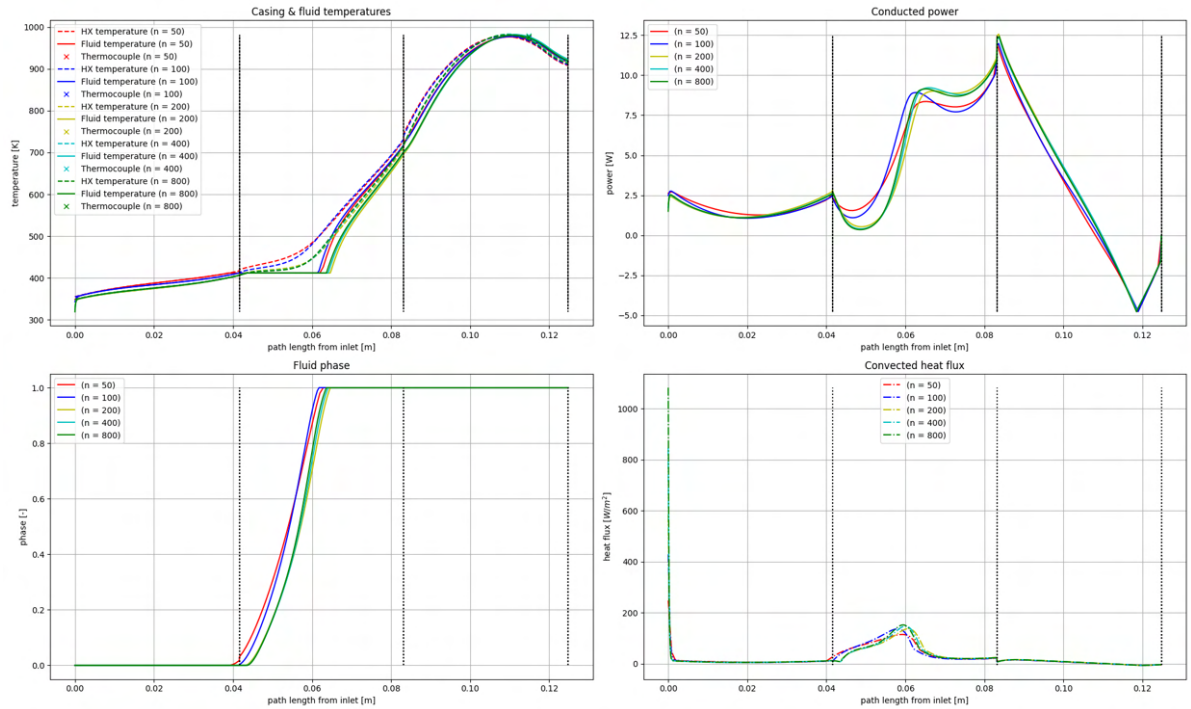

Figure 5.8: Results from simulations with varying numbers of element per layer to verify mesh convergence

Finally, the last step of the verification process is to compare the results generated by the custom in house model to results produced by an already verified general purpose simulation suit. ANSYS Fluent was chosen for this purpose. However, due to the difficulty of obtaining meaningful results from simulations including the phase transition, it was decided to limit the verification with ANSYS to purely gaseous flow. The input parameters used for the AM heating chamber in the numerical model and replicated in the ANSYS simulation are summarized in table 5.1. While relying on fewer assumptions, the ANSYS simulation still contains a number of simplifications to allow it to be solved with the moderate computing power that was available. So, the heating chamber was simulated in two dimensions with an axial symmetry, thus also neglecting the spiral in the outer layer. Furthermore, the flow was defined as being laminar. The mesh size was first set to 0.05 mm before being reduced to 0.025 mm. By comparing the results of these two simulations mesh convergence of the ANSYS model was verified. The residuals were set to 10^{-7}, allowing the temperature distribution to converge to its final solution shown in fig. 5.10.

Table 5.1: Operating and boundary conditions used for the verification case in both the ANSYS Fluent and Python models

Parameter	Value	Unit	Parameter	Value	Unit
number of channels	3	$[-]$	pressure	3.5	$[bar]$
channel length	41.6	$[mm]$	mass flow rate	9.63	$[mg/s]$
wall thickness	0.8	$[mm]$	conducted power at inlet	0	$[W]$
channel width	0.5	$[mm]$	inlet fluid temperature	450	$[K]$
layer spacing	1.2	$[mm]$	ambient temperature	293	$[K]$
heated section length	34.7	$[mm]$	emissivity	0.7	$[-]$
input power	40	$[W]$	wall conductivity	11.34	$[W/(m \cdot K)]$

As can be seen from fig. 5.10, the velocity remains quite low throughout the heater, only reaching a maximum of 1.94 m/s. The Reynolds number was also verified with the ANSYS results and it reaches a maximum of 2.72 meaning that the laminar flow assumption is justified. Furthermore the predicted pressure drop is only of 55 Pa or 0.016 % confirming that the inviscid and constant pressure assumptions are also valid.

Figure 5.10 shows the temperature distribution taken at the center of the axial channels of the AN-

SYS solution compared to the fluid temperature distribution predicted by the in Python model. Overall, the agreement between the two models is good. Especially the outlet temperature, which is probably the most important aspect, is very close for both cases with ANSYS predicting 1022 and the in house model 1016, so, only a 0.6 % difference. Where both models differ a bit more is in the first and particularly in the second layer. Part of the reason for these differences is that the ANSYS model also takes into account the flow and heat transfer in the radial channel sections, while the in house model does not. So, a possible future improvement of the model developed for this project would be to add the ability to simulate the radial channels. However, if one ignores the first three millimeters where the low temperature and rapid temperature increase cause larger relative differences between the models, the maximum relative difference occurs right before the transition from the second to the third layer and peaks at 6.6 %, so well within the accuracy specified by the requirements.

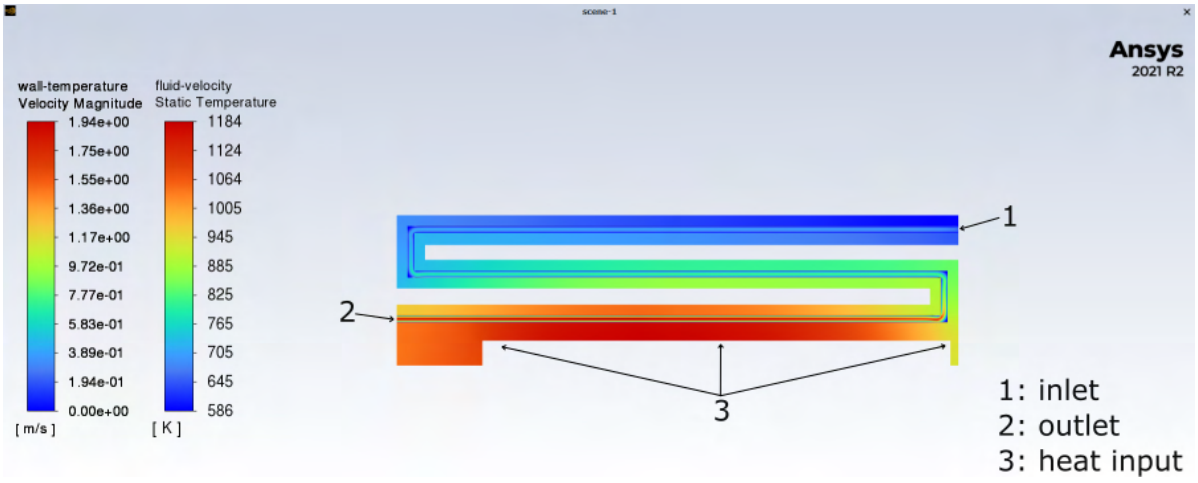

Figure 5.9: Solution generated by ANSYS Fluent for a 3 layer heating chamber with purely gaseous flow

Unfortunately, it was not possible to generate a similar simulation with water flow at the inlet and a phase transition from liquid to gaseous in ANSYS. Thus the model could not be fully verified with an already verified CFD (Computational Fluid Dynamics) software. Instead, it was judged that the successful verification of the model with only steam was sufficient, as validation of the model with experimental data would make up for the lack of further verification with liquid propellant.

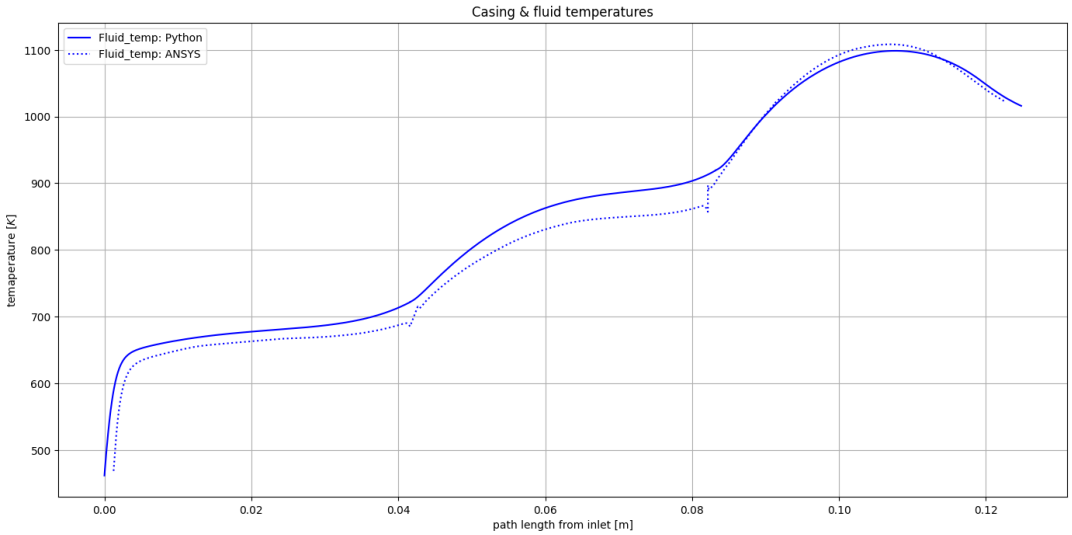

Figure 5.10: Plot showing the comparison between the fluid temperature distribution obtained from the ANSYS Fluent and in-house models

5.4.2. Validation

Comparing the results from the numerical model to ANSYS can provide useful insights and is a good indicator for the correctness of the results generated by the model. However, the ANSYS simulation used for comparison is still based on many assumptions and uses the same boundary conditions as for the model developed in house. In reality these assumptions and boundary conditions might not be applicable, meaning that the simulations are not able to produce representative results. Thus, it was decided that a better way to validate the model would be to perform a series of tests, replicate the test conditions in the simulation and compare the results.

One of the important considerations that has to be made to ensure the simulation and experiments are comparable is that the simulations are only valid for thermal steady state. Thus the tests would also need to be performed at steady state. This can only be achieved if the tests can be performed for long enough to allow the chamber to settle to an equilibrium temperature, following the initial start-up transient.

With the available test setup, longer tests were not possible without the need for modifications of the GSE, which, due to time constraints were not feasible. This means the numerical model is not yet validated. One of the recommendations for work on this topic would thus be to perform thrusts of a longer duration and validate the model.

5.4.3. Sensitivity analysis

Even with a validated numerical model, there can still be differences between the simulation results and empirical measurements if the input values do not precisely match the test conditions. This can be problematic, since it can sometimes be difficult to determine some of these input values with a high degree of precision. It was therefore decided to perform a sensitivity analysis of the input parameters where measurement uncertainty is to be expected. This should also be useful to gain an understanding on the impact that each parameter has an how it can be used to tune or improve a thruster's performance.

For this sensitivity analysis, one parameter was changed at a time in a range around a reference value. For most parameters this meant either a −20 to 20 % or −10 to 10 % range around the reference value, depending on the expected difficulty of controlling or measuring the given parameter during testing. For the temperatures used as input parameters variations of −10 to 10 K were used and for the emissivity the values 0.5, 0.6, 0.7, 0.8 and 0.9 were used. Table 5.2 shows the absolute and relative changes in outlet temperature that this resulted in.

From table 5.2 one can see that the two parameters that have the largest impact are clearly the mass flow rate and the input power, with changes in outlet temperature exceeding 15 %. This is followed by the emissivity and thermal conductivity of the chamber which have at most a 1 to 2 % effect. Finally, the remaining parameters seem to have a marginal, almost negligible effect. As previously mentioned, the Nusselt Number is a parameter that is hard to estimate or measure. So, seeing that it has a limited impact on the performance of the chamber means that even if the chosen value of 3.66 is not accurate, the results of the model should still be valid.

The significant impact of changing the mass flow rate should be kept in mind when comparing test results to simulation results. This is particularly important for the tests presented in this report, as the mass flow rate was not measured and only an approximate average value was used. In terms of performance optimization, the effect of the mass flow rate observed during the sensitivity analysis means any increase of the mass flow rate is highly detrimental to the outlet temperature and thus I_{sp}. However, it was also noted that the efficiency of the chamber increased when increasing the mass flow rate, as the lower temperatures helped reduce any thermal losses. Indeed, when reducing the mass flow rate by 20 % the efficiency went from 95.5 % to 98.7 %, while when the mass flow rate was decreased by 20 % it dropped to 80.5 %.

The sensitivity of the outlet temperature to the input power should pose less of a problem for simulation and test result comparisons, as the input power is easier to record accurately. However, the rapid drop in outlet temperature when reducing the power by 10 % signifies that failing to supply the required amount of power will have a detrimental effect on the propulsion system performance.

Table 5.2: Sensitivity analysis: variation of input parameters and impact on outlet temperature

Emissivity $[-]$	Outlet temperature $[K]$	Relative difference [%]	Conductivity [%]	Outlet temperature $[K]$	Relative difference [%]
0.5	919.4	3.71	-20	938.1	1.10
0.6	905.1	2.10	-10	931.1	0.34
0.7	886.5	0.00	0	927.9	0.00
0.8	864.1	-2.53	10	922.8	-0.55
0.9	860.3	-2.96	20	917.8	-1.09
Mass flow rate [%]	Outlet temperature $[K]$	Relative difference [%]	Nusselt number [%]	Outlet temperature $[K]$	Relative difference [%]
-20	990.9	9.48	-20	907.1	0.22
-10	948.4	4.78	-10	906.2	0.12
0	905.1	0.00	0	905.1	0.00
10	812.5	-10.23	10	906.4	0.14
20	672.4	-25.71	20	906.9	0.20
Input power [%]	Outlet temperature $[K]$	Relative difference [%]	Ambient temperature $[K]$	Outlet temperature $[K]$	Relative difference [%]
-10	768.2	-15.13	-10	891.1	-1.27
-5	850.3	-6.05	-5	901.7	-0.10
0	905.1	0.00	0	902.6	0.00
5	942.4	4.12	5	902.7	0.01
10	966.9	6.83	10	904.1	0.17
Inlet wall temperature $[K]$	Outlet temperature $[K]$	Relative difference [%]	Inlet fluid temperature $[K]$	Outlet temperature $[K]$	Relative difference [%]
-10	903.2	-0.21	-10	902.2	-0.32
-5	905	-0.01	-5	904.9	-0.02
0	905.1	0.00	0	905.1	0.00
5	906.9	0.20	5	909.1	0.44
/	/	/	10	910.9	0.64

6

Prototype evaluation and testing

Following the manufacturing of the AM heating chamber prototype, this prototype was inspected and tested. The goal of this chapter is to present the inspection, see section 6.1, and testing process, see section 6.2, and their respective outcomes. Additionally an attempt at comparing the test results and simulation results obtained with the numerical model is also made in section 6.3.

6.1. Part inspection

Following the printing process, the loose powder was removed from the chamber, the part was thermal treated, the sacrificial support structures were removed from the support brackets and the holes for which tight tolerances are critical were re-drilled. This was all done by the same supplier as the printing, so the part could only be inspected once all of these steps had been completed. When asked about the powder removal process which was one of the main concerns of the manufacturing process, Materialise reported that there were no issues, the powder could easily be removed. During the inspection process, the part was also cleaned and flushed with isopropanol and no remaining powder was observed during flushing process. This means that either the addition of the spiral in the outer layer was an effective mitigation method, or it was not even necessary in the first place.

Along with the complete heating chamber a second specimen was also printed and cut in half lengthwise, allowing to inspect the inner features of the printed part. The cutting of the chamber was also done by Materialise via wire Electrical Discharge Machining (EDM). Both of these parts are shown in fig. 6.1.

To facilitate the inspection of the parts and their sub-millimeter details, a digital camera equipped with a macro lens was used to produce magnified pictures of the parts. These pictures are shown in fig. 6.1, fig. 6.8 and fig. 6.3.

During the visual inspection of the parts and pictures, no significant structural defects such as gaps or internal voids could be found. Defects too small to be seen with these methods or on the inside of the parts could still be present. To detect those, more advanced inspection methods such as Computed Tomography (CT) scans would be necessary. Due to time constraints it was unfortunately not possible to use these methods. However, the absence of visible defects is already a indicator of good structural integrity.

Additionally to looking for structural defects, some of the most crucial dimensions of the parts were also verified. This was done by measuring a reference dimension of the part, the total length, with a caliper and using it to convert the size in pixels of features as observed in fig. 6.1b to millimeters. The reference length was measured four times on the picture and on the sectioned part. These measurements, their average and standard deviation is given in table 6.1. Based on the average values, one can deduce that one pixel corresponds to 0.011 59 mm.

(a) 3D printed heating chamber after printing and machining of holes and welding surfaces but before welding of additional components

(b) 3D printed heating chamber cut in half via EDM for internal inspection

Figure 6.1: Full and half heating chambers as received from Materialise

Table 6.1: Total part length measurements taken on the sectioned part and the corresponding picture

Measurement	Length measurement from picture [Pixel]	Length measurement from part [mm]
1	4232.03	49.01
2	4232.121	49.03
3	4228.229	49.06
4	4233.617	49.06
Average	4231.499	49.04
Standard deviation	1.990457	0.021213

Measuring the size of the wall thickness on fig. 6.1b and converting it to millimeters with the newly obtained conversion factor gave the values presented in table 6.2. The measurements were performed at three different location of each wall on the left side fig. 6.1b. The left side was used because the lighting conditions on that side make it easier to distinguish the edge of the walls. The same was done for the channel width. The measurements are given in table 6.3.

Table 6.2: Wall thickness measurements taken on the sectioned part and the corresponding picture

Measurement	Length measurement from picture [Pixel]	Converted length [mm]
1	68	0.788071
2	69	0.79966
3	68	0.788071
4	66	0.764892
5	69	0.79966
6	68	0.788071
7	69	0.79966
8	69	0.79966
9	68	0.788071
10	70	0.811249
11	70	0.811249
12	68	0.788071
13	67	0.776481
14	68	0.788071
15	66	0.764892
Average	68.2	0.790388
Standard deviation	1.16619	0.013515

Table 6.3: Channel width measurements taken on the sectioned part and the corresponding picture

Measurement	Length measurement from picture [Pixel]	Converted length [mm]
1	43	0.498339
2	40.5	0.469366
3	42.5	0.492544
4	41	0.47516
5	43	0.498339
6	42.5	0.492544
Average	42.08333	0.487715
Standard deviation	0.975392	0.011304

From the measurements taken during the inspection one can thus determine that the overall part length is off by 0.082 %, the wall thickness by −1.2 % and the channel width by −2.5 %. As indicated by the length, for which the offset clearly falls within the margin of measurement error, the general dimensions of the part seem to have been reproduced accurately by the 3D printing process. The smaller features such as the wall thickness and channel width meanwhile are slightly less accurate, but still acceptable. In fact the offset is within the range of values one would expect when taking into account the roughness of the parts. Indeed the roughness of the surfaces makes it difficult to determine where exactly the edge of walls is when taking measurements from pictures. So overall, the dimensional accuracy of the AM parts is deemed satisfactory and the parts should be usable for testing.

Additionally to looking for structural defects and verifying the dimensions, using the macro pictures, the parts were also inspected for other types of manufacturing defects. One of the main defects that could be found is the outer radius of the transition from the outer channel to the intermediate channel. Given the vertical print orientation of the chamber, with the outlet facing up, the aforementioned radius lead to a small region requiring unsupported horizontal or near-horizontal printing. As can be seen in 6.2a, this has lead to a slight collapse of the powder during the printing process, locally reducing the channel width in the finished part. This slight contraction of the flow path should not have a significant impact on the performance of the part. In future designs one should however take appropriate measures to mitigate such defects. Another minor defect that could be identified on the pictures is a small protrusion on the outer wall of the intermediate layer, see fig. 6.2b. This protrusion is located in an area where the part was printed with an overhang angle of 50°, so this could have been a contributing factor. The protrusion is however not in an area where it could affect the propellant flow, so it will not have an impact on the performance. Nevertheless, it is an indication that more small defects could be present

in locations that cannot be inspected.

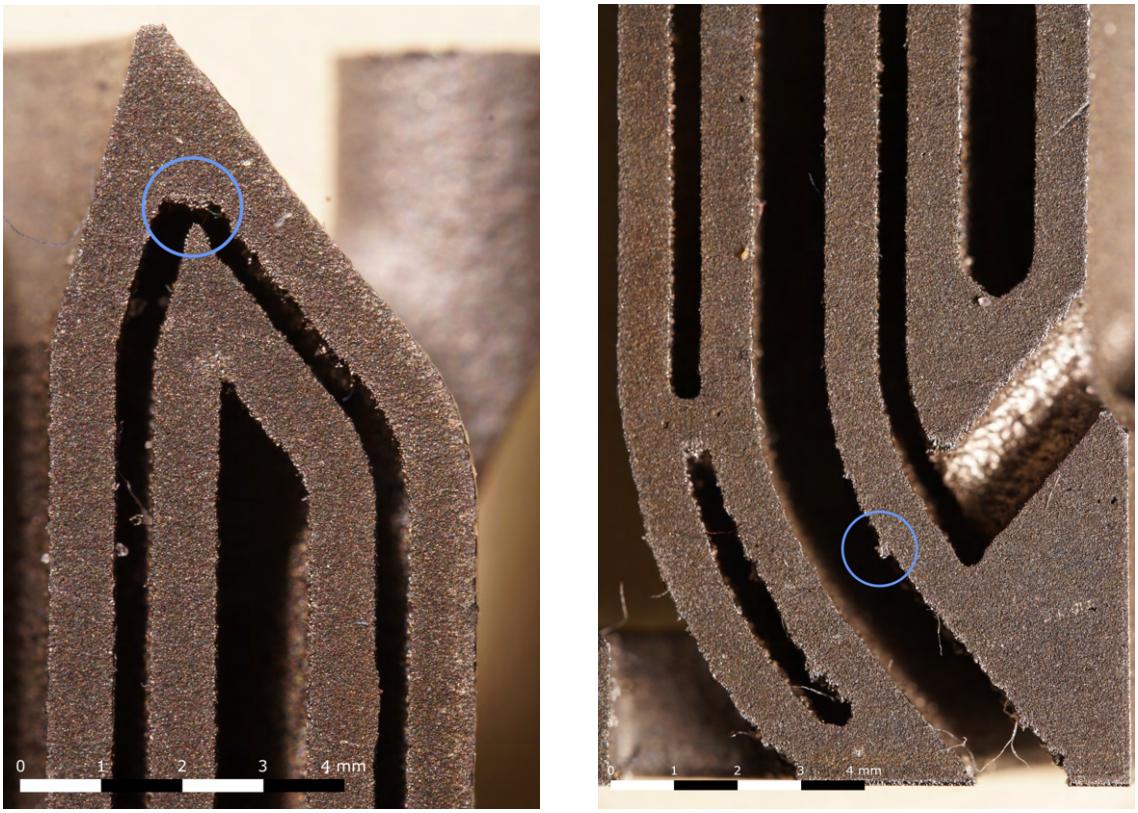

(a) Reduction of channel width due to manufacturing defect of unsupported horizontal surface (circled in blue)

(b) Protrusion on the lower side of an overhanging surface (circled in blue)

Figure 6.2: Close-up pictures of sectioned heating chamber highlighting minor printing defects

Figure 6.1a shows the inside of the outer wall of the inner channel. This picture was taken to highlight the roughness that is typical of 3D printed parts. The shiny area at the bottom of the picture was machined after the printing process, to guarantee tight tolerances at the interface between the heating element and the chamber, hence why the surface finish is much better. The rest of the part shown on this picture is however in the as-printed state. Due to the low flow velocity within the channels and the associated low Reynolds number, the surface irregularities should not be a cause for concern in this specific application.

So, to conclude this section on the inspection of the 3D printed parts, one can say that their quality is sufficient for feasibility and performance testing in the context of this project. For future prototypes a more in depth inspection, with methods allowing to inspect the internal features of the part, is recommended.

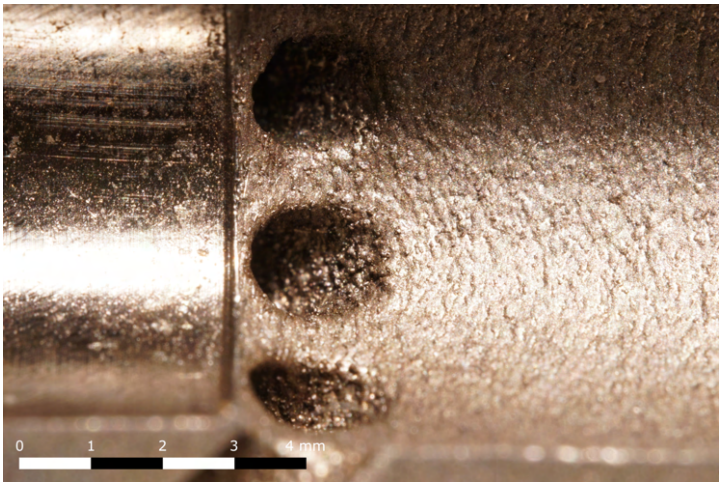

Figure 6.3: Close-up picture of sectioned heating chamber highlighting the surface roughness

6.2. Prototype testing

In this section the testing of the AM heating chamber prototype is presented. The test objective is first established before the test methodology and setup are presented. This is followed by the results and a discussion on the outcome of the tests.

6.2.1. Test objective

Before proceeding with the testing of a heating chamber prototype, it is important to define the test objectives, as this also defines how the tests are performed and which measurements are taken. Of course, the test objectives should also be in line with the research objectives of the project.

The first test objective is aimed at directly covering the first research objective by putting the functionality of the heating chamber prototype to the test. This objective can be phrased as follows: *To demonstrate the functionality of the AM heating chamber by integrating it into the test setup and using it to produce thrust.*

The second test objective should cover the second aspect of the research objective but in an indirect way. Indeed, given that the prototype design was not optimized for performance it cannot be used to directly demonstrate any performance advantages of AM designs. However, if it can be used to validate the numerical model developed during this project, the model can then be used to show the potential for advantages that AM offers. Thus the second test objective is: *To generate experimental data to validate the numerical model.*

6.2.2. Test methodology and setup

To achieve the first test objective, demonstrating the functionality of the heating chamber, the heater and nozzle need to be welded to the chamber and this assembly should then be integrated with a test bed. That bed needs to be able to provide the heater with electrical power and the chamber with pressurized water. To determine whether the chamber is functional, the thrust it produces needs to be measured. Figure 6.4 shows the full AM chamber assembly mounted on the test bed.

For the second test objective, the chamber, heater and nozzle assembly also needs to be integrated to the same test bed as for the first test objective. Additionally, to obtain data that can later on be compared to the numerical model, additional measurements need to be taken. The numerical model is designed to mainly give temperature and power consumption as its outputs. The outlet temperature in particular is one of the most important factors. Therefore, the test setup needs to allow for the measurement of the power consumption and outlet temperature. However, due to the design of the chamber channels, it is not possible to have a thermocouple located in the propellant flow at the chamber outlet. The next best option is to instead take measurements at the heat source. Additionally, a thermocouple should also be place on the chamber wall near the nozzle to have a second data point of the temperatures in this region. Additional thermocouples should be placed at various locations on the chamber walls to help validate not only the outlet temperature, but also the temperature distribution

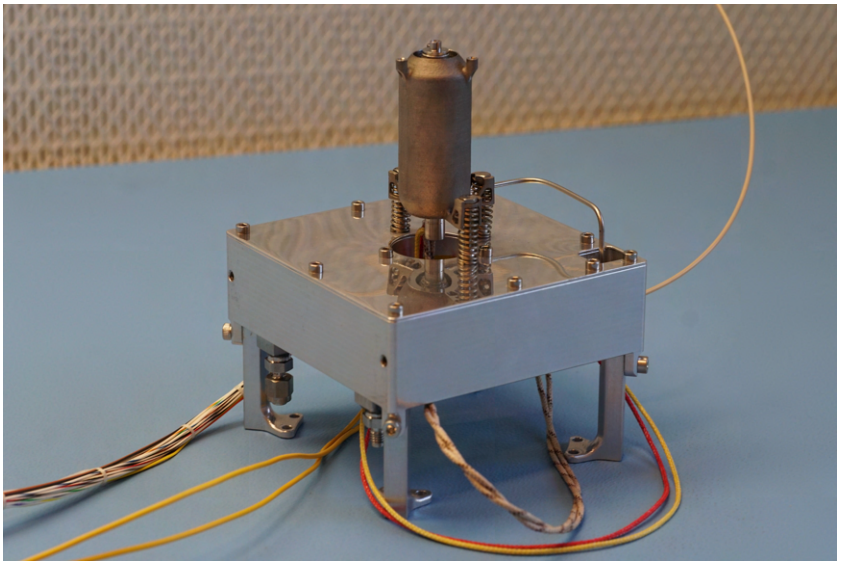

Figure 6.4: AM heating chamber prototype mounted on a test bed

throughout the chamber.

As has already been shown by the sensitivity analysis performed on the numerical model, the mass flow rate has a significant impact on the chamber performance. To ensure the test conditions can be matched in the validation simulations, the mass flow rate also needs to be recorded during testing. Along with the thrust measurements, the mass flow rate can also be used to determine the specific impulse and infer the temperature at the chamber outlet. The pressure at which the water is supplied should also be recorded, as this is also one of the input parameters of the numerical model and because it directly influences the thrust and specific impulse. It should thus be kept the same during the different test runs. Finally, for validation, it is important the measurements be taken at steady state, as the numerical model cannot simulate transient effects.

For the following test, to keep the setup simple, the tank is kept separate from the test bed. In this configuration, an external scale is used to measure the mass of the propellant and the one in the chamber is used to estimate the thrust. Furthermore, to allow for a faster pressure control, it was decided to use an external high pressure nitrogen supply coupled with a digital pressure regulator. This setup is schematically represented in fig. 6.5.

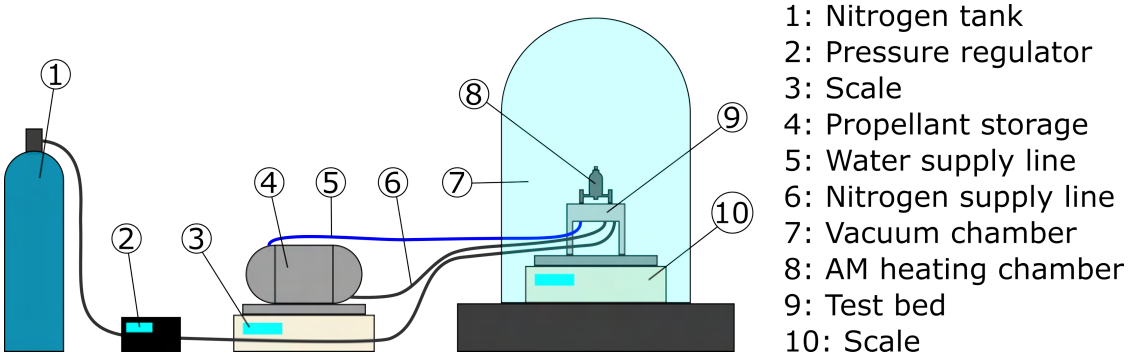

Figure 6.5: Schematic of initial two scale test setup

After initial tests it was observed that this setup would not be viable to obtain useful data. Indeed one crucial oversight that had been made during the design of the setup was that the AM heating chamber channels constitute a not insignificant volume. When the propellant supply is opened for thrusting, this volume partially fills up with water, increasing the mass of the thrust head and skewing the thrust measurements taken by the internal scale. This effect was observed during testing, as the thrust was far greater than realistically possible. Furthermore, the measurements taken by both scales

were prone to severe simultaneous oscillations. The most plausible explanation for these oscillations is that the heating chamber was subject to an unstable boiling process in which the boiling point moved back and forth within the channels. This in turn caused propellant to flow back and forth between the storage and heating chamber, increasing and decreasing their mass periodically and resulting in the oscillations observed in the scale measurements.

While it seemed highly likely that the test bed, with the integrated AM heating chamber, was producing thrust during these first tests, the effect of the additional water mass in the chamber meant that this could not be proven beyond a reasonable doubt. It was thus decided that a different test setup would be needed to achieve the first test objective.

Given the lack of time to make modifications to the setup, the best option was to place the test bed and tank inside the chamber. So, the test bed and propellant storage were placed onto the single scale inside of the chamber. Since no issues had been found with the external pressurant supply during the first series of tests, this part of the setup was kept. This new setup is shown in fig. 6.6.

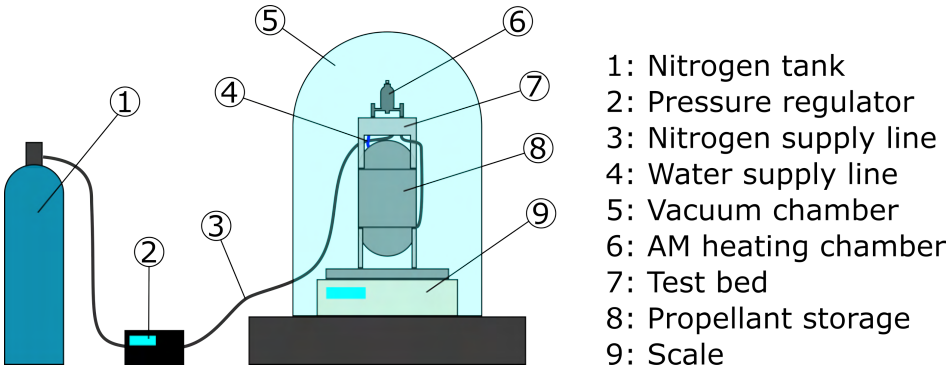

Figure 6.6: Schematic of second single scale test setup

In this configuration, the setup does not allow for continuous thrust and mass flow rate measurements. So, very long duration thrusts, where the impact of the transient startup phase on the average thrust and mass flow rate measurements can be minimized, are the only option to measure these parameters at steady state. This partly compromises the second test objective, however, the continuous temperature measurements should still make it possible to validate the temperature distribution generated by the simulation.

The test equipment available for this test campaign allowed for up to seven thermocouples to be used simultaneously. Additionally to the heater and nozzle thermocouples, it was decided to also place two probe thermocouples at the transition from the second to the third layer, as according to the numerical model this is a point where boiling is likely to occur. Furthermore, a thermocouple was also attached to the outer wall of the chamber and another to one of the mounting points of the chamber to get the temperature at the mounting interface / inlet. Finally, the last thermocouple was placed on the aluminium plate onto which the chamber is mounted. This was mainly done as a safety precaution, so the tests could be aborted if too much heat was being conducted to the rest of the test bed and risked damaging it. The thermocouple placement is schematically illustrated by fig. 6.7, while fig. 6.8a and fig. 6.8b are pictures of the test setup, showing the nozzle and outer layer thermocouple locations.

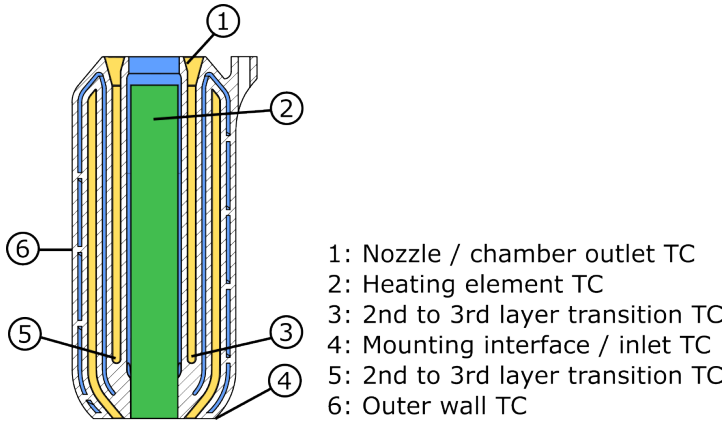

Figure 6.7: Schematic representation of thermocouple (TC) positions

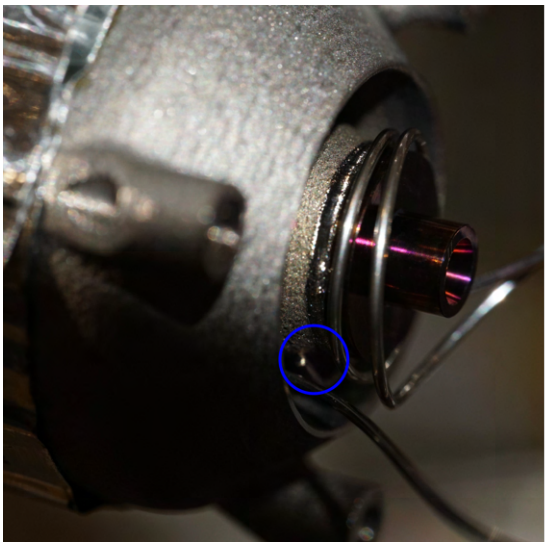

(a) Probe thermocouple wound around nozzle base with tip (circled in blue) applied against chamber outlet wall

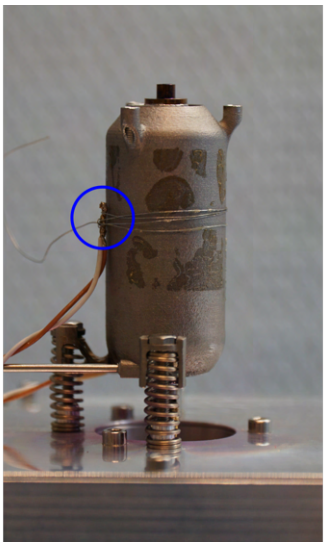

(b) Outer layer thermocouple (circled in blue), dark patches are due to glue residue from aluminium tape used to secure thermocouple in place during tests

Figure 6.8: Location of thermocouples on prototype chamber during testing

Most of the test setup equipment has already been mentioned while explaining the test setup itself. In terms of data acquisition tools, two separate systems were used in parallel. The power consumption of the heater and its temperature, as well as data from an integrated pressure transducer are all directly recorded by a data acquisition unit integrated into the test bed. This data is then sent via serial communication to one of the test computers where it is saved. The second data acquisition system records measurements from the other thermocouples, from the scale and from the pressure sensor of the vacuum chamber. The list of equipment and sensors used is given in table 6.4.

Table 6.4: List of equipment used for testing of the AM heating chamber prototype

Equipment	Model/type	Accuracy
Thermocouples	Type 'K' Nickel Chromium/Nickel Aluminium to ANSI MC96.1	Greater of 2.2 $[°C]$ or 0.75 [%]
Scale	A&D Weighing FX-3000i Precision Balance	Readability: 0.01 $[g]$; Repeatability: 0.01 $[g]$; Linearity: 0.02 $[g]$
Pressure regulator	PCD-Series PSIG Pressure Controller	0.05 $[bar]$ (+/- 25 [%] of full scale)
Data logger	34970A Data Acquisition/Switch Unit	
Vacuum pressure sensor	INFICON VGC401	Gain error: 0.02 [%], Offset error 0.05 [%] of full scale range
Power supply	9202B Multi-Range Programmable DC Power Supply	
Vacuum chamber	Kurt J.Lesker Company Glass Bell Jar Vacuum Chamber	
Vaccum pump 1	Pfeiffer ACP 15	
Vacuum pump 2	Pfeiffer TMU 261 P X	
Voltmeter	Test bed embedded electronics	
Ammeter	Test bed embedded electronics	

Once the setup is ready to be used, meaning it is fully assembled, the tank is filled with water and the fluidic lines are all connected, the test procedure is quite simple and can be summarized as follows:

1. Seal vacuum chamber and remove air until reaching vacuum level ($\leq 1 \times 10^{-4}$ mbar)
2. Start low frequency data acquisition of both acquisition systems (5 Hz)
3. Let test software perform necessary checks (propellant supply pressure, heater responsiveness, etc.)
4. Perform bake-out of test unit
5. Preheat heating chamber
6. Start higher frequency data acquisition (1 Hz)
7. Perform test
8. Switch back to lower frequency data acquisition
9. Let test unit cool down
10. Repeat from step (5) for following tests

Following the tests, the data needs to be post processed to obtain usable results. Since the data is being recorded by two separate acquisition systems, which both take measurements at slightly different time points and intervals, the first post processing step is to interpolate the data recorded by the test bed to obtain data points at the same time points as the ones recorded by the external data acquisition system.

Next, the start and end points of the thrusts have to be identified. The start of a thrust can be identified by a jump in force measured by the scale coupled with a rise in the vacuum chamber pressure, as steam is expelled by the thruster. Once a start point has been identified, the end point can simply be found from the duration of the thrust which is known.

Since a single scale was used to measure the thrust and propellant consumption, the scale data has to be processed to separate these two pieces of information. One can use the measurements taken by the scale before and after the test to obtain the total propellant consumption. To reduce the impact of noise an average of a series of measurements is taken instead of a single value. For the measurement before the test an average taken over 15 s is deemed sufficient. For the measurement after the test however, it was found that the thruster needs some time to settle down and for the scale measurement to become constant again. It was thus decided to average this measurement over 120 s. So, with these measurements giving the propellant consumption, the average mass flow rate can be obtained by dividing the consumption by the test duration, as shown in eq. (6.1), where $M_{initial}$ and M_{final} are the initial and final mass measurements and t the thrust duration.

$$\dot{m}_{avg} = \frac{M_{initial} - M_{final}}{t} \tag{6.1}$$

To obtain the thrust from the scale data, a constant mass flow rate over the duration of the thrust is assumed. One can then subtract the initial averaged scale measurement from the measured values, $M_{measured}$, and compensate the mass reduction resulting from the consumption of propellant by adding the product of the mass flow rate and time elapsed since the start of the thrust, t, see eq. (6.2). However, as the chamber outlet temperature is bound to change during the tests, the mass flow rate will also change. Thus, the thrust obtained with this post processing will not be the real thrust produced by the resistojet. So one should only consider the initial thrust measured during the first seconds as accurate, while the later values should be considered as estimates.

$$T(t) = 9.81(M_{measured}(t) - M_{initial} + \dot{m}_{avg} \cdot t) \tag{6.2}$$

The last post processing step that remains is the averaging of the measurements taken by the two thermocouples located at the transition from the second to the third layer. The other parameters do not require any post processing meaning that all of the measurements can be plotted and the results evaluated.

6.2.3. Test results

In this section the test results are presented. In total eight tests were performed with the second test setup, six successful ones and two incomplete tests. The results are presented under the form of time plots of the different parameters that were monitored. These parameters include the nozzle, second to third layer transition, outer wall and mounting interface temperatures shown in fig. 6.9 and fig. 6.11. The heater temperature, compensated thrust, input power and vacuum chamber pressure are shown in fig. 6.10 and fig. 6.12.

The first two tests were performed with the following parameters. Preheat time was set to 15 minutes at 750 °C, the tank pressure to 3.75 bar and the thrust duration to 10 minutes. The measurements taken during those tests as well as during all other successful tests are shown in fig. 6.9 and fig. 6.10. While from fig. 6.9 one can see that the second layer and inlet temperatures seem to reach a plateau, the heater and nozzle temperatures were decreasing after 10 minutes.

Based on these initial observations it was decided that the test duration should be increased to reach steady state. However, a safety feature in the GSE software prevented longer thrusts. Changing this limit was deemed unfeasible given the very tight schedule of the test allocated campaign. It was thus decided to perform the following thrust at a maximum duration of 13 minutes.

The next two tests were thus carried out with the same parameters as the first two ones but with the increased thrust duration. These tests were successful and are thus also shown in fig. 6.9 and fig. 6.10. From these slightly longer tests it became apparent that the heater and nozzle temperatures were not about to stabilize. Thus, with further increasing the test duration not being an option, a different solution was needed to reach steady state. First, reducing the target temperature to 700 °C for the preheat and test was considered. However, during the first test with a lower set temperature, the temperature of the heater dropped below 600 °C, triggering a safety and aborting the test, see fig. 6.11 and fig. 6.12. The purpose of this safety feature is to prevent operation at too low temperatures, where the exhaust could start freeze and potentially damage the test equipment. However, following the abort command, the power supply was immediately cut, which resulted in a rapid temperature drop and the likely formation of ice (not observed), as indicated by the thrust spike in fig. 6.12.

Following this failure, the initial conclusion was that the AM chamber is not able to maintain its heater temperature above 600 °C at steady state with the 38 W of maximum power. To reach steady state operating conditions that allow for a higher steady state temperature at a lower power were needed. From the sensitivity analysis performed on the numerical model, see section 5.4.3, one can see that reducing the mass flow rate can achieve this effect. It was thus decided to reduce the operating pressure from 3.75 to 3.00 bar and raise the target temperature back to 750 °C. The first test with these settings unfortunately failed as well. Indeed, the heater did not reach its target temperature during the preheat phase and as soon as it started thrusting, the temperature started dropping. This time ice formation was observed at the nozzle outlet. Looking at fig. 6.12, one can see that the heater power seems to be capped to around 10 W, which is the reason why the heater could not reach the desired temperature.

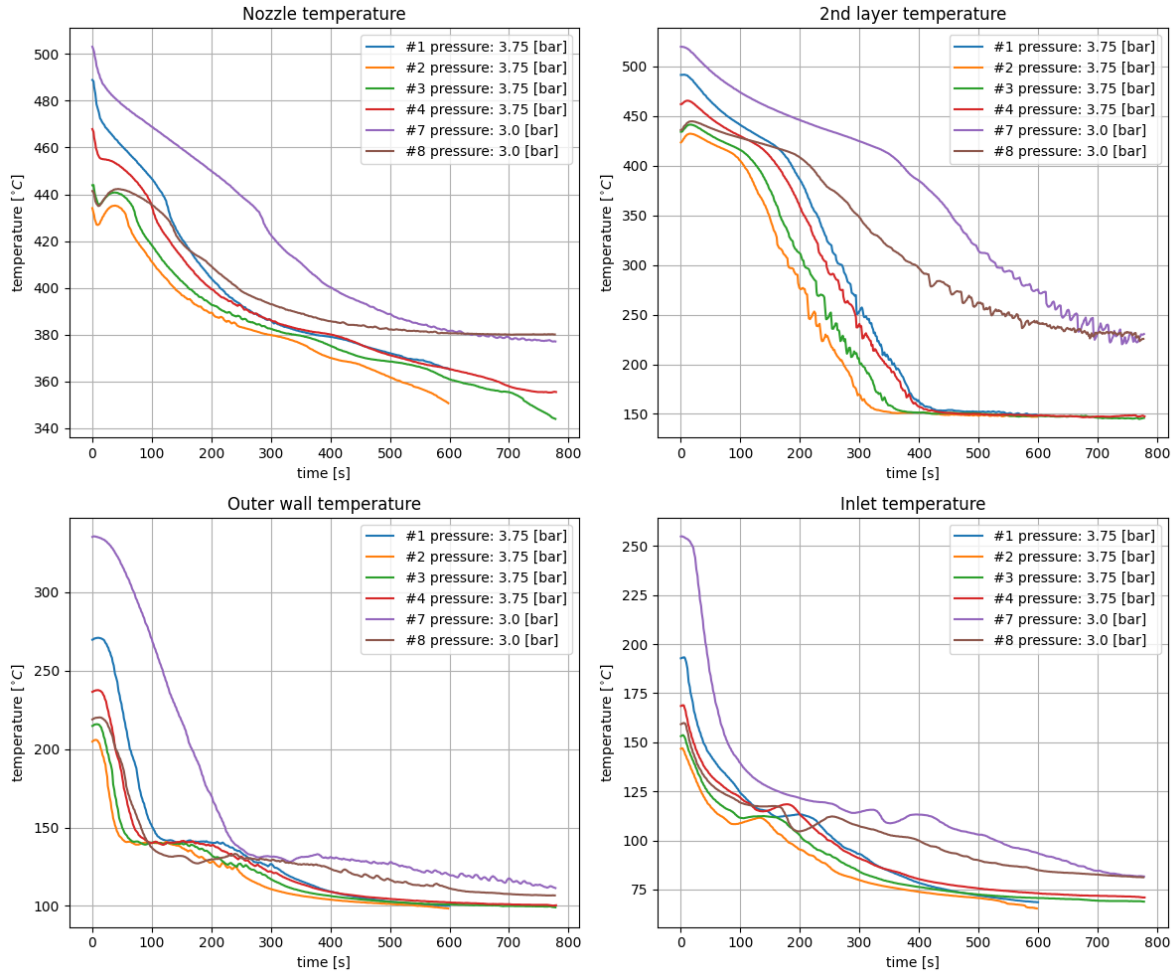

Figure 6.9: Temperatures measured on the AM heating chamber at multiple locations during the six successful tests

The cause for this power limit is not entirely clear, but it seems that an incorrect recovery from the previous failure might have caused it.

Indeed, after reinitialising the system, two further tests could be performed at 3.00 bar. These successful tests are shown in fig. 6.9 and fig. 6.10. The results of those tests show that all of the temperatures, as well as the power consumption seem to be stabilising. The fact that the power consumption is stabilising at around 32 W means that with these operating conditions it is likely possible to achieve steady state. This would however require longer tests. Due to time constraints and the project coming to an end, no more tests could be carried out, meaning that no test data could be gathered at steady state operation.

The tests described in this section are summarized in table 6.5. The main parameters of the operating conditions are included in this table as well as the average performance of the successful tests. A more detailed analysis of the test results and possible conclusions are presented in section 6.2.4.

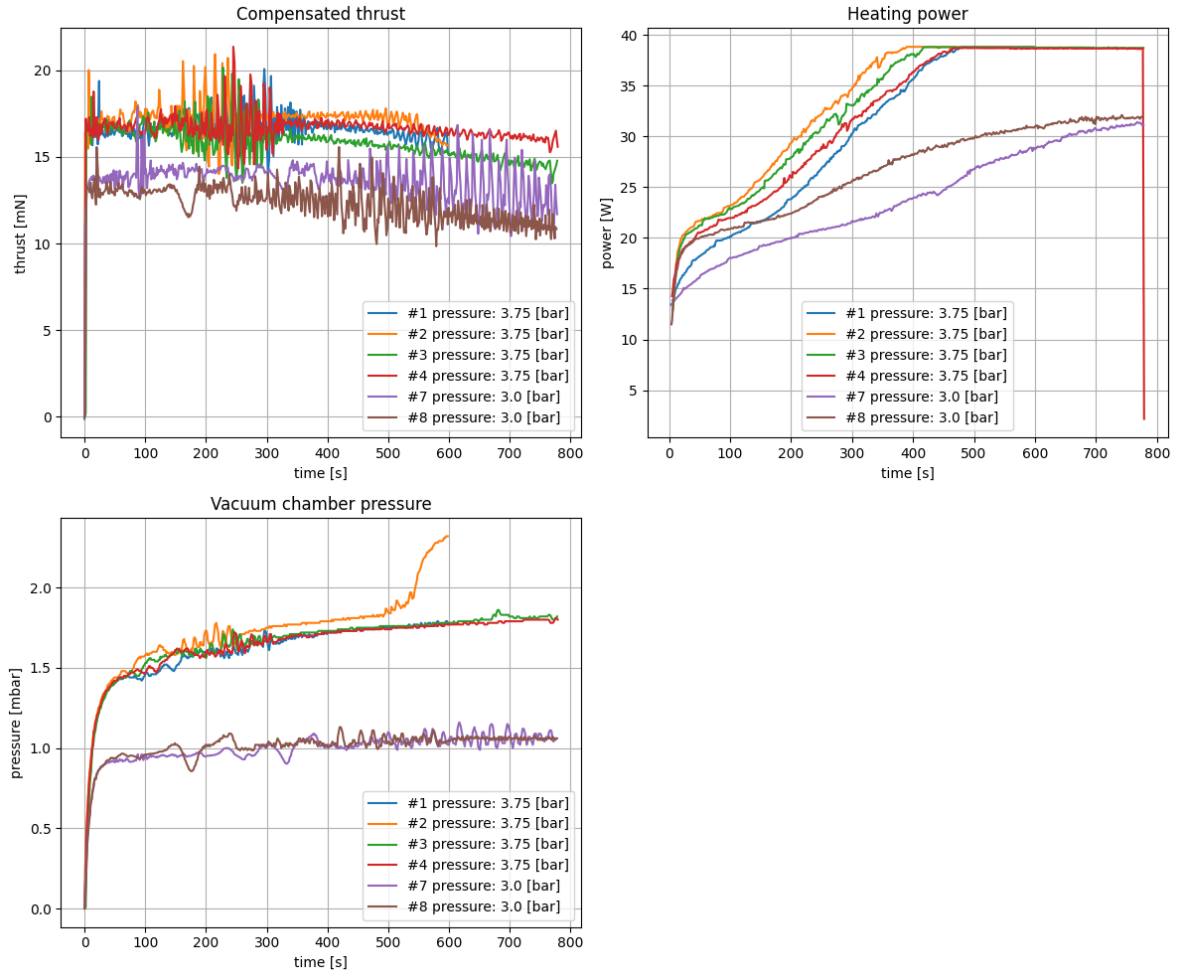

Figure 6.10: Thrust estimate, heater power and vacuum chamber pressure measurements taken during the six successful tests

6.2.4. Discussion

While the previous section, presenting the results, also contained some brief analysis of certain results and preliminary conclusions used to guide the tests towards achieving the test objectives, the main analysis and discussion of the results is presented in this section. This discussion will mainly focus on the six successful tests.

The first and probably most important conclusion one can draw from the tests is that the propulsion system is capable of producing thrust with its new AM heating chamber. Indeed as shown by the thrust plot in fig. 6.10, right after the start of the tests, the force measured by the scale jumps up by 17 mN for the 3.75 bar tests and by 13.5 mN for the 3.00 bar ones. The fact that this force is indeed the thrust generated by the setup is further confirmed by the increase in pressure within the vacuum chamber, indicating that gas is being released into the chamber. Furthermore, the reduction in temperature throughout the chamber shown in fig. 6.9 also confirms that heat is being transferred from the internal heater and heating chamber to the propellant. One can thus conclude that the first test objective has been fulfilled and the functionality of the AM heating chamber has been demonstrated.

Regarding the second test objective, one of the main conditions to have usable data for verification is that the setup should reach steady state during the test runs. By looking at the temperature plots in fig. 6.9, one can see that for the 3.75 bar tests, thermal steady state is not reached, as some of the temperatures are still dropping at the end of the runs. For the tests at the lower 3.00 bar pressure, it is a bit less clear. The temperatures seem to be leveling off, but only just, so one cannot conclusively say that steady state has been achieved. Thus, one can conclude that the second test objective has not been achieved. To support this conclusion, a more detailed analysis of the behaviour of the chamber temperatures is warranted. This analysis should also provide further insights into the behaviour of this

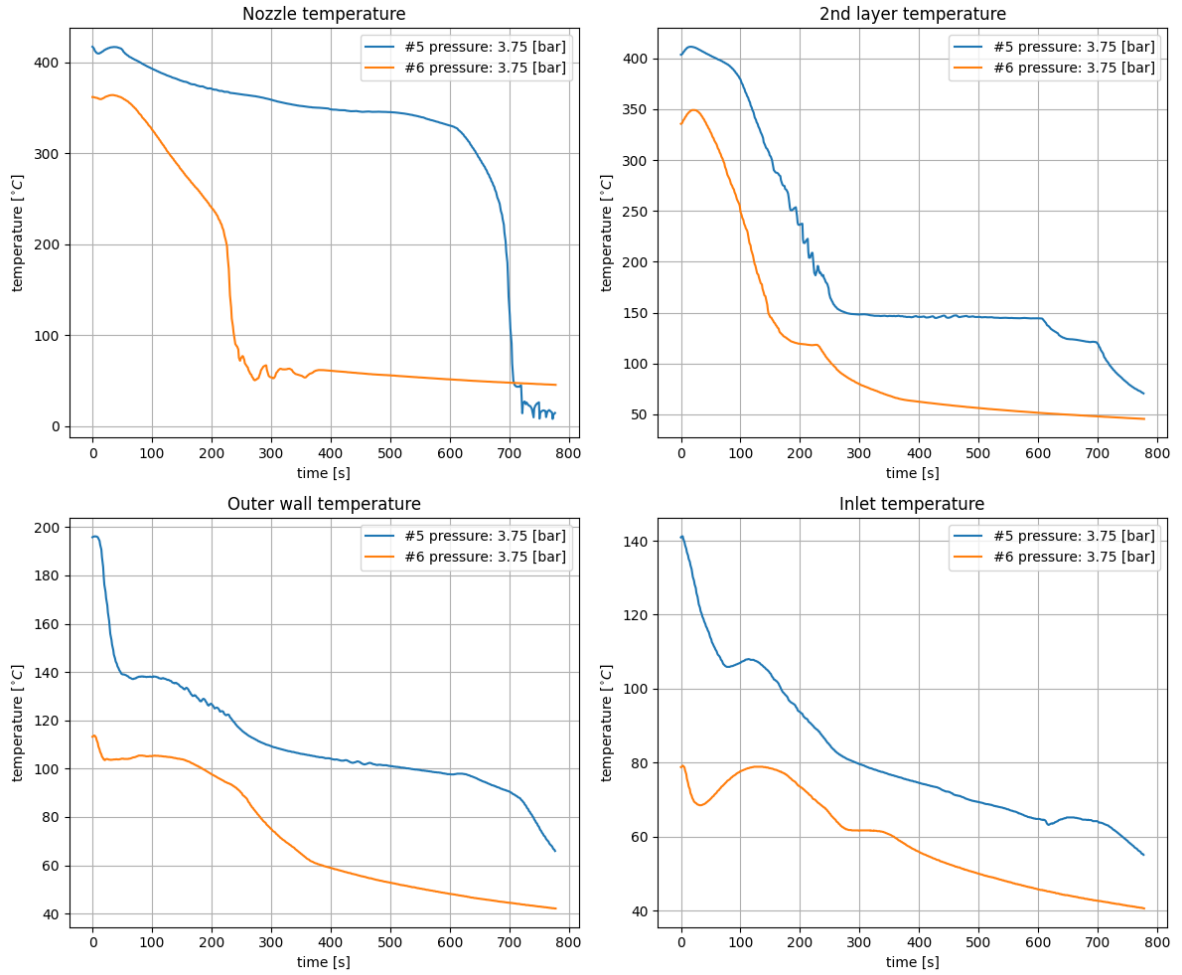

Figure 6.11: Temperatures measured on the AM heating chamber at multiple locations during the two unsuccessful tests

setup and its AM chamber and show why one can say that certain tests were close to achieving steady state or not.

Starting this analysis with the first four tests at a pressure of 3.75 bar, one can see that in all four tests the cartridge heater was able to reach its target temperature of 750 °C, see fig. 6.10, however, the temperature measured at the wall near the nozzle, see fig. 6.9, only reaches a value of 434 to 489 °C. So, one can already conclude from this that while they are in close proximity, the measurements in the heater and at the nozzle are not comparable before propellant starts flowing. Furthermore, the inconsistency of the nozzle temperature should also be noted. The main reason for this inconsistency is likely to be the fact that the preheat phase was not always started with the same initial conditions. Indeed, for the first test, the preheat phase came right after the bake-out phase during which a substantial amount of heat had already been transferred to the test bed and AM chamber assembly. For later tests, the cooldown time between tests was not kept constant, meaning that the setup had still variable amounts of heat stored within its structure before the next preheat phase. While these differences in starting conditions are not ideal, one can see from the temperature plots that the differences quickly reduce over the course of the tests, meaning that if longer tests could be performed the start conditions would play a negligible impact.

Back to the observation about the discrepancy between the nozzle temperature and heater temperature, one can see that the difference observed at the start of the test runs remains throughout their entire duration. So, even with propellant flowing through the chamber. One of the simplifying assumptions used in the numerical model was that the temperature on the inner and outer wall of a channel are the same for a given axial position. According to this, one should not see the large temperature difference between the heater and nozzle found here. However, while it is clear that this assumption

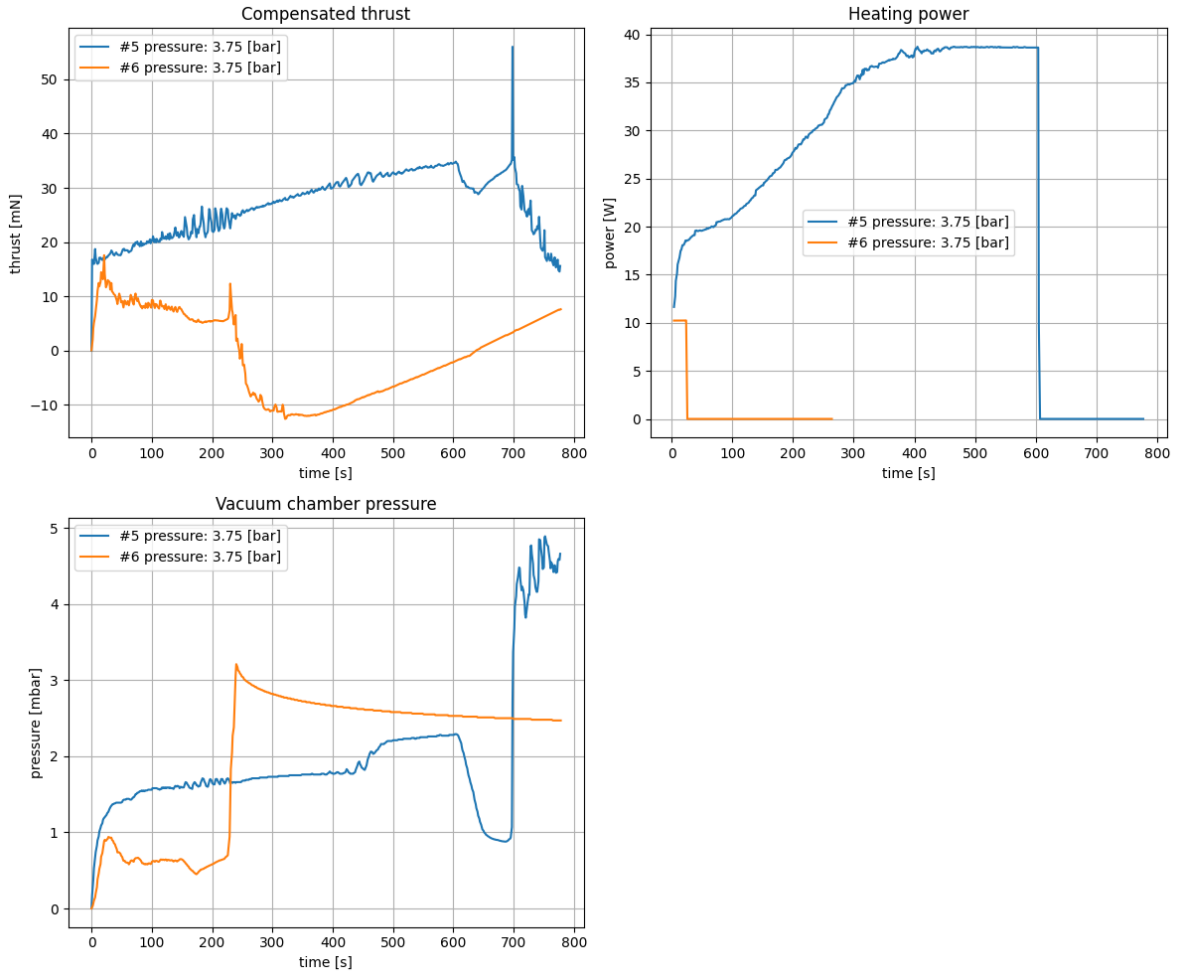

Figure 6.12: Thrust estimate, heater power and vacuum chamber pressure measurements taken during the two unsuccessful tests

is not applicable near the nozzle, it might still be true at most other locations on the chamber. Indeed, the nozzle is a region that is subject to different phenomenons than other areas. It could be possible that the expanding steam cools the nozzle down and helps create this large temperature difference. This hypothesis is reinforced when considering that ice formed on the nozzle during both of the aborted tests. Furthermore, the nozzle, which was initially shiny and metallic gray turned dark blue/purple after the tests with the first test setup. This darker color could have helped the nozzle dissipate more heat through radiation, further exacerbating the temperature difference. Finally, it is also plausible that the thermocouple near the nozzle, simply slightly pressed against the chamber wall was not providing an accurate reading.

Still on the topic of temperatures for the first four tests, it is interesting to note that the outer wall temperature drops rapidly at the start of the tests, before reaching a brief plateau slightly below 140 °C and then further dropping to seemingly stabilize at around 100 °C. Similarly, the second to third layer transition temperature also reaches a plateau at 150 °C for the second half of the test runs. Incidentally, the boiling temperature of water at 3.75 bar is 140 °C. Thus one can conclude that during the first thrusting phase, the water boils very early in the first layer, before the boiling point quickly moves up in that layer, coinciding with the plateau at 140 °C. Later in the test, the section in which boiling occurs moves further downstream in the channels and covers the section including the transition from the second to third layers. So the fact that the temperature stays very constant for the latter half of the test at that location is not necessarily an indication that steady state has been reached. Indeed, anywhere within the section where boiling occurs, the chamber should be at or close to the boiling temperature. So, at around 400 s into the tests, the start of the third layer might correspond with the end of the phase

Table 6.5: Summary of the main test conditions and results

Test ID	Status	Duration $[s]$	Tank pressure $[bar]$	Target temperature $[°C]$	Average thrust $[mN]$	Average mass flow rate $[mg/s]$	Average ISP $[s]$	Notes
1	success	10	3.75	750	16.65	11.69	145.2	
2	success	10	3.75	750	17.29	12.3	143.4	
3	success	13	3.75	750	16.42	11.73	142.7	
4	success	13	3.75	750	16.34	11.58	143.9	
5	failure	13	3.75	700	/	/	/	Cartridge temperature went below 600 $[°C]$ and low temperature abort was triggered
6	failure	13	3.00	750	/	/	/	Preheat failure due to power being limited to 10 $[W]$ for unknown reason
7	success	13	3.00	750	14.94	9.15	166.4	
8	success	13	3.00	750	12.33	8.87	141.8	

transition region, while at the end of the test, this point could correspond to the middle or even the start of the transition region. This hypothesis is further reinforced by the fact that the nozzle temperature keeps on dropping all the way until the end of the test.

All of these factors seem to confirm that for the 3.75 bar cases, the thruster has not reached steady state and will not be able to reach steady state without the temperature of the heater dropping below 600 °C, as highlighted by the fifth test. Moving on to the cases at 3.00 bar, one can once again note the large difference in initial temperatures throughout the chamber. The higher temperatures of the seventh test can be explained by the fact that, following the failure of the sixth test, a bake-out at 750 °C was performed to ensure that the heater was again capable of reaching its target temperature. Following the bake-out, the setup went straight into preheat mode, followed by the thrust. It thus had significantly more stored heat at the start of the test.

As for the other tests, this initial difference gradually reduces and the end temperatures are quite similar. What is quite different for the tests at a lower pressure is that the heater temperature stays at 750 °C throughout the tests. Indeed, the power input plot shows that, while the power is rising throughout the test, to make up for the consumption of the stored thermal energy, towards the end of the test run, the power seems to level off at around 32 W. This is particularly visible for the eighth run, because it started with less stored energy and thus closer to steady state. Looking at the other temperature curves, one can make similar observations. The temperatures seem to level off towards the end of the run, especially for the eighth test. Thus, if tests with the same operating conditions could be extended to 15 or 20 minutes or if the preheat time could be shortened, one might be able to achieve thermal steady state.

Furthermore, it is also worth noting that at a lower pressure, the temperatures throughout the chamber remain higher. This confirms the predictions of the numerical model that a lower mass flow rate allows for operation at a lower power and higher temperature. The fact that the mass flow rate is lower is confirmed by measurements, but also by the vacuum chamber pressure readings, that stay lower than for the higher pressure tests. Interestingly, the plateaus near the boiling temperature of water observed at 3.75 bar cannot be found on the plots of the tests at 3.00 bar, where they should occur at 133.5 °C. It thus seems that the water is boiling somewhere between the middle of the outer channel and the end of the second channel.

Going back to the thrust plot, a further observation is the fluctuations in the measurements. However,

the amplitude of these fluctuations is not constant throughout the tests. Indeed, for the runs at 3.75 bar, the oscillations are mainly strong from the start until a bit over 300 s into the tests. For the 3.00 bar thrusts, the oscillations are quite small at first but start to become more pronounced at the 300 to 400 s mark. The most likely explanation for these oscillations is an instability in the boiling process and the location where it occurs. The earlier tests with the first setup configuration already revealed this effect of the heating chamber. One can imagine that the phase transition of water removes a lot of energy locally and thus cools down the wall surface at the location where boiling occurs. This allows the boiling location to move further downstream where the walls are still hotter. If the heat stored deeper in the chamber walls heats the surface of those walls back up, the resulting temperature increase upstream of the boiling point can cause it to move back upstream, restarting the cycle and creating thrust and mass flow rate oscillations. In this context, it is also worth noting that for the 3.75 bar tests, the reduction in oscillations almost coincides with the temperature at the end of the second layer reaching its plateau. Thus the thrust and mass flow rate oscillation might be predominant at certain operating conditions or cooldown rates of the prototype chamber. Gaining a better understanding of the thruster behaviour might help identify the conditions at which oscillations could be minimised.

While for the 3.75 bar cases, the thrust magnitude is very similar for all tests, for the 3.00 bar tests, the thrust starts out with the same magnitude, but diverges between the two tests. In fact, for the seventh test, at the end of the run the thrust magnitude is more comparable to that of the tests at higher pressure than to that of the other test at the same conditions. One possible explanation for this is the difference in starting conditions due to preheating. Furthermore, while the plot in fig. 6.10 shows that it is the thrust that is higher, it might in fact be the mass flow rate that has not remained constant. Indeed, with this setup it was not possible to differentiate between the mass flow rate and thrust due to the use of a single scale. The higher thrust of test seven is also reflected by the higher specific impulse shown in table 6.5.

Finally, about the performance of the thruster in terms of specific impulse and thrust, one cannot make any definitive conclusions, since the values are heavily influenced by the transient phase at the start of the tests. However, the performance is in line with what would be expected for a resistojet operating under similar conditions. This concludes the analysis and discussion of the test results.

6.3. Comparison of test results to numerical model

One of the main requirements for the test results to be usable in a comparison with the numerical model was that thermal steady state is reached. In the last two test runs it is plausible that towards the end of the runs the chamber was close to steady state. One might thus be tempted to reproduce the operating conditions of these tests in the numerical model to compare them to the test results. This was done with test #8 using the input parameters summarized in table 6.6. The simulation results are shown in fig. 6.13.

Table 6.6: Operating and boundary conditions used to replicate test #8 with the numerical model

Parameter	Value	Unit	Parameter	Value	Unit
number of channels	3	$[-]$	operating pressure	3.00	$[bar]$
channel length	41.6	$[mm]$	mass flow rate	8.87	$[mg/s]$
wall thickness	0.8	$[mm]$	inlet wall temperature	81	$[°C]$
channel width	0.5	$[mm]$	inlet fluid temperature	80	$[°C]$
layer spacing	1.2	$[mm]$	ambient temperature	293	$[K]$
heated section length	34.7	$[mm]$	emissivity	0.8	$[-]$
input power	32	$[W]$	wall conductivity	11.34	$[W/(m \cdot K)]$

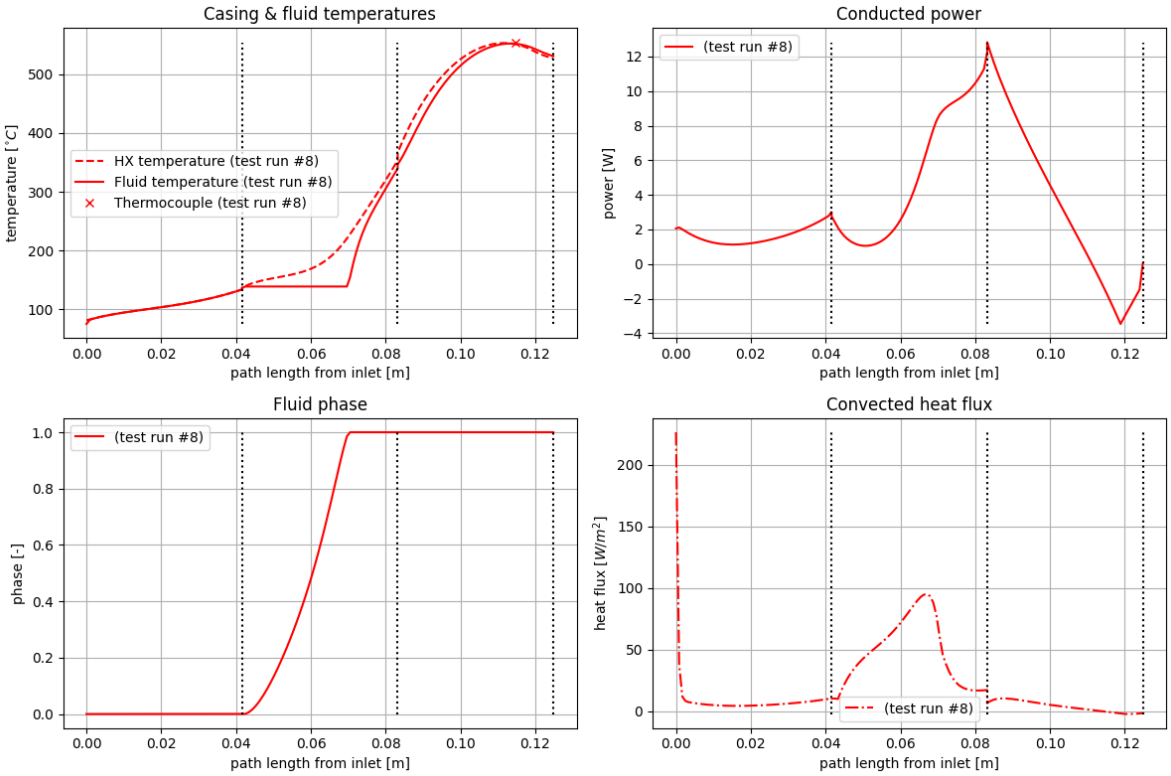

Figure 6.13: Simulation results of the attempt to replicate the condition of test #8 with the numerical model

From the temperature plot of the simulation, one can see that at steady state, the chamber should reach 105 °C at the outer wall, 353 °C at the end of the second layer and 527 °C at the nozzle. From the test result plots, shown in fig. 6.9, one can however see that the chamber reaches 107 °C at the outer wall, 230 °C at the end of the second layer and 380 °C at the nozzle towards the end of the run. So, except for the outer wall temperature, the simulation and test results do not match at all. Based on this, one might be tempted to prematurely conclude that the simulation is incorrect. However, if one remembers the sensitivity analysis in section 5.4.3, one should know that the mass flow rate can have a large impact on the simulation outcome. Furthermore, the mass flow rate used as an input value for the simulation presented here was set equal to the average mass flow rate throughout the entire duration of the test. Since the temperature in the chamber continuously decreased during the test, this average mass flow rate is likely significantly lower than the real mass flow rate at the end of the test, when the temperature is at its lowest. Thus it should come as no surprise that the numerical model predicted significantly higher temperatures.

The conclusion from this comparison is that with the current test setup it is impossible to generate data that represents steady state and that would be comparable to simulations. To obtain this data, a setup that can independently and continuously measure the mass flow rate and thrust is needed. This could be achieved by using a flow meter and thrust balance. This equipment was, however, not available at the time the tests were carried out.

6.4. Conclusion

This chapter on the evaluation and testing of the AM heating chamber prototype started out with an inspection of the 3D printed part. From the inspection it was concluded that the part was dimensionally accurate and free of visible defects and could therefore be used for testing. After integrating the heating chamber into a test bed, testing revealed that the part was indeed functional, as the setup was able to produce thrust, thereby achieving one of the test and research objectives. The second test objective was to generate test data that could be compared to the results from the numerical model and used for validation. Due to issues with the initial test setup, it was necessary to revert to a simpler configuration with a single scale to measure both the thrust and propellant consumption. With this setup it was only

possible to obtain the average mass flow rate of an entire test. Thus, even though the chamber came close to the steady state conditions necessary for validation in two of the six successful tests, the mass flow rate could not be measured at these conditions making it impossible to replicate the conditions in a simulation. This means that the second test objective was not achieved and the numerical model left unvalidated. Improving the test setup with the aforementioned equipment could help with obtaining the necessary steady state data to validate the model.

7

Conclusion and recommendations

During the course of this thesis project, the heating chamber was identified as the component of a resistojet propulsion system that is the most well suited to the use of AM. A numerical model to simulate the performance of heating chambers was developed, with the intention of serving as a design tool and helping to demonstrate the performance improvements that could be unlocked through the geometrical freedom made possible by AM. A tubular concentric heating chamber, printable in a single piece, was designed and manufactured. Following an inspection, this chamber was integrated into a test bed, and a series of tests was performed. This was done with the goal of achieving the following research objective and answering the research questions established in chapter 3:

"To demonstrate the feasibility of using additively manufactured components as part of a resistojet propulsion system and demonstrate the resulting advantages, by designing, manufacturing and testing additively manufactured components for a resistojet propulsion system."

1) Can the key components of a resistojet propulsion system be manufactured with additive manufacturing technologies?

1.2) Can the heating chamber be manufactured with additive manufacturing technologies?
- 1.2.1) Can the 3D printed heating chamber be integrated into a complete propulsion system?
- 1.2.2) Can the 3D printed heating chamber be used as part of a propulsion system to produce thrust?

2) Can additive manufacturing of the key components of a resistojet propulsion system be beneficial to the system design and performance?

2.1) Can 3D printing of the heating chamber lead to a thermal efficiency increase?

The first part of this objective was accomplished with the successful demonstration of the functionality of the prototype heating chamber. Thus also positively answering the first set of research questions. Indeed, the thruster with the AM chamber was able to produce between 12.3 and 17.3 mN of thrust during six separate tests. However, the failure of the tests to generate results at thermal steady state meant that no empirical results could be compared to the predictions of the numerical model for validation. As a consequence, the unvalidated model could not be used to explore the performance potential of AM resistojet heating chambers. This means that the second part of the research objective could not be accomplished leaving the second set of research questions unanswered.

Since one can conclude that it is possible to 3D print a resistojet heating chamber. This opens the door for future resistojet designs to consider AM as a viable fabrication option. While more work is still needed to demonstrate that it is advantageous to use AM from a performance point of view, the prototype developed in this project has already shown that it is possible to use AM to go from a chamber made out of an assembly of parts to one made out of a single part even incorporating mounting points.

Given that this study only achieved part of its research objective, the main recommendation that can be made is to perform the necessary experimental testing required to validate the numerical model and use this model to investigate the performance potential of AM tubular concentric heating chambers. This could be achieved in future tests if a flow meter and thrust balance capable of taking measurements at a moderate-to-high frequency over the entire duration of the tests are used. Furthermore, to ensure that thermal steady state is reached, longer duration tests would have to be carried out.

Following the validation of the numerical model, it should be used to generate a new optimized design, tailored to fulfill a set of performance requirements specified to demonstrate the advantages of AM. Manufacturing and testing of this optimized design would then help provide a conclusive answer to the research objective defined for this project.

Going beyond the scope of this project, one could also recommend to perform endurance testing of AM heating chambers used by water resistojets. Indeed, Robinson et al.[22] have shown that a design that works for short test campaigns may faile during prolonged endurance testing and repeated heat cycles. This could be particularly relevant in the context of water resistojets, where the possibility of corrosion adds a further possible source of failure.

Finally, the test campaign has also revealed that water resistojets can be prone to boiling instabilities. More research in this domain would be recommended to understand why these oscillations are occurring and if they can be mitigated by operating the thruster at specific operating conditions or by the addition of design features.

References

[1] Jun Asakawa et al. “Fundamental Ground Experiment of a Water Resistojet Propulsion System: AQUARIUS Installed on a 6U CubeSat: EQUULEUS”. In: *TRANSACTIONS OF THE JAPAN SOCIETY FOR AERONAUTICAL AND SPACE SCIENCES, AEROSPACE TECHNOLOGY JAPAN* 16 (Jan. 2018), pp. 427–431. DOI: 10.2322/tastj.16.427.

[2] J. J. Beaman et al. “Additive Manufacturing Review: Early Past to Current Practice”. In: *Journal of Manufacturing Science and Engineering* 142.11 (Sept. 2020). ISSN: 1087-1357. DOI: 10.1115/1.4048193. URL: https://doi.org/10.1115/1.4048193 (visited on 05/18/2022).

[3] Tomasz Blachowicz, Guido Ehrmann, and Andrea Ehrmann. “Metal Additive Manufacturing for Satellites and Rockets”. In: *Applied Sciences* 11 (Dec. 2021), p. 12036. DOI: 10.3390/app112412036.

[4] Byron Blakey-Milner et al. “Metal additive manufacturing in aerospace: A review”. In: *Materials & Design* 209 (July 2021), p. 110008. DOI: 10.1016/j.matdes.2021.110008.

[5] A. Cervone. *AE4S07 – Course reader: Micro-Propulsion*. July 2020.

[6] Angelo Cervone et al. “Chapter 5 - Electrothermal microthruster”. en. In: ed. by Kean How Cheah. Elsevier, Jan. 2022, pp. 125–149. ISBN: 9780128190371. DOI: 10.1016/B978-0-12-819037-1.00003-7. (Visited on 11/08/2022).

[7] Paschalis Charalampous, Ioannis Kostavelis, and Dimitrios Tzovaras. “Non-destructive quality control methods in additive manufacturing: a survey”. In: *Rapid Prototyping Journal* 26.4 (Jan. 2020), pp. 777–790. ISSN: 1355-2546. DOI: 10.1108/RPJ-08-2019-0224. URL: https://doi.org/10.1108/RPJ-08-2019-0224 (visited on 06/30/2022).

[8] Ze Chen et al. “A review on qualification and certification for metal additive manufacturing”. In: *Virtual and Physical Prototyping* 17.2 (Apr. 2022), pp. 382–405. ISSN: 1745-2759. DOI: 10.1080/17452759.2021.2018938. URL: https://doi.org/10.1080/17452759.2021.2018938 (visited on 06/22/2022).

[9] Zhong Yang Chua, Il Hyuk Ahn, and Seung Ki Moon. “Process monitoring and inspection systems in metal additive manufacturing: Status and applications”. en. In: *International Journal of Precision Engineering and Manufacturing-Green Technology* 4.2 (Apr. 2017), pp. 235–245. ISSN: 2198-0810. DOI: 10.1007/s40684-017-0029-7. URL: https://doi.org/10.1007/s40684-017-0029-7 (visited on 06/30/2022).

[10] Giulio Coral et al. “Design and testing of additively manufactured high-efficiency resistojet on hydrogen propellant”. In: *Acta Astronautica* 181 (2021), pp. 14–27. DOI: https://doi.org/10.1016/j.actaastro.2020.12.047.

[11] T. DebRoy et al. “Additive manufacturing of metallic components – Process, structure and properties”. In: *Progress in Materials Science* 92 (Mar. 2018), pp. 112–224. DOI: 10.1016/j.pmatsci.2017.10.001.

[12] Jacob N. Easley et al. “Additive Manufacturing of Propellant Tank and Structural Supports of CubeSat Cold Gas Propulsion System”. In: *AIAA Propulsion and Energy 2019 Forum*. American Institute of Aeronautics and Astronautics, Aug. 2019. DOI: 10.2514/6.2019-4309.

[13] C. Halbach, R. Page, and R. Short. “3 kw concentric tubular resistojet performance compared with theory”. In: *5th Electric Propulsion Conference*. American Institute of Aeronautics and Astronautics, Mar. 1966. DOI: 10.2514/6.1966-224.

[14] M. L. Huber et al. “New International Formulation for the Thermal Conductivity of H_2O”. In: 41.3 (2012), p. 033102. DOI: 10.1063/1.4738955.

[15] Frank P. Incropera. *Fundamentals of heat transfer*. eng. New York : Wiley, 1981. ISBN: 9780471427117. URL: http://archive.org/details/fundamentalsofhe0000incr (visited on 11/09/2022).

[16] Aljaž Ivekovič et al. “Selective laser melting of tungsten and tungsten alloys”. In: *International Journal of Refractory Metals and Hard Materials* 72 (Dec. 2017). DOI: 10.1016/j.ijrmhm.2017.12.005.

[17] Ming Li et al. “Metal Binder Jetting Additive Manufacturing: A Literature Review”. In: *Journal of Manufacturing Science and Engineering* 142 (June 2020), pp. 1–45. DOI: 10.1115/1.4047430.

[18] Moshe Nahmany et al. “Structural Properties of EB-Welded AlSi10Mg Thin-Walled Pressure Vessels Produced by AM-SLM Technology”. en. In: *Journal of Materials Engineering and Performance* 26.10 (Oct. 2017), pp. 4813–4821. ISSN: 1544-1024. DOI: 10.1007/s11665-017-2953-7. URL: https://doi.org/10.1007/s11665-017-2953-7 (visited on 05/21/2022).

[19] Daisuke Nakata and Kiyoshi Kinefuchi. “Thermal Design and Experimental Verification of the 3D-printed Registojet”. In: *2018 Joint Propulsion Conference*. American Institute of Aeronautics and Astronautics. DOI: 10.2514/6.2018-4907. URL: https://arc.aiaa.org/doi/abs/10.2514/6.2018-4907 (visited on 05/29/2022).

[20] Daisuke Nakata et al. “Thermal Design and Experimental Verification of a Three-Dimensional-Printed Resistojet”. In: *Journal of Propulsion and Power* 38.1 (2022), pp. 148–156. DOI: 10.2514/1.B38187. URL: https://doi.org/10.2514/1.B38187 (visited on 05/12/2022).

[21] M. Robinson et al. “Endurance testing of the additively manufactured STAR resistojet”. en. In: *Materials & Design* 180 (Oct. 2019), p. 107907. ISSN: 0264-1275. DOI: 10.1016/j.matdes.2019.107907. URL: https://www.sciencedirect.com/science/article/pii/S0264127519303454 (visited on 06/10/2022).

[22] Matthew David Robinson et al. *Endurance Testing of Engineering Model Additive-Manufactured High Temperature Resistojets Made from Inconel 625 and Tantalum*. en. Tech. rep. 4091359. Rochester, NY, Apr. 2022. DOI: 10.2139/ssrn.4091359. URL: https://papers.ssrn.com/abstract=4091359 (visited on 06/10/2022).

[23] Federico Romei. “Manufacturing of a High-Temperature Resistojet Heat Exchanger by Selective Laser Melting”. In: *Acta Astronautica* 138 (May 2017), pp. 356–368. DOI: 10.1016/j.actaastro.2017.05.020.

[24] Federico Romei, Angelo Grubisic, and Dave Gibbon. “Performance testing and evaluation of a high temperature xenon resistojet prototype manufactured by selective laser melting”. In: IEPC Conference. 2017. URL: https://core.ac.uk/display/111415385.

[25] Federico Romei, Angelo Grubisic, and Matthew Robinson. “High performance resistojet thruster: STAR Status Update”. In: May 2018. URL: https://eprints.soton.ac.uk/417359/1/FRomei_High_Performance_Resistojet_Thruster_STAR_Status_Update.pdf.

[26] Geovanni A Solorzano. “Development and Prototype Validation of an Additive Manufactured Cubesat Propulsion Tank”. In: (2015). URL: https://commons.erau.edu/edt/249/.

[27] R Shankar Subramanian. “Heat transfer in flow through conduits”. In: *Department of Chemical and Biomolecular Engineering, Clarkson University Project* (2015). URL: https://web2.clarkson.edu/projects/subramanian/ch330/notes/Heat%20Transfer%20in%20Flow%20Through%20Conduits.pdf.

[28] Akshay Reddy Tummala and Atri Dutta. “An Overview of Cube Satellite Propulsion Technologies and Trends”. In: *Aerospace* (2017). DOI: 10.3390/aerospace4040058.

[29] W. Wagner and A. Pruss. “The IAPWS Formulation 1995 for the Thermodynamic Properties of Ordinary Water Substance for General and Scientific Use”. In: 31.2 (2002), pp. 387–535. DOI: 10.1063/1.1461829.

[30] Kazuya Yaginuma et al. “AQT-D: CubeSat Demonstration of a Water Propulsion System Deployed from ISS”. In: *TRANSACTIONS OF THE JAPAN SOCIETY FOR AERONAUTICAL AND SPACE SCIENCES, AEROSPACE TECHNOLOGY JAPAN* 18.4 (June 2019), pp. 141–148. DOI: 10.2322/tastj.18.141.

[31] B.T.C. Zandbergen. *Course AE4S01: Thermal Rocket Propulsion*. Aug. 2020.

A

Heating chamber technical drawing

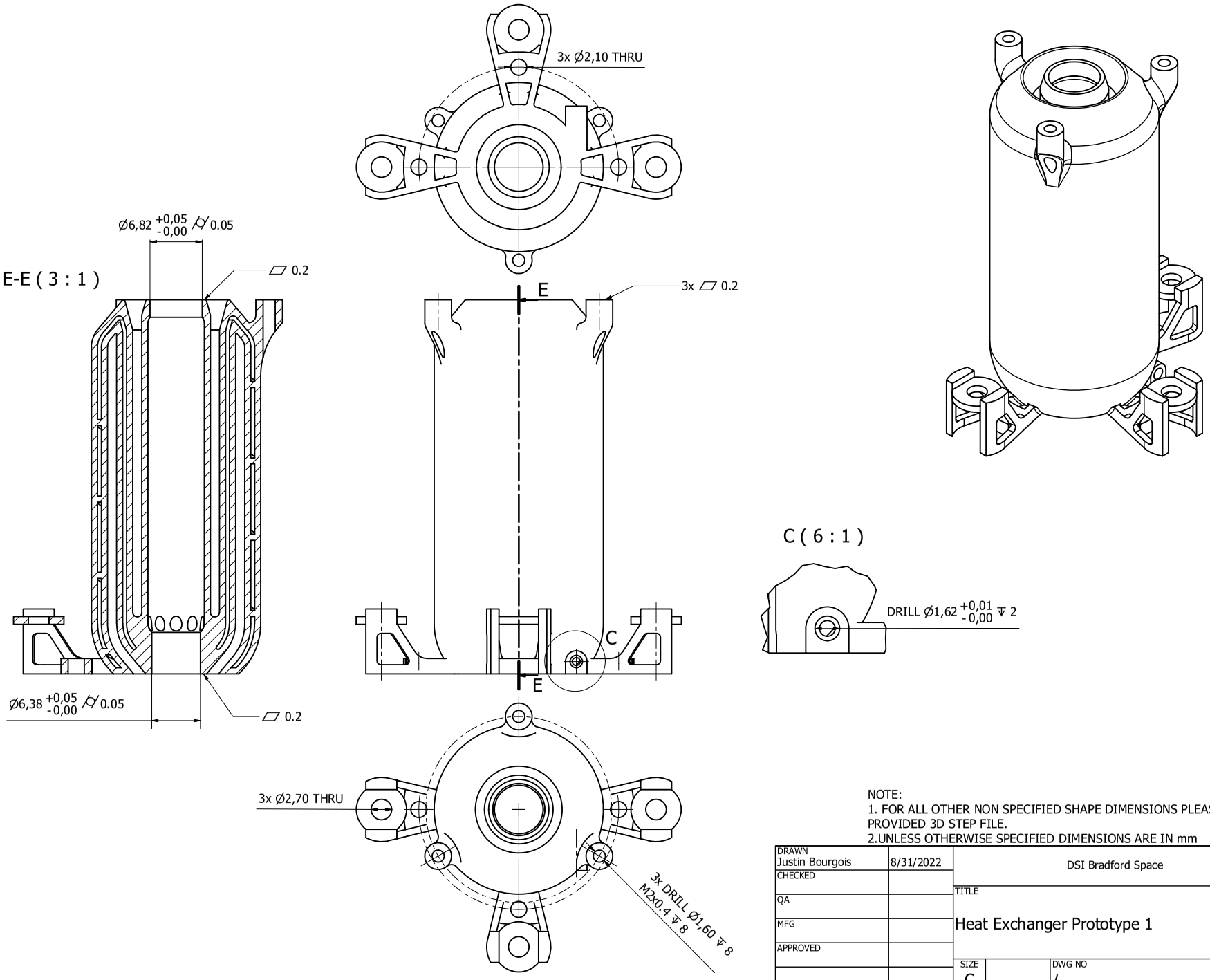

NOTE:
1. FOR ALL OTHER NON SPECIFIED SHAPE DIMENSIONS PLEASE USE THE PROVIDED 3D STEP FILE.
2.UNLESS OTHERWISE SPECIFIED DIMENSIONS ARE IN mm

DRAWN Justin Bourgois	8/31/2022	DSI Bradford Space	
CHECKED		TITLE	
QA		Heat Exchanger Prototype 1	
MFG			
APPROVED			
		SIZE C / DWG NO /	REV 1
		SCALE 3 : 1	SHEET 1 OF 1

B

Prototype close-up pictures

Figure B.1: AM heating chamber prototype before the integration of the nozzle and cartridge heater

Figure B.2: Sectioned heating heating chamber used to inspect the capability of the printing process to accurately reproduce the inner features

Figure B.3: Close up picture of the partially collapsed horizontal area at the transition from the first to the second channel

Figure B.4: Close up picture of the overhanging channel wall showing a minor print defect

Figure B.5: Close up picture showing the surface roughness of the channel walls of the as printed part

C

Numerical model script

```
1  ##script name: Resistojet HX Simulator v1.3.4
2  ##author: Justin Bourgois
3
4  ##############################    Initialisation
       ##############################
5
6  import numpy as np
7  from scipy import interpolate
8  from scipy import integrate
9  import matplotlib.pyplot as plt
10 import sys
11 import os
12 from datetime import datetime
13
14 if not sys.warnoptions:
15     import warnings
16     warnings.simplefilter('error')
17
18 time_start = datetime.now()
19
20 #initialize figure
21 fig, ax = plt.subplots(2, 2, figsize = (12, 8))
22 colors = ('r', 'b', 'y', 'c', 'g')
23 linestyles = ('--', '-.', ':', '-')
24
25
26 ##############################    Functions    ##############################
27
28
29
30 #importing NIST data from file
31 def importNISTdata(filename):
32
33 # description:  function performing the calculations to get the
       temperature and power distribution along given layer
34
35 # intputs:  #filename:  name of file (generated from NIST) from which
       reference data is to be read
36
```

```
37 # outputs:  #data:      0: Temperature (K), 1:Pressure (MPa), 2: Density (
       kg/m3), 3: Volume (m3/kg), 4: Internal Energy (kJ/kg),
38 #                       5: Enthalpy (kJ/kg), 6: Entropy (J/g*K), 7: Cv (J/
       g*K), 8: Cp (J/kg*K), 9: Sound Spd. (m/s),
39 #                       10: Joule-Thomson (K/MPa), 11: Viscosity (uPa*s),
       12: Therm. Cond. (W/m*K), 13: Phase
40
41      data = np.empty(14)
42
43      file = open(r'Reference data\\' + filename,'r')
44      lines = file.readlines()
45      file.close()
46      for i in range(1,len(lines)):
47          line = lines[i].split('\t')
48          row = np.empty(14)
49          for j in range(13):
50              element = float(line[j])
51              row[j] = element
52          if line[13] == 'liquid\n':
53              row[13] = 0
54          elif line[13] == 'vapor\n':
55              row[13] = 1
56          else:
57              row[13] = -1
58          data = np.vstack((data, row))
59
60      data[:,5] = data[:,5] * 1000
61      data[:,8] = data[:,8] * 1000
62
63      return data[1:]
64
65
66  def importMetalData(filename):
67
68      data = np.empty(2)
69
70      file = open(r'Reference data\\' + filename,'r')
71      lines = file.readlines()
72      file.close()
73      for i in range(0,len(lines)):
74          line = lines[i].split('\t')
75          row = np.empty(2)
76          for j in range(2):
77              element = float(line[j])
78              row[j] = element
79          data = np.vstack((data, row))
80
81      data = data[1:]
82
83      return data
84
85  def getTempDistr(N, local_cond, local_rad, local_conv, local_gen,
       local_int_out, local_int_in, local_standoff, local_wires, Pc_0, Tc_0,
       hfluid_0, Tcs):
86
87  # description:  function performing the calculations to get the
```

```
    temperature and power distribution along given layer
88
89  # intputs:  #N:                index of current layer
90             #local_cond:        turning on/off conduction
91             #local_rad:         turning on/off radiation to environment
92             #local_conv:        turning on/off convection to fluid
93             #local_gen:         turning on/off distributed heat generation
94             #local_int_out:     turning on/off inter-layer radiation from
                   outer layer
95             #local_int_in:      turning on/off inter-layer radiation from
                   inner layer
96             #local_standoff:    turning on/off temperature gradient at
                   inlet due to thermal stand-off
97             #local_wires:       turning on/off power loss due to cartridge
                    heater wires
98             #P_0:               Power flowing through wall at beginning of
                    layer
99             #Tc_0:              Temperature of wall at beginning of layer
100            #hfluid_0:          Fluid enthalpy at beginning of layer
101            #Tcs:               Temperature distribution used for inter
                   layer radiation calculations
102
103 # outputs:  #Pl:    distribution of power flowing through wall
104            #Qrl:   distribution of radiated heat flux
105            #Qcl:   distribution of convected heat flux
106            #Prl:   distribution of radiated power
107            #Pcl:   distribution of convected power
108            #Pirl:  distribution of internally radiated power
109            #Tcl:   distribution of casing wall temperature
110            #hfl:   distribution of fluid enthalpy
111            #T_tcl: temperature measured by thermocouple
112
113     if global_standoff and local_standoff:
114         if global_var_kc:
115             kc = kcfromT_metal(Tc_0)
116         else:
117             kc = base_kc
118         Tc_0 = max(min(Tc_0 + Pc_0 / (kc * N_standoff * standoff_dims[1] *
                standoff_dims[2]) * standoff_dims[0], 3000), 268)
                                    #computing temperature at end of element
                based on conduction
119
120     if global_wires and local_wires:
121         P_wires = (Tc_0 - Tc_inlet) * kc_wires * N_wires * np.pi *
                wire_dims[1]**2 / wire_dims[0]
                                                                  #computing
                temperature at end of element based on conduction
122     else:
123         P_wires = 0
124
125     T_tcl = 0
126     l_heated = 0
127
128     Pl = np.empty(n)
129     Qrl = np.empty(n)
130     Qcl = np.empty(n)
```

```
131     Prl = np.empty(n)
132     Pcl = np.empty(n)
133     Pirl = np.empty(n)
134     Tcl = np.empty(n)
135     hfl = np.empty(n)
136
137     for i in range(n):      #stepping along layer elements
138
139         if global_cond and local_cond:
140             if global_var_kc:
141                 kc = kcfromT_metal(Tc_0)
142             else:
143                 kc = base_kc
144             Tc_1 = max(min(Tc_0 + Pc_0 / (kc * As[len(r_1s)-Nl+N]) * dxs[
                    len(r_1s)-Nl+N], 3000), 268)
                                                          #computing
                    temperature at end of element based on conduction
145
146         else:
147             Tc_1 = Tc_0
148
149         if global_rad:
150             if local_rad:
151                 P_rad_r = epsilon * sigma * (((Tc_0+Tc_1)/2)**4 - Ta**4) *
                        np.pi * 2 * r_1s[len(r_1s)-Nl+N] * dxs[len(r_1s)-Nl+N]
                                    #computing power lost through
                    radiation to environment
152             else:
153                 P_rad_r = 0
154             if i == (n - 1) or i == 0:
155                 P_rad_a = epsilon * sigma * (Tc_1**4 - Ta**4) * np.pi * (
                        r_1s[len(r_1s)-Nl+N]**2 - r_4s[len(r_1s)-Nl+N]**2)
156             else:
157                 P_rad_a = 0
158             P_rad = P_rad_r + P_rad_a
159         else:
160             P_rad = 0
161
162         if global_conv and local_conv:
163             if global_var_Nu:
164                 vel = m_dot / (np.pi * (r_2s[len(r_1s)-Nl+N]**2 - r_3s[len
                        (r_1s)-Nl+N]**2) * rhofromEnthalpy(hfluid_0))
165                 Re = Dhs[len(r_1s)-Nl+N] * vel * rhofromEnthalpy(hfluid_0)
                        / mufromEnthalpy(hfluid_0)
166                 Pr = CpfromEnthalpy(hfluid_0) * mufromEnthalpy(hfluid_0) /
                        condfromEnthalpy(hfluid_0)
167                 Pe = Re * Pr
168                 if i > 0:
169                     DL = Dhs[len(r_1s)-Nl+N] / (dxs[len(r_1s)-Nl+N] * i)
170                     Nu = 3.66 + 0.065 * Pe * DL / (1 + 0.04 * (Pe * DL)
                            **(2/3))
171                 else:
172                     Nu = 3.66
173             else:
174                 Nu = base_Nu
175             conv_coeff = Nu * condfromEnthalpy(hfluid_0) / Dhs[len(r_1s)-
```

```
                Nl+N]

                #computing convection coefficient of element
176 ##          P_conv = conv_coeff * (np.pi * 2 * dxs[len(r_1s)-Nl+N] * (
    r_2s[len(r_1s)-Nl+N] + r_3s[len(r_1s)-Nl+N])) * (((Tc_0+Tc_1)/2) -
    TfromEnthalpy(hfluid_0))                                        #
    computing power transfered to fluid via convection
177
178             C1 = conv_coeff * (np.pi * 2 * dxs[len(r_1s)-Nl+N] * (r_2s[len
                    (r_1s)-Nl+N] + r_3s[len(r_1s)-Nl+N]))
179             C2 = C1 / (1 + C1 / (m_dot * CpfromEnthalpy(hfluid_0)))
180             Tfluid_0 = TfromEnthalpy(hfluid_0)
181
182             P_conv = C2 * (Tc_1 - Tfluid_0)
                                                        #computing power
                     transfered to fluid via convection
183
184         else:
185             P_conv = 0
186
187         if global_gen and local_gen and ls[len(r_1s)-Nl+N] - (cart_dims[0]
                + cart_dims[1]) < i * dxs[len(r_1s)-Nl+N] and l_heated <
                cart_dims[1] :
188             P_gen = -P_cart / cart_dims[1] * dxs[len(r_1s)-Nl+N-1]

                #computing power input of heater to element
189             l_heated = l_heated + dxs[len(r_1s)-Nl+N-1]
190         else:
191             P_gen = 0
192
193         if global_int and local_int_out:
194             T_ref = Tcs[(N)*n-i-1]

                #getting temnperature of adjacent outer element
195             T_local = Tcs[N*n+i]
196             r_ref = r_4s[len(r_1s)-Nl+N-1]
197             r_local = r_1s[len(r_1s)-Nl+N]
198             l_local = dxs[len(r_1s)-Nl+N]
199             A_local = np.pi * 2 * r_local * l_local
200             P_ir_out = sigma * A_local * (T_local**4 - T_ref**4) / (1/
                    epsilon + (1-epsilon) / epsilon * (r_local/r_ref))      #
                    computing power lost/gained through radiation to outer
                    adjacent layer
201         else:
202             P_ir_out = 0
203
204         if global_int and local_int_in:
205             T_ref = Tcs[(N+2)*n-i-1]

                #getting temnperature of adjacent outer element
206             T_local = Tcs[N*n+i]
207             r_ref = r_1s[len(r_1s)-Nl+N+1]
208             r_local = r_4s[len(r_1s)-Nl+N]
209             l_local = dxs[len(r_1s)-Nl+N]
210             A_local = np.pi * 2 * r_local * l_local
211             P_ir_in = sigma * A_local * (T_local**4 - T_ref**4) / (1/
```

```
                epsilon + (1-epsilon) / epsilon * (r_local/r_ref))      #
                    computing power lost/gained through radiation to inner
                    adjacent layer
212         else:
213             P_ir_in = 0
214
215         P_ir = P_ir_in + P_ir_out
                                                        #computing power lost
                /gained through radiation to adjacent layers
216
217         Pc_1 = Pc_0 + P_rad + P_conv + P_gen + P_ir + P_wires
                            #computing power at end of element based on all
                power inputs and outputs to element
218         hfluid_1 = hfluid_0 + P_conv / m_dot
                                            #computing fluid enthalpy at end
                 of element based on convected power
219
220         P_wires = 0
221
222         Pl[i] = Pc_1
                                                                    #adding
                new values to property distributions
223         Qrl[i] = P_rad / (dxs[len(r_1s)-Nl+N])
224         Qcl[i] = P_conv / (dxs[len(r_1s)-Nl+N]) * 2 * np.pi * (r_2s[len(
                r_1s)-Nl+N] + r_3s[len(r_1s)-Nl+N])
225         Prl[i] = P_rad
226         Pcl[i] = P_conv
227         Pirl[i] = P_ir
228         Tcl[i] = Tc_1
229         hfl[i] = hfluid_1
230
231         Tc_0 = Tc_1
                                                                        #
                setting start values for next element equal to end values of
                current element
232         Pc_0 = Pc_1
233         hfluid_0 = hfluid_1
234
235         if N == Nl-1 and ls[len(r_1s)-Nl+N] - TC_pos[1] - dxs[len(r_1s)-Nl
                +N] <= i * dxs[len(r_1s)-Nl+N] < ls[len(r_1s)-Nl+N] - TC_pos
                [1]:
236             if global_var_kc:
237                 kc = kcfromT_metal(Tc_0)
238             else:
239                 kc = base_kc
240             T_tcl = Tc_1 -  P_gen *  TC_pos[0] / (2 * np.pi * r_3s[len(
                    r_1s)-Nl+N] * dxs[len(r_1s)-Nl+N] * kc)
241
242
243     return Pl, Qrl, Qcl, Prl, Pcl, Pirl, Tcl, hfl, T_tcl
244
245
246 def sub_solver(P_0, Tc_0, Tcs):
247
248 # description:  solving function calling the function to get the
        temperature distribution of each layer
```

```
249 #                with the appropriate heat transmission/dissipation
        mechanisms turned on/off
250
251 # intputs:  #P_0:   Power flowing through wall at inlet / baseplate
        interface
252             #Tc_0:  Temperature of wall at inlet / baseplate interface
253             #Tcs:   Temperature distribution used for inter layer
                    radiation calculations
254
255 # outputs:  #Pls:   distribution of power flowing through wall
256             #Qrls:  distribution of radiated heat flux
257             #Qcls:  distribution of convected heat flux
258             #Prls:  distribution of radiated power
259             #Pcls:  distribution of convected power
260             #Pirls: distribution of internally radiated power
261             #Tcls:  distribution of casing wall temperature
262             #hfls:  distribution of fluid enthalpy
263             #T_tcs: temperature measured by thermocouple
264
265     if Nl > 1:
266
267         ##outer layer
268         N = 0
269         local_cond = True
270         local_rad = True
271         local_conv = True
272         local_gen = False
273         local_int_out = False
274         local_int_in = True
275         local_standoff = True
276         local_wires = False
277         Pls, Qrls, Qcls, Prls, Pcls, Pirls, Tcls, hfls, T_tcls =
              getTempDistr(N, local_cond, local_rad, local_conv, local_gen,
              local_int_out,
278                                                                  local_int_in
                                                                     ,
                                                                     local_standoff
                                                                     ,
                                                                     local_wires
                                                                     ,
                                                                     P_0
                                                                     ,
                                                                     Tc_0
                                                                     ,
                                                                     hfromT
                                                                     (
                                                                     Tf_inlet
                                                                     )
                                                                     ,
                                                                     Tcs
```

```
                                                                    )
279
280         ##intermediate layers
281         local_cond = True
282         local_rad = False
283         local_conv = True
284         local_gen = False
285         local_int_out = True
286         local_int_in = True
287         local_standoff = False
288         local_wires = False
289
290         for N in range(1,Nl-1):
291             Pl, Qrl, Qcl, Prl, Pcl, Pirl, Tcl, hfl, T_tcl = getTempDistr(N
                    , local_cond, local_rad, local_conv, local_gen,
                    local_int_out,
292                                                                 local_int_in
                                                                    ,
                                                                    local_standoff
                                                                    ,
                                                                    local_wires
                                                                    ,
                                                                    Pls
                                                                    [-1],
                                                                    Tcls
                                                                    [-1],
                                                                    hfls
                                                                    [-1],
                                                                    Tcs
                                                                    )
293             Pls = np.hstack((Pls, Pl))
294             Qrls = np.hstack((Qrls, Qrl))
295             Qcls = np.hstack((Qcls, Qcl))
296             Prls = np.hstack((Prls, Prl))
297             Pcls = np.hstack((Pcls, Pcl))
298             Pirls = np.hstack((Pirls, Pirl))
299             Tcls = np.hstack((Tcls, Tcl))
300             hfls = np.hstack((hfls, hfl))
301             T_tcls = np.hstack((T_tcls, T_tcl))
302
303         ## inner layer
304         local_cond = True
305         local_rad = False
306         local_conv = True
307         local_gen = True
308         local_int_out = True
309         local_int_in = False
310         local_standoff = False
311         local_wires = True
312
```

```
313             N = Nl-1
314             Pl, Qrl, Qcl, Prl, Pcl, Pirl, Tcl, hfl, T_tcl = getTempDistr(N,
                    local_cond, local_rad, local_conv, local_gen, local_int_out,
315                                                                 local_int_in
                                                                    ,
                                                                    local_standoff
                                                                    ,
                                                                    local_wires
                                                                    ,
                                                                    Pls
                                                                    [-1],
                                                                    Tcls
                                                                    [-1],
                                                                    hfls
                                                                    [-1],
                                                                    Tcs
                                                                    )
316             Pls = np.hstack((Pls, Pl))
317             Qrls = np.hstack((Qrls, Qrl))
318             Qcls = np.hstack((Qcls, Qcl))
319             Prls = np.hstack((Prls, Prl))
320             Pcls = np.hstack((Pcls, Pcl))
321             Pirls = np.hstack((Pirls, Pirl))
322             Tcls = np.hstack((Tcls, Tcl))
323             hfls = np.hstack((hfls, hfl))
324             T_tcls = np.hstack((T_tcls, T_tcl))
325
326         else:
327
328             ##only layer
329             N = 0
330             local_cond = True
331             local_rad = True
332             local_conv = True
333             local_gen = True
334             local_int_out = False
335             local_int_in = False
336             local_standoff = True
337             local_wires = True
338             Pls, Qrls, Qcls, Prls, Pcls, Pirls, Tcls, hfls, T_tcls =
                    getTempDistr(N, local_cond, local_rad, local_conv, local_gen,
                    local_int_out,
339                                                                 local_int_in
                                                                    ,
                                                                    local_standoff
                                                                    ,
                                                                    local_wires
                                                                    ,
```

```
                                                                    P_0
                                                                    ,
                                                                    Tc_0
                                                                    ,
                                                                    hfromT
                                                                    (
                                                                    Tf_inlet
                                                                    )
                                                                    ,
                                                                    Tcs
                                                                    )
340
341     return Pls, Qrls, Qcls, Prls, Pcls, Pirls, Tcls, hfls, T_tcls
342
343
344 def solver(P_0, Tc_0):
345
346 # description: intermediate solver function only really used for internal-
        radiation iterations
347
348 # intputs:  #P_0:   Power flowing through wall at inlet / baseplate
        interface
349             #Tc_0:  Temperature of wall at inlet / baseplate interface
350
351 # outputs:  #Ps:    distribution of power flowing through wall
352             #Qrs:   distribution of radiated heat flux
353             #Qcs:   distribution of convected heat flux
354             #Prs:   distribution of radiated power
355             #Pcs:   distribution of convected power
356             #Pirs:  distribution of internally radiated power
357             #Tcs:   distribution of casing wall temperature
358             #hfs:   distribution of fluid enthalpy
359             #T_tcs: temperature measured by thermocouple
360
361     global global_int
362
363     if global_int:
364
365         current_rel_fac = rel_fac
366         boggle_factor = 0
367
368         global_int = False
369         Tcs = np.zeros(n * Nl)

                #generating input temperature distribution (not used anyway
                when no inter layer radition, but nevertheless required as an
                input)
370         Ps, Qrs, Qcs, Prs, Pcs, Pirs, Tcs_old, hfs, T_tcs = sub_solver(P_0
                , Tc_0, Tcs)          #initialisation of temperature
                distribution, assuming no inter-layer radiation
371
372         global_int = True
```

```
373         Ps, Qrs, Qcs, Prs, Pcs, Pirs, Tcs, hfs, T_tcs = sub_solver(P_0,
                Tc_0, Tcs_old)          #getting first temp distr with inter-
                layer radiation, using previous temp distr as input
374         Tc_error = np.absolute((Tcs - Tcs_old) / Tcs)
                                                        #computing error
                between new and old temp distr
375
376         lcf = 0
377         counter = 0
378
379         while np.any(Tc_error > conv_crit):# or abs(np.sum(Pirs)) >
                conv_crit:                  #checking error and power balance
                for convergence
380
381             Ps, Qrs, Qcs, Prs, Pcs, Pirs, Tcs, hfs, T_tcs = sub_solver(P_0
                    , Tc_0, Tcs_old)     #getting next temp distr with inter-
                    layer radiation, using updated temp distr as input
382             Tc_error_new = np.absolute((Tcs - Tcs_old) / Tcs)
                                                    #computing error between
                    new and old temp distr
383             if (np.max(Tc_error_new) / np.max(Tc_error)) > 1+conv_crit :
384                 current_rel_fac = current_rel_fac / (np.max(Tc_error_new)
                        / np.max(Tc_error))
385                 lcf = 0
386             elif (np.max(Tc_error_new) / np.max(Tc_error)) < 1+conv_crit:
387                 if lcf >= 50:
388                     current_rel_fac = current_rel_fac * 1.1
389                     lcf = 0
390                 else:
391                     current_rel_fac = current_rel_fac / (np.max(
                            Tc_error_new) / np.max(Tc_error))**0.5
392                     lcf = lcf + 1
393             Tc_error = Tc_error_new
394             Tcs_old = current_rel_fac * Tcs + (1 - current_rel_fac) *
                    Tcs_old
395             counter = counter + 1
396             if counter == 100:
397                 print('Max difference between solutions: ', max(Tc_error),
                        '\t Relaxation factor: ', current_rel_fac)
398                 counter = 0
399
400     else:
401
402         Tcs = np.zeros(n * Nl)

                #generating input temperature distribution (not used anyway
                when no inter layer radition, but nevertheless required as an
                input)
403         Ps, Qrs, Qcs, Prs, Pcs, Pirs, Tcs, hfs, T_tcs = sub_solver(P_0,
                Tc_0, Tcs)           #getting temperature distribution, in
                case of no inter-layer radiation
404
405     return Ps, Qrs, Qcs, Prs, Pcs, Pirs, Tcs, hfs, T_tcs
406
407
408 def get_BC_in(inlet_BC, mini, maxi):
```

```
409
410 # description: iterative and recursive function to get the correct inlet
        boundary conditions at the inlet to fullfill the desired outlet
        conditions
411
412 # intputs: #inlet_BC: 't' or 'p', see variable declaration for
        explanation
413             #lower boundary within which to look for solution
414             #upper boundary within which to look for solution
415
416 # outputs: #BC:    boundary condition at inlet to fulfill power input at
        outlet (can be power or temperature depending on case)
417
418     global n
419
420     BC = (mini + maxi) / 2
                                                          #computing mid-
          point between min and max inputs
421
422     if inlet_BC == 'p':
423         n = n_base
424         Ps, Qrs, Qcs, Prs, Pcs, Pirs, Tcs, hfs, T_tcs = solver(P_0, BC)
                #getting results with mid-point guess as BC for fixed power
              case
425     elif inlet_BC == 't':
426         n = n_base
427         Ps, Qrs, Qcs, Prs, Pcs, Pirs, Tcs, hfs, T_tcs = solver(BC, Tc_0)
                #getting results with mid-point guess as BC for fixed
             temperature case
428
429     print('Inlet BC guess: ', BC, '\t Power at outlet: ', Ps[-1])
430
431     if global_gen:
432         P_ref = 0
433         P_error = abs(Ps[-1])
434     else:
435         P_ref = P_cart
436         P_error = abs((Ps[-1] - P_ref) / P_ref)
                                        #compute error of power at outlet
             for inlet BC guess
437
438     if P_error > conv_crit and abs((maxi - mini) / max(abs(mini), abs(maxi
          ))) > 1e-14:      #checking for convergence toward correct outlet
         BC with condition for exiting iterations in case of non-convergence
439
440         if Ps[-1] < P_ref:
441             BC = get_BC_in(inlet_BC, BC, maxi)
                                                #function calling itself with
                 min value updated with BC guess in case BC guess was too
                 small
442         else:
443             BC = get_BC_in(inlet_BC, mini, BC)
                                                #function calling itself with
                 max value updated with BC guess in case BC guess was too
                 large
444
```

```
445     return BC
446
447
448 def get_results(inletBC, Nl, plot, printRes, label, color):
449
450 # description: function calling the necessary functions to compute, plot
        and print the results
451
452 # intputs:  #inlet_BC:  't' or 'p', see variable declaration for
        explanation
453             #number of layers
454             #turn on/off plotting of results
455             #turn on/off printing of results
456             #label attributed to results
457             #color attributed to results
458
459 # outputs:  #Ps:    distribution of power flowing through wall
460             #Qrs:   distribution of radiated heat flux
461             #Qcs:   distribution of convected heat flux
462             #Prs:   distribution of radiated power
463             #Pcs:   distribution of convected power
464             #Pirs:  distribution of internally radiated power
465             #Tcs:   distribution of casing wall temperature
466             #hfs:   distribution of fluid enthalpy
467             #T_tcs: temperature measured by thermocouple
468
469     global P_0, Tc_0, dxs, As, Dhs, xs, main_path
470
471     time_start_run = datetime.now()
472
473     init_interp_funcs()

            #initializing interpolation functions
474
475     if save_input or save_output or save_figures:
476         main_path = createMainFolder(sim_name, main_folder_name)
                                        #create main folder to which output
              files are saved
477
478     if save_input:
479         saveInput(label)

              #save input parameters
480
481     print()
482
483     As = np.pi*(r_1s**2 - r_2s**2 + r_3s**2 - r_4s**2)
                                                #compute cross sectional area
          of layers
484
485     Dhs = (r_2s - r_3s) * 2
                                                                            #
          compute hydraulic diameter of channels
486
487     dxs = ls / n_base
```

```
        #compute step size for each layer
488     xs = np.linspace(0, ls[len(ls)-Nl], n_base)
489     for i in range(1, Nl):
490         xs = np.hstack((xs, np.linspace(np.sum(ls[len(ls)-Nl:len(ls)-Nl+i
                ]), np.sum(ls[len(ls)-Nl:len(ls)-Nl+i+1]), n_base)))
                #compute x coordinates along wall path
491
492     if inlet_BC == 'p':
493
494         P_0 = P_inlet
495         Tc_0 = get_BC_in(inlet_BC, 273, 1000)
                                                    #get inlet
                conditions for fixed power case
496
497     elif inlet_BC == 't':
498
499         Tc_0 = Tc_inlet
500         P_0 = get_BC_in(inlet_BC, min(-10,-P_cart), P_cart)
                                          #get inlet conditions for fixed
                temperature case
501
502     Ps, Qrs, Qcs, Prs, Pcs, Pirs, Tcs, hfs, T_tcs = solver(P_0, Tc_0)
                            #get results from solver
503
504     time_end_run = datetime.now()
505     elapsed_time = time_end_run - time_start_run
506
507     if np.any(Tcs <= 268):
508         print('\nWarning:□Casing□temperature□too□low,□solution□may□not□be□
                correct!')        #print warning for low casing temperature
509
510     if np.any(Tcs >= 1500):
511         print('\nWarning:□Casing□temperature□too□high,□solution□may□not□be
                □correct!')       #print warning for high casing temperature
512
513     if np.any(TfromEnthalpy(hfs) < 273):
514         print('\nWarning:□Fluid□temperature□too□low,□solution□may□not□be□
                correct!')         #print warning for low fluid temperature
515
516     if global_gen:
517         P_ref = 0
518         P_error = abs(Ps[-1])
519     else:
520         P_ref = P_cart
521         P_error = abs((Ps[-1] - P_ref) / P_ref)
522
523     if P_error > conv_crit:
524         print('\nWarning:□Inlet□boudary□condition□did□not□converge,□
                solution□may□not□be□correct!□Please□use□different□input□values.
                ')       #print warning if the power input BC could not be
                achieved
525
526     if plot:
527         plotResults(label, color, Ps, Qrs, Qcs, Prs, Pcs, Pirs, Tcs, hfs,
                xs, Nl, T_tcs)    #send results to plotting function
528
```

```
529     if printRes:
530         printResults(label, Ps, Qrs, Qcs, Prs, Pcs, Pirs, Tcs, hfs, xs,
                T_tcs, elapsed_time)              #send results to printing
                function
531
532     if save_output:
533         saveOutput(label, Ps, Qrs, Qcs, Prs, Pcs, Pirs, Tcs, hfs, T_tcs,
                elapsed_time)                     #send results to results
                saving function
534
535     return Ps, Qrs, Qcs, Prs, Pcs, Pirs, Tcs, hfs, T_tcs
536
537
538 def init_interp_funcs():
539
540     global hfromT, TfromEnthalpy, rhofromEnthalpy, VfromEnthalpy,
            EfromEnthalpy, sfromEnthalpy, CvfromEnthalpy, CpfromEnthalpy,
            afromEnthalpy, JTfromEnthalpy, mufromEnthalpy, condfromEnthalpy,
            PhasefromEnthalpy, kcfromT_metal
541
542     fluid_properties = importNISTdata(fluid_data)
543     kcOfmetal = importMetalData(metal_data)
544
545     hfromT = interpolate.interp1d(fluid_properties[:,0], fluid_properties
            [:,5], bounds_error=False, fill_value='extrapolate')
546     TfromEnthalpy = interpolate.interp1d(fluid_properties[:,5],
            fluid_properties[:,0], bounds_error=False, fill_value='extrapolate'
            )
547     rhofromEnthalpy = interpolate.interp1d(fluid_properties[:,5],
            fluid_properties[:,2], bounds_error=False, fill_value='extrapolate'
            )
548 ##    VfromEnthalpy = interpolate.interp1d(fluid_properties[:,5],
        fluid_properties[:,3], bounds_error=False, fill_value='extrapolate')
549 ##    EfromEnthalpy = interpolate.interp1d(fluid_properties[:,5],
        fluid_properties[:,4], bounds_error=False, fill_value='extrapolate')
550 ##    sfromEnthalpy = interpolate.interp1d(fluid_properties[:,5],
        fluid_properties[:,6], bounds_error=False, fill_value='extrapolate')
551 ##    CvfromEnthalpy = interpolate.interp1d(fluid_properties[:,5],
        fluid_properties[:,7], bounds_error=False, fill_value='extrapolate')
552     CpfromEnthalpy = interpolate.interp1d(fluid_properties[:,5],
            fluid_properties[:,8], bounds_error=False, fill_value='extrapolate'
            )
553 ##    afromEnthalpy = interpolate.interp1d(fluid_properties[:,5],
        fluid_properties[:,9], bounds_error=False, fill_value='extrapolate')
554 ##    JTfromEnthalpy = interpolate.interp1d(fluid_properties[:,5],
        fluid_properties[:,10], bounds_error=False, fill_value='extrapolate')
555     mufromEnthalpy = interpolate.interp1d(fluid_properties[:,5],
            fluid_properties[:,11], bounds_error=False, fill_value='extrapolate
            ')
556     condfromEnthalpy = interpolate.interp1d(fluid_properties[:,5],
            fluid_properties[:,12], bounds_error=False, fill_value='extrapolate
            ')
557     PhasefromEnthalpy = interpolate.interp1d(fluid_properties[:,5],
            fluid_properties[:,13], bounds_error=False, fill_value=(0, 1))
558
559     kcfromT_metal = interpolate.interp1d(kcOfmetal[:,0], kcOfmetal[:,1],
```

```
        bounds_error=False, fill_value='extrapolate', kind = 'quadratic')
560
561
562 def plotResults(label, color, Ps, Qrs, Qcs, Prs, Pcs, Pirs, Tcs, hfs, xs,
        Nl, T_tcs):
563
564 # description: function plotting the results
565
566 # inputs:   #label: label attributed to results
567             #color: color attributed to results
568             #Ps:    distribution of power flowing through wall
569             #Qrs:   distribution of radiated heat flux
570             #Qcs:   distribution of convected heat flux
571             #Prs:   distribution of radiated power
572             #Pcs:   distribution of convected power
573             #Pirs:  distribution of internally radiated power
574             #Tcs:   distribution of casing wall temperature
575             #hfs:   distribution of fluid enthalpy
576             #Nl:    number of layers
577             #T_tcs: temperature measured by thermocouple
578
579 # outputs:  None
580
581     ax[0,0].plot(xs, Tcs-273.15, label = 'HX temperature '+label, color =
            color, linestyle = linestyles[0])
582     if global_conv:
583         ax[0,0].plot(xs, TfromEnthalpy(hfs)-273.15, label = 'Fluid
                temperature '+label, color = color, linestyle = '-')
584     for i in range(Nl):
585         ax[0,0].plot((np.sum(ls[len(ls)-Nl:len(ls)-Nl+i+1]), np.sum(ls[len
                (ls)-Nl:len(ls)-Nl+i+1])),
586                      (min(min(Tcs-273.15), min(TfromEnthalpy(hfs)-273.15))
                         ,
587                       max(max(Tcs-273.15), max(TfromEnthalpy(hfs)-273.15))
                          ),
588                      color = 'k', linestyle = ':')
589     ax[0,0].plot(np.sum(ls[len(ls)-Nl:len(ls)]) - TC_pos[1], np.sum(T_tcs)
            -273.15,
590                      color = color, marker = 'x', label = 'Thermocouple '+
                         label, linestyle = 'none')
591
592     ax[1,0].plot(xs, PhasefromEnthalpy(hfs), label = label, color = color,
            linestyle = '-')
593     for i in range(Nl):
594         ax[1,0].plot((np.sum(ls[len(ls)-Nl:len(ls)-Nl+i+1]), np.sum(ls[len
                (ls)-Nl:len(ls)-Nl+i+1])),
595                      (0, 1), color = 'k', linestyle = ':')
596
597     ax[0,1].plot(xs, Ps, label = label, color = color, linestyle = '-')
598     for i in range(Nl):
599         ax[0,1].plot((np.sum(ls[len(ls)-Nl:len(ls)-Nl+i+1]), np.sum(ls[len
                (ls)-Nl:len(ls)-Nl+i+1])),
600                      (min(Ps), max(Ps)), color = 'k', linestyle = ':')
601
602 ##    if global_rad:
603 ##        ax[1,1].plot(xs, Qrs, label = 'radiated heat flux '+label, color
```

```
        = color, linestyle = linestyles[0])
604     if global_conv:
605 ##      ax[1,1].plot(xs, Qcs, label = 'convected heat flux '+label,
        color = color, linestyle = linestyles[1])
606         ax[1,1].plot(xs, Qcs, label = label, color = color, linestyle =
                linestyles[1])
607     for i in range(Nl):
608         ax[1,1].plot((np.sum(ls[len(ls)-Nl:len(ls)-Nl+i+1]), np.sum(ls[len
                (ls)-Nl:len(ls)-Nl+i+1])),
609                      (min(Qcs),max(Qcs)), color = 'k', linestyle = ':')
610
611
612 def printResults(label, Ps, Qrs, Qcs, Prs, Pcs, Pirs, Tcs, hfs, xs, T_tcs,
        elapsed_time):
613
614 # description: function printing the results
615
616 # inputs:   #Ps:    distribution of power flowing through wall
617             #Qrs:   distribution of radiated heat flux
618             #Qcs:   distribution of convected heat flux
619             #Prs:   distribution of radiated power
620             #Pcs:   distribution of convected power
621             #Pirs:  distribution of internally radiated power
622             #Tcs:   distribution of casing wall temperature
623             #hfs:   distribution of fluid enthalpy
624             #xs:    x coordinates along wall path
625             #T_tcs: temperature measured by thermocouple
626
627 # outputs:  None
628
629     print()
630     print(label)
631     print('T_fluid @ cartridge = ', TfromEnthalpy(hfs[-1]), '[K]')
632     print('T_thermoCouple = ', np.sum(T_tcs), '[K]')
633     print('T_casing @ inlet = ', Tcs[0], '[K]')
634     print('Power loss to satellite = ', P_cart - np.sum(Pcs) - np.sum(Prs)
        , '[W]')
635     print('Power loss through radiation = ', np.sum(Prs), '[W]')
636     if P_cart != 0:
637         print('Efficiency = ', np.sum(Pcs)/P_cart)
638     print('Elapsed time = ', elapsed_time)
639
640
641 def createMainFolder(sim_name, main_folder_name):
642
643     folder_name = sim_name + '_' + time_start.strftime('%Y-%m-%d_%H-%M-%S'
        )
644     if test:
645         folder_name = 'Test\\' + folder_name
646     path = os.path.dirname(os.path.realpath(__file__)) + '\\' +
        main_folder_name + '\\' + folder_name
647     if not os.path.exists(path):
648         os.makedirs(path)
649
650     return path
651
```

```
652
653 def saveOutput(label, Ps, Qrs, Qcs, Prs, Pcs, Pirs, Tcs, hfs, T_tcs,
        elapsed_time):
654
655 # description: function to save results of simulation run
656
657 # inputs:   #label: label of simulation run
658             #Ps:    distribution of power flowing through wall
659             #Qrs:   distribution of radiated heat flux
660             #Qcs:   distribution of convected heat flux
661             #Prs:   distribution of radiated power
662             #Pcs:   distribution of convected power
663             #Pirs:  distribution of internally radiated power
664             #Tcs:   distribution of casing wall temperature
665             #hfs:   distribution of fluid enthalpy
666             #T_tcs: temperature measured by thermocouple
667
668 # outputs:  None
669
670     path = main_path + '\\' + label
671     if not os.path.exists(path):
672         os.makedirs(path)
673     np.save(path + r'\output', np.array([Ps, Qrs, Qcs, Prs, Pcs, Pirs, Tcs
            , hfs, xs]))
674     np.savetxt(path + r'\output.txt', np.array([Ps, Qrs, Qcs, Prs, Pcs,
            Pirs, Tcs, hfs, xs]))
675
676     version = os.path.basename(__file__)
677
678     if P_cart != 0:
679         efficiency = np.sum(Pcs)/P_cart
680     else:
681         efficiency = 0
682
683     with open(r'Reference Data\Output summary template.txt', 'r') as
            template:
684         summary = template.read().format(version, label, TfromEnthalpy(hfs
                [-1]), np.sum(T_tcs), Tcs[0], P_cart - np.sum(Pcs) - np.sum(Prs
                ), np.sum(Prs), efficiency, elapsed_time)
685
686     with open(path + r'\Output summary.txt', 'w') as output:
687         output.write(summary)
688
689
690 def saveInput(label):
691
692 # description: function to save inputs of simulation run
693
694 # inputs:   None
695
696 # outputs:  None
697
698     path = main_path + '\\' + label
699     if not os.path.exists(path):
700         os.makedirs(path)
701
```

```
702     version = os.path.basename(__file__)
703
704     with open(r'Reference Data\Input summary template.txt', 'r') as
            template:
705         summary = template.read().format(version, save_input, save_output,
                save_figures, test, main_folder_name, sim_name, fluid_data,
706                                          metal_data, Nl, r_1s, r_2s, r_3s,
                                                 r_4s, ls, standoff_dims,
                                             N_standoff, wire_dims,
707                                          N_wires, kc_wires, cart_dims,
                                             TC_pos, n_base, global_cond,
                                             global_rad, global_conv,
708                                          global_gen, global_int,
                                             global_standoff, global_var_kc
                                             , global_var_Nu, global_wires,
                                              conv_crit,
709                                          rel_fac, base_kc, epsilon, sigma,
                                              base_Nu, P_cart, m_dot,
                                             P_inlet, Tc_inlet, Tf_inlet,
                                             Ta, inlet_BC)
710
711     with open(path + r'\input summary.txt', 'w') as output:
712         output.write(summary)
713
714
715 def showplt():
716
717 # description: function to embelish and show the plots
718
719 # inputs:   None
720
721 # outputs:  None
722
723     ax[0,0].set_xlabel('path length from inlet [m]')
724     ax[0,0].set_ylabel(r'temperature $[^{\circ}C]$')
725     ax[0,0].set_title('Casing & fluid temperatures')
726     ax[0,0].legend()
727     ax[0,0].grid(True)
728
729     ax[1,0].set_xlabel('path length from inlet [m]')
730     ax[1,0].set_ylabel('phase [-]')
731     ax[1,0].set_title('Fluid phase')
732     ax[1,0].legend()
733     ax[1,0].grid(True)
734
735     ax[0,1].set_xlabel('path length from inlet [m]')
736     ax[0,1].set_ylabel('power [W]')
737     ax[0,1].set_title('Conducted power')
738     ax[0,1].legend()
739     ax[0,1].grid(True)
740
741     ax[1,1].set_xlabel('path length from inlet [m]')
742     ax[1,1].set_ylabel(r'heat flux $[W/m^2]$')
743     ax[1,1].set_title('Convected heat flux')
744     ax[1,1].legend()
745     ax[1,1].grid(True)
```

```
746
747     plt.tight_layout()
748
749     if save_figures:
750         plt.savefig(main_path + r'\temp_distr')
751     plt.show()
752
753
754 ##############################   Main Program
    ##############################
755
756 #simulation report
757 save_input = True                                   #turn on/off
    generation and saving of file containing input values
758 save_output = True                                  #turn on/off
    generation and saving of file containing output values
759 save_figures = True                                 #turn on/off saving of
     figures
760 test = False                                        #create folder
    containing simulation in separate folder titled "test"
761
762 main_folder_name = 'Reports'                       #folder in which
    subfolders should be created and files saved
763 sim_name = 'Test_comparison'                                #name of
    simulations run used for folder containing files of individual
    simulations
764
765 #slecting reference data from files
766 fluid_data = 'H2O@3.0bar.dat'                       #reference data used
    for fluid properties
767 metal_data = 'inconel718.dat'                       #reference data used
    for casing properties (only conductivity as a function of temperature)
768
769 ##geometry
770
771 NI = 3                                              #number of layers
772
773 r_1s = np.array([0.01339, 0.01109, 0.00779, 0.00449])       #outer walls
    outer radii
774 r_2s = np.array([0.01259, 0.01029, 0.00699, 0.00369])       #outer walls
    inner radii / fluid channel outer radii
775 r_3s = np.array([0.01209, 0.00979, 0.00649, 0.00319])       #inner walls
    outer radii / fluid channel inner radii
776 r_4s = np.array([0.01129, 0.00899, 0.00569, 0])            #inner walls
    inner radii
777
778 ls = np.array([0.0416, 0.0416, 0.0416, 0.0416])           #length of
    each layer
779
780 standoff_dims = np.array([0.01, 0.005, 0.0015])    #length, width and
    height of thermal stand-off conections
781 N_standoff = 3                                     #number of thermal
    stand-off connecitons
782
783 wire_dims = np.array([0.16, 0.0003219])            #length and radius of
    thermal cartridge wires
```

```
784 N_wires = 4                                          #number of wires
785 kc_wires = 19.2                                      #thermal conductivity
       of wires
786
787 cart_dims = np.array([0.00635, 0.03466])             #dimensions of
       cartridge heater sections (length of forward unheated section, length
       of central heated section) [m]
788
789 TC_pos = np.array([0.00135, 0.01])                   #reference point used
       for cartridge heater temperature (radial position = difference betweeen
        radius of heating coil and heater shell, longitudinal distance from
       tip)
790
791 ##mesh
792
793 n_base = 50                                              #number of
       elements per layer (minimum 250, 500 to 1000 recommended)
794
795 ##physical mechanisms
796
797 global_cond = True                                       #turn on/off
       conduction along wall
798 global_rad = True                                        #turn on/off radiation
        to environment
799 global_conv = True                                       #turn on/off
       convection to fluid
800 global_gen = True                                        #turn on/off
       distributed heat generation of cartridge heater
801 global_int = True                                      #turn on/off inter-
       layer radiation
802 global_standoff = False                                  #turn on/off thermal
       stand-off
803 global_var_kc = True                                    #turn on/off
       temperature dependent conductivity
804 global_var_Nu = False                                   #turn on/off variable
       Nusselt number
805 global_wires = False                                    #turn on/off thermal
       conductivity through wires
806
807 ##convergence
808
809 conv_crit = 1e-2                                       #convergence limit
       applied to boudary condition and inter-layer radiation iterations
810 rel_fac = 0.5                                          #relaxation factor to
       prevent inter-layer radiation iterations from oscillating and ensure
       convergence (is now a variable controlled by the simulation, so
       intitial value bares little relevance)
811
812 ##physical properties
813
814 base_kc = 11.338                                           #conductivity of
       wall material (only used if global_var_kc = False)
815 epsilon = 0.8                                          #emissivity of wall
       material
816 sigma = 5.670373e-8                                    #Boltzman constant (
       for radiation)
```

```
817 base_Nu = 3.66                                          #Nusselt number (only
        used if global_var_Nu = False)
818
819 ##boundary conditions
820
821 P_cart = 32                                             #input power of
        cartridge heater
822 m_dot = 8.87e-6#9.63e-6                                        #mass flow
        rate of fluid through HX
823 P_inlet = 0                                             #power flowing trough
        to baseplate/satellite near inlet (only used if inlet_BC = 'p')
824 Tc_inlet = 273.15 + 81                                    #casing temperature
        at baseplate/satellite interface (only used if inlet_BC = 't')
825 Tf_inlet = 273.15 + 35                                    #fluid temperature
        at inlet
826 Ta = 273.15+23                                          #ambient temperature
        of environment
827 inlet_BC = 't'                                          #selection of either
        fixed temperature ('t') or power ('p') at interface with baseplate/
        satellite
828
829 ##solution
830 results0 = get_results(inlet_BC, Nl, True, True, '(test run #8)', colors
        [0])        #get results, plot and print them (results = Ps, Qrs, Qcs,
         Prs, Pcs, Pirs, Tcs, hfs, T_tcs)
831
832 ##############################   Post processing
        ##############################
833
834 #plot results
835
836 showplt()                                               #add legends, grids,
        etc. and show plots
837
838 ##############################   Room for additional stuff
        ##############################
```